Development of Infrared Silicon BIB detectors with integrated linear amplification

DISSERTATION
zur Erlangung des Grades eines Doktors
der Naturwissenschaften

vorgelegt von
Valentin Fedl

eingereicht beim Fachbereich Physik
der Universität Siegen
Siegen, 2011

angefertigt am
Halbleiterlabor der Max-Planck-Institute für Physik und für
extraterrestrische Physik München

Erster Gutachter: Prof. Dr. Lothar Strüder
Zweiter Gutachter: Prof. Dr. Ullrich Pietsch

Tag der mündlichen Prüfung: 13.5.2011

Abstract

Topic of the thesis is the investigation of semiconductor radiation detectors at cryogenic temperatures, which are based on the DEpleted P-channel Field Effect Transistor (DEPFET) active pixel sensor and the Blocked Impurity Band (BIB) detector concept. The DEPFET is a monolithic sensor-amplifier combination, which is able to determine the amount of signal electrons with very low noise. The BIB detector is a mid-infrared sensor, which is sensitive in the 5 μm to 40 μm bandwidth.

The main subject is the investigation of the basic detector's physical mechanisms at cryogenic conditions. It was the purpose of this thesis to develop a physical model for the properties of this active pixel sensor operated at cryogenic temperatures. Special emphasis was given to the amplification mechanisms of the DEPFET and the removal of trapped signal charge from the transistor's gate. A detailed modeling of the electric field inside the transistor's bulk was required to describe the device properties correctly. Based on the understanding of the electron dynamics in the signal collection area with electrons partially trapped in shallow donor states a method for complete signal charge reset was established. It is the basis for proper device operation and was successfully implemented. The predictions of the developed model and the experimental results were very good. The understanding of the device behaviour at cryogenic temperatures and the consistent experimental verification are a sound basis for the final integration of the DEPFET element in a mid-infrared detector system.

Kurzfassung

Gegenstand der Arbeit ist die Untersuchung von Halbleiter Strahlungsdetektoren bei kryogenischen Temperaturen, die auf den DEpleted P-channel Field Effect Transistor (DEPFET) aktiven Pixelsensor und das Blocked Impurity Band (BIB) Detektor Konzept basieren. Der DEPFET ist eine monolithische Sensor-Verstärker Kombination, der die Anzahl von Signalelektronen mit einem geringen Rauschen bestimmen kann. Der BIB Detektor ist ein Sensor im mittleren Infrarot, der im Wellenlängenbereich von 5 μm bis 40 μm sensitiv ist.
Das Hauptthema befasst sich mit der Untersuchung von physikalischen Mechanismen im Detektor bei kryogenischen Temperaturen. Die Zielsetzung dieser Arbeit ist die Entwicklung eines physikalischen Modells, welches die Eigenschaften dieses aktiven Pixelsensors für den Betrieb bei tiefen Temperaturen beschreibt. Der Schwerpunkt lag vor allem bei den Verstärkungsmechanismen im DEPFET und das Entfernen von getrappten Signalladungsträgern aus dem Gate des Transistors. Dabei wurde ein ausführliches Modell der elektrischen Felder im Bulk des Transistors benötigt, um die Eigenschaften des Bauelements genau zu beschreiben. Es wurde eine Methode zum vollständigen Löschen der Signalladung entwickelt, die auf das Verständnis der Elektronendynamik in dem Sammelbereich, indem die Elektronen teilweise in die flachen Störstellen getrappt sind, basiert. Sie bildet die Grundlage für einen einwandfreien Betrieb und wurde erfolgreich implementiert. Die Vorhersagen des entwickelten Modells und der experimentellen Ergebnisse waren sehr gut. Das Verständnis des Bauelementeverhaltens bei kryogenischen Temperaturen und die konsistente experimentelle Verifikation bilden eine gute Grundlage für die finale Integration des DEPFET Elements in ein Mittelinfrarotsensor-System.

Contents

1 Introduction 1

1.1 Motivation . . . 1
1.2 Overview . . . 3
1.3 Infrared detectors . . . 5
1.3.1 Thermal detectors . . . 5
1.3.2 Photodetectors . . . 7
1.4 The conventional extrinsic photodetector . . . 9
1.4.1 Energy band structure and functional principle . . . 9
1.4.2 Drawbacks . . . 10

2 The concept of a BIB detector with integrated linear amplification 11

2.1 Fundamental concept of the BIB structure . . . 11
2.1.1 Energy band structure of heavily doped Silicon . . . 12
2.1.2 The BIB structure . . . 14
2.2 The DEPFET detector concept . . . 17
2.2.1 Functional principle . . . 17
2.3 The combination DEPFET - BIB . . . 20

3 The properties of doped semiconductors at cryogenic temperatures 23

3.1 The hydrogen model of shallow donor states . . . 23
3.2 The Poole-Frenkel effect . . . 25
3.3 The metal-insulator transition . . . 26
3.3.1 Insulating regime . . . 27
3.3.2 Intermediate regime . . . 27
3.3.3 Metallic regime . . . 28
3.4 Mobility . . . 28

4 The investigation of the DEPFET at cryogenic conditions 31

4.1 Setup for the DEPFET . . . 31

4.1.1 Thermal control 32
4.1.2 Readout 33
4.2 Characterisation of the p-MOSFET 38
4.3 Spectroscopic measurements 41
4.3.1 Sample schemes 41
4.3.2 Clear performance 45
4.3.3 Amplification 45

5 The investigation of BIB detector test structures 51
5.1 Material and Design of the BIB structure device 51
5.2 Setup for the BIB structure measurements 52
5.2.1 Thermal control 53
5.2.2 Biasing and readout 53
5.3 Electron transport measurements 54
5.3.1 The blocking mechanism and impurity band conduction 54
5.3.2 Intrinsic electric fields 58
5.3.3 Influence of the p^+-contact 63

6 The reset mechanism of the DEPFET at cryogenic temperatures 65
6.1 The reset problem at cryogenic temperatures 65
6.1.1 Freeze-out of free charge carriers 65
6.1.2 A new method for the reset 68
6.2 Model 70
6.2.1 Electric field enhanced emission 70
6.2.2 Electric field dependent recombination 73
6.2.3 DEPFET Simulation 76
6.2.4 Electron transport in the internal gate 82
6.3 The finite difference method 85
6.3.1 Description 85
6.3.2 Electron dynamics 87
6.4 Experimental results and discussion 96
6.4.1 Dependence on the gate- and clear pulse width 97
6.4.2 Gate pulse 100
6.4.3 Temperature dependence 107
6.5 Review of the experimental and theoretical methods 108
6.6 Future prospects 108
6.6.1 Proposal for a new design 109
6.6.2 Source pulsing 110
6.6.3 Burst mode 112

6.7 Summary of chapter 6 113

7 Conclusion 115

References I

Chapter 1

Introduction

1.1 Motivation

The universe sends us a tremendous amount of information in the form of electromagnetic radiation needed to explore the existence and the behaviour of astrophysical objects. Infrared radiation can pass through interstellar dusts without being absorbed. One example are young stars, being surrounded by a cloud of dust, which is only penetrated by infrared light. Additionally, many objects in the universe which are too cool and faint to be detected in visible light, can be detected in the infrared. For example, the visible light from a planet is hidden by the brightness of the star that it orbits. In the infrared, where planets have their peak brightness, the brightness of the star in the optical regime is reduced, making it possible to detect a planet in the infrared.
The state-of-the-art choice for many astronomical and spectroscopic applications in the mid-infrared wavelength regime, in the 5 to 40 μm bandwidth, are now antimony doped silicon Blocked Impurity Band (BIB) photodetectors. The concept of BIB detectors goes back to the invention of Petroff and Stapelbroek [1]. A readout noise of 10 e^- ENC can be obtained. Existing BIB detectors are operated at temperatures of 5 K to 10 K. The detector and the first amplification stage are connected via bump bonds to the first amplification stage. The disadvantage is the presence of interconnection stray capacitance, existing between the first amplification stage and the detector, which contributes to the readout noise.
The detection of radiation in most semiconductor detectors proceeds in several steps:

1. Arrival of radiation and interaction with the semiconductor
2. Generation and collection of signal charge
3. Amplification and readout of the signal charge (electronics)

4. Removal of the signal charge from the detector

Those four elements are the core components of the detector system. The DEpleted P-channel Field Effect Transistor (DEPFET) is an integrated amplifier-sensor system, which was invented by J. Kemmer and G. Lutz [2]. The sensor can be highly resistive silicon for optical and x-ray applications. With such a device it is possible to achieve an intrinsically low readout noise of 2 e^- ENC. The amplifier structure of the DEPFET is able to further improve the noise performance of the BIB detector. The combination of a BIB detector and a DEPFET represents a new device concept and would be the first mid- to far-infrared sensor with an integrated linear amplifier. For the realization of the DEPFET - BIB system the detector types have to be examined separately.
In this work the physical properties of these devices were investigated at cryogenic temperatures. One important property is the reset of the DEPFET, which was studied in more detail. The infrared sensor combination DEPFET - BIB detector is a promising candidate to detect the previous described astrophysical objects.

1.2 Overview

The aim of this work is the investigation of the device physics of the DEPFET and the BIB structure[1] at cryogenic temperatures. It is the first time, in this work, that the DEPFET was investigated at cryogenic temperatures down to 5 K. Due to low thermal energy, freeze-out effects of charge carriers occur in these devices. The central topic of the thesis is the impact of these effects on the DEPFET transistor, its amplification property and the reset performance. Additionally, dark current measurements on the BIB structure give information about the behaviour of the freeze-out in dependence of electric fields.
Trapping of signal electrons in the DEPFET lead to low clear performance. The time to remove the signal charge exceeds the effective detection time by several orders of magnitude, which makes it unattractive to use it as an integrated amplifier. A new method was developed, based on the principle of enhanced emission of the trapped electrons from the shallow donor states, which is realized by applying dynamic electric fields at their position underneath the gate.
Only by using this method an efficient reset is ensured and the DEPFET can be successfully operated at cryogenic temperatures [3]. Therefore, a model was developed and simulations were performed to understand the physical processes of the signal electrons in the complex potential distribution of the collection region. In combination with the experimental results it is possible to analyze the physical limits of the method.

The thesis is structured in six major parts:

- In this first chapter, a brief introduction of different types of infrared sensors, thermal and photodetectors, is given. The BIB detector is a special type of an extrinsic photodetector. The concept of conventional extrinsic photodetectors is described at the end of the chapter.
- In chapter two, the BIB structure, the DEPFET and the idea to unify these detector concepts are illustrated.
- The third chapter describes the physical properties of doped semiconductors at cryogenic temperatures. The interaction of electrons with shallow donors is modeled in dependence of the electric field and the doping concentration. The understanding of this principle is fundamental to analyze the detectors physics and represents the core of the detector concept.
- Chapter four and five deal with the device physics of the DEPFET and the BIB structure respectively. A measurement setup was established to examine these detector elements separately at cryogenic temperatures down to 5 K. The transistor

[1] In the following chapters the BIB structure means the chip of the whole detector system.

characteristics, the clear performance and the intrinsic amplification of the DEPFET were analyzed. Additionally, BIB structure properties, such as hopping conduction, the blocking mechanism and the intrinsic electric fields are described with analytical models and verified by means of measurements. These mechanisms are based on the interaction of electrons with shallow donor states.

- Chapter six is the main part of this thesis and evaluates the removal of signal charge of the DEPFET at cryogenic temperatures. The physical principle of the interaction of electrons with shallow donor states is discussed in its complex environment. After the description of the problem and the associated components a physical model is presented, which describes the observed properties and shows the way to a proper operation of the reset: The time dependent interaction of the signal electrons with the shallow donors underneath the transistors gate is modeled with a differential equation solved numerically using a finite difference method. The experimental results are discussed and compared with the predictions of the model.
- Finally, in chapter seven, the scientific results of the thesis are summarized.

The new reset method is a breakthrough in the field of cryogenic amplification [4]. The experimental and theoretical methods can be applied on any cryogenic sensor, which is based on the DEPFET principle. This work has enhanced the understanding of the detector system on the basis of a physical model.

1.3 Infrared detectors

For the detection of infrared photons either thermal- or photodetectors are used. In the case of thermal detectors, phonons are generated by incident infrared radiation, while in photodetectors charge carriers such as electrons and/or holes are excited. The properties of the signal carriers such as velocity and energy influence the key parameters such as spectral response, speed and energy resolution. In the following subsections the two detector types are briefly introduced. Furthermore, the functional principle of the extrinsic photodetector, which builds the fundament for the BIB structure, is explained.

1.3.1 Thermal detectors

Thermal detectors operate on a simple principle: when heated by incoming IR radiation, their temperature increases. The temperature changes are measured by any temperature-dependent mechanism, such as thermoelectric voltage, resistance or pyroelectric voltage. One outstanding device is the superconducting tunneling junction exploiting the generated phonons, which break the bounded states of the cooper pairs leading to the tunneling of the electrons through the insulator.
The simplest representation of the thermal detector is shown in figure 1.1. The detector is represented by a thermal capacitance C_{th} coupled via a thermal conductance G_{th} to a heat sink at a constant temperature T. In the absence of incident radiation, the average temperature of the detector will also be T, although it will exhibit a fluctuation around this value. When the incoming radiation is received by the detector, the rise in temperature is found by solving the heat balance equation [5]:

$$C_{th}\frac{\partial \Delta T}{\partial t} + G_{th}\Delta T = \epsilon\phi \tag{1.1}$$

with ΔT being the temperature difference due to the optical signal ϕ between the detector and its surroundings and ϵ the emissivity of the detector. Assuming the radiant power to be a periodic function $\phi = \phi_0 e^{i\omega t}$, where ω is the frequency and ϕ_0 is the amplitude of sinusoidal radiation, the solution of the differential heat radiation is approximately:

$$\Delta T = \frac{\epsilon\phi_0}{\sqrt{G_{th}^2 + \omega^2 C_{th}^2}} \tag{1.2}$$

It is desirable to make ΔT as large as possible. Therefore, C_{th} and G_{th} must be as small as possible. This means that a small detector and fine connecting wires to the heat sink are

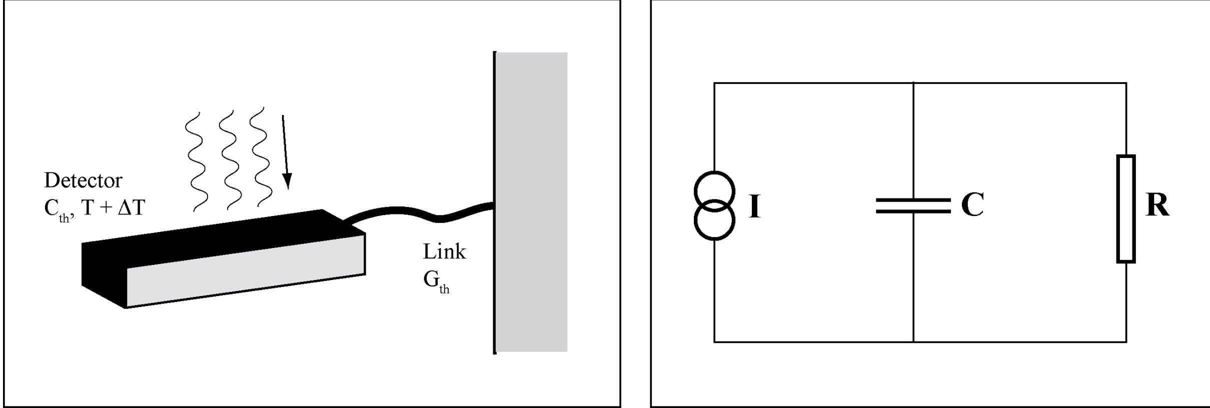

Figure 1.1: *Left:* Thermal detector. *Right:* Its electric analogue.

needed. The thermal resistance is defined as $R_{th} = \frac{1}{G_{th}}$ and equation 1.2 can be rewritten as:

$$\Delta T = \frac{\epsilon \phi_0 R_{th}}{\sqrt{1 + \omega^2 \tau_{th}^2}} \tag{1.3}$$

with τ_{th} being the characteristic thermal response time for the detector which is defined as:

$$\tau_{th} = \frac{C_{th}}{G_{th}} \tag{1.4}$$

The disadvantage of this detector type is the slow response time. Typical values for thermal time constants are in the millisecond range. This is much longer than the typical time of a photon detector. A conventional radiation detector has a response time in the range of a few 100 ns including the generation of charge carriers by incident radiation and their drift/diffusion to the readout node. Additionally, there is a trade-off between the sensitivity, which is proportional to ΔT and the frequency response. A high sensitivity is associated with a low frequency response.
One famous representative for astrophysics applications is the superconducting transition-edge sensor (TES) [6]. It consists of an absorber for the detecting radiation with a thermometer system of small thermal capacity. Since TES thermometers use the extremely rapid change in electrical resistance in the narrow temperature range (<1 mK) of a superconducting transition, the detector must be cooled to 0.05 K and electrically biased into the superconducting transition at about 0.1 μK. Therefore, a small amount of energy

deposits results in a significant measurable change in the resistance leading to a high sensitivity. TES thermometers have achieved an energy resolution of (7.2 ± 0.4) eV full width at half maximum (FWHM) for 6 keV x-rays with a response time of approximately 200 μs [7].

1.3.2 Photodetectors

In contrast to thermal detectors, photodetectors exhibit both excellent signal-to-noise performance and a very fast response. In this class of detectors the radiation is absorbed within the material by interaction with electrons, either bound to lattice atoms, or to impurity atoms or by free electrons. Depending on the nature of the interaction, the class of photon detectors is further sub-divided into different types. The most important are:

1. **Intrinsic photodetectors**,
2. **Quantum well photodetectors** and
3. **Conventional extrinsic photodetectors**

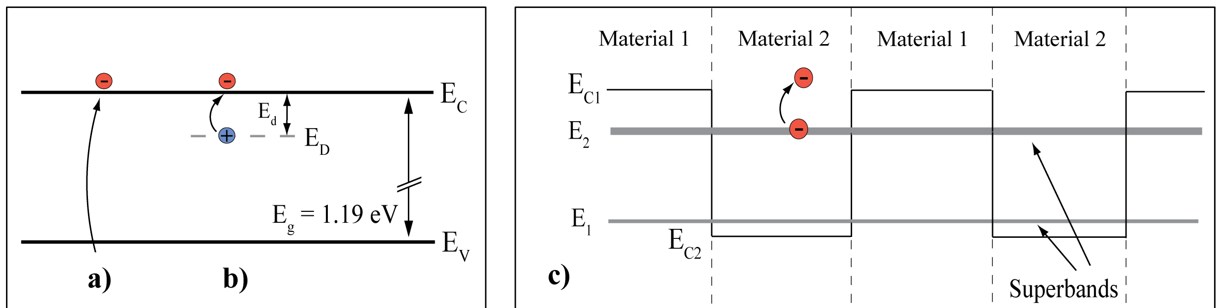

Figure 1.2: Energy band structure and the excitation mechanisms in different semiconductor materials. a) In the intrinsic photodetector the electrons are excited from the valence band. b) The electrons in the extrinsic photodetector are excited from the shallow donors into the conduction band. c) Quantum well detector: Materials with different energy values of the conduction band edges (E_{C1} and E_{C2}) are epitaxially grown in alternate order. This results in bound states E_1 and E_2, which are created in the potential well. The electrons are excited from the superband into the conduction band.

Intrinsic photodetectors

Intrinsic photodetectors are crystal lattices that provide a well-defined spacing between the valence band, within which electrons are captive, and the conduction band, where electrons are free to move through the crystal lattice. If a photon with energy greater than the bandgap is absorbed, an electron will be excited from the valence band and placed into the conduction band as shown in figure 1.2 a). The most important representative for intrinsic detectors for infrared applications is the semiconductor material HgCdTe. Research by Lawson and co-workers triggered development of variable bandgap $Hg_{1-x}Cd_xTe$ alloys, providing an unprecedented degree of freedom on infrared detector design [8]. HgCdTe is special since its bandgap depends on the mixture of mercury and cadmium (fraction x) and the bandgap can be tuned by more than an order of magnitude, from less than 0.1 eV to greater than 1.5 eV. Nevertheless, the cutoff wavelength can be tuned only up to 15 μm [9].

Quantum well detectors

Since the initial proposal by Esaki and Tsu and the advent of the Molecular Beam Epitaxy (MBE), the interest in semiconductor superlattices (SLs) and quantum well structures has increased continously over the years, driven by technological challenges, new physical concepts and phenomena as well as promising applications. It is possible to grow thin epitaxial layers with a thickness in the range of several lattice constants being mostly 4 nm to 10 nm. When materials are grown in alternate order with different energy values of the conduction band edges, potential wells with discrete energies are created. Figure 1.2 c) shows the band structure of a layer system with the discrete energies E_1 and E_2. The bound states overlap and a superband is formed. The photocurrent originates from the excitation of electrons from the superband by incident infrared radiation into higher states. Among the different types of quantum well infrared photodetectors, technology of the GaAs/AlGaAs multiple quantum well detectors is the best known. An important concept associated with device applications of new epitaxial growth techniques is that device structure dimensions in the growth direction can be tuned to achieve a certain cutoff wavelength. This means that one can do electrical engineering at the quantum mechanical level. Cutoff wavelengths of up to 28 μm can be achieved [10].

Extrinsic photodetectors

Extrinsic photodetectors are used for detection in the far infrared at wavelengths beyond 20 μm. The understanding of this detector type is fundamental for the explanation of the BIB structure. Therefore, following section gives a more detailed overview of the conventional extrinsic photodetector.

1.4 The conventional extrinsic photodetector

Extrinsic photodetectors are used in a wide range of the IR-spectrum extending from a few μm to approximately 300 μm. They are the most abundantly used detectors operating in the range of $\lambda > 20$ μm. The spectral range of a extrinsic photodetector is determined by the doping impurities and by the base material into which it is introduced. The active region of an extrinsic photodetector consists of a IV- or III/V-semiconductor with n-type or p-type impurities. Detectors based on silicon and germanium have found the widest application compared to extrinsic photodetectors based on other materials.

1.4.1 Energy band structure and functional principle

The wavefunction of the shallow donors (or acceptors) can be modeled in analogy to the hydrogen atom (subsection 3.1). The electrons, being due to the excess electron from the fifth main group, orbit the positive phosphorous ion with an effective mass of the conduction electron m^* and the dielectric permittivity in silicon ϵ_{Si} [11]:

$$E_b = \frac{m^* q^4}{32\pi^2 \hbar \epsilon_{Si}^2} = \frac{m^*}{\epsilon_{Si}^2} E_{Ryd} \tag{1.5}$$

where E_b is the binding energy, q is the charge, $\hbar$ is the Planck constant and $E_{Ryd} = 13.6$ eV is the Rydberg energy. In silicon, the shallow donor states have a binding energy of about 42.7 meV to 53.7 meV, when the donors act as substitutionals (table 1.1). Otherwise, when the donor atoms do not replace a silicon atom in the lattice, but are incorporated in between the silicon structure, deep impurities are formed. The energy of such a state is approximately in the middle of the energy band gap. The valence electron is bound more strongly and is localized to the impurity atom. The maximum detectable wavelength λ_c can be approximated by the binding energy of the donor:

$$E_b = \frac{\hbar c}{\lambda_c} \tag{1.6}$$

and is in the range of 28 μm to 35 μm for Si:As and Si:Sb. The photons must have an energy greater than the binding energy to excite the electron from the shallow donor states into the conduction band as shown in figure 1.2 b). Every donor provides an electron, which can be used as signal charge for incident photons. In the presence of a voltage the amount of generated electrons can be determined by the measured photocurrent I_{ph}:

$$I_{ph} = q\phi\nu A = q\phi(1 - exp(-d\sigma N_D)) \cdot A \tag{1.7}$$

ϕ is the incoming IR flux, ν is the quantum efficiency, d is the thickness of the sensitive area, σ is the capture coefficient, A is the surface and N_D is the concentration of neutral donors. By applying a voltage at the device contacts the electrons drift in the electric field to the first readout node.

Donor type	Binding energy	Cutoff wavelength
P	45 meV	27.5 μm
As	54.7 meV	22.6 μm
Sb	42.7 meV	29.0 μm

Table 1.1: The binding energy E_b and the cutoff-wavelength λ_c of the shallow donor states of phosphorous, arsen and antimony in silicon. λ_c is calculated by using equation 1.6.

1.4.2 Drawbacks

The fixed ionized donors cannot provide any electrons for further generation by incoming infrared photons. This has the following drawbacks:

1. After a certain exposure time the donors are completely ionized and the detector reaches a state of saturation. This limits the expected operational time of the sensor.
2. The quantum efficiency is reduced as the effective concentration $< N^0_{D,eff} >$ is reduced by the ionized donors $< N^+_D >$:

   $$< N^0_{D,eff} >= N_D - < N^+_D >$$

   In equation 1.7 N_D is replaced by $< N^0_{D,eff} >$. For silicon, N_D is in the range of $10^{16}\frac{1}{\mathrm{cm}^3}$. $< N^0_{D,eff} >$ is a dynamic parameter and depends strongly on the incident photon flux.
3. The ionized donors are trapping centers with a huge capture cross section. When the signal electron is trapped, it does not reach the readout node of the sensor system and therefore, it does not contribute to signal detection. Either, the trapped electron is used for other incident infrared photons. Or, when this electron is emitted thermally at a random time point, it makes a wrong contribution to signal detection. This is an additional noise source of the detector and is called generation-recombination noise.

These drawbacks do not exist for BIB structures as explained in the following chapter.

Chapter 2

The concept of a BIB detector with integrated linear amplification

In this chapter the idea of the infrared sensor combination DEPFET - BIB detector is presented. First, the functional principle of the BIB structure is described. In this connection the energy band structure is relevant for the understanding. Subsequently, the DEPFET is explained. The amplifier structure at the frontside of the DEPFET is relevant for the DEPFET - BIB, which is illustrated at the end of the chapter.

2.1 Fundamental concept of the BIB structure

For the observation of faint astronomical objects in the mid- to far infrared a photodetector with high sensitivity is needed. The BIB detector can fulfill the requirements of high quantum efficiency and low noise.
The active layer of the BIB structure is heavily doped. For example, silicon BIB structures have a doping concentration of $N_D = 10^{17} - 10^{18} \frac{1}{\mathrm{cm}^3}$. The probability to excite an electron increases with the densities of shallow donors. This property comes along with the reduction of the sensitive thickness. State-of-the art BIB structures have an active layer thickness of 35 μm and 45 μm [12]. In comparison, the thickness of conventional extrinsic photodetectors is in the milimeter range.
The energy band structure of the heavily doped active layer is illustrated in subsection 2.1.1. It is fundamental for the understanding of the electron transport in a BIB structure, which is explained in subsection 2.1.2.

2.1.1 Energy band structure of heavily doped Silicon

In a high doping concentration regime, the states of the shallow donors interact with each other, which leads to a change of the energy band structure of silicon. As shown in figure 2.1 an energy band is formed underneath the lower conduction band edge. Neighbouring donor states with the same energy and the same quantum number split due to Pauli's principle. Detailed descriptions of impurity band forming can be found in many publications [13], [14]. The minimum concentration N_{min} for building such an energy band can be estimated with the radius of the 1s-state of the shallow donor r_{1s}. Assuming the 1s-states of the shallow donors fill the whole solid, then, N_{min} is determined to:

$$N_{min} = \frac{1}{V_{1s}} = \frac{1}{4/3\pi r_{1s}^3} \tag{2.1}$$

where V_{1s} is the volume of one 1s-state. The radius r_{1s} can be determined by using the equation for the Bohr radius with an effective mass $m^* = 0.26 \cdot m_0$ [11]:

$$r_{1s} = \frac{4\pi\epsilon_{Si}\hbar^2}{m^* e^2} = 2.4 \text{ nm} \tag{2.2}$$

with $m_0 = 9.1 \cdot 10^{-31}$ kg being the rest mass of an electron and $\epsilon_{Si} = 11.7$ the permittivity of silicon one obtains $N_{min} \approx 10^{18}\ \frac{1}{\text{cm}^3}$.

This has fundamental implications:

1. In addition to the basic n-doping of the active layer the base material incorporates impurities and/or acceptors. The energy levels of these states are within the band gap. Some of the electrons of the shallow donors are caught in these ionized impurities/acceptors. At cryogenic temperatures the low thermal energy does not allow to emit these trapped electrons into higher states, e.g. states in the impurity or conduction band.

2. There is an electron transport in the impurity band. The electrons in the shallow donor states can hop from the shallow donor state to a neighbouring one[1]. Conduction in the impurity band can only occur if there are empty states in which the electrons can hop into. The ionized donors originate from the ionization process of the acceptors as described in item 1. Therefore, the donors can be neutralized by the hopping conduction mechanism and not only by trapped electrons from the

[1] The electrons are provided by an ohmic contact, which is a n^+-implantation.

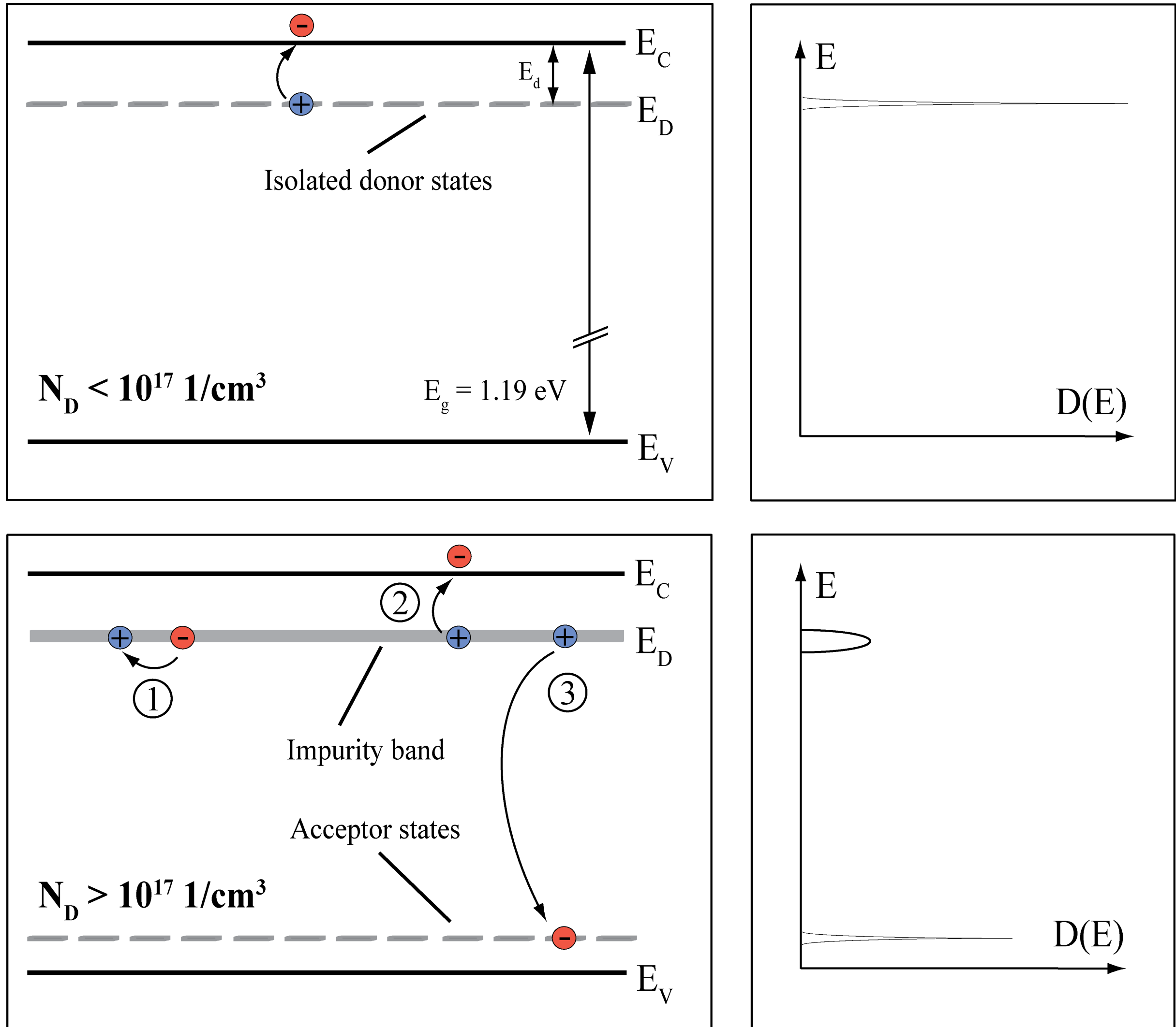

Figure 2.1: *Top Left:* Energy band structure for n-doped silicon at cryogenic temperatures. The doping concentration is lower than $N_D = 10^{17}\ \frac{1}{\text{cm}^3}$ and all donors have one energy level. The ionization occurs via thermal or photon excitation. *Bottom Left:* At concentrations greater than $N_D = 10^{17}\ \frac{1}{\text{cm}^3}$ an impurity band is formed beneath the lower conduction band edge. 1. Electrons can move in the impurity band according to an electric potential (hopping conduction). Donor ionization occurs when 2. an electron is excited into the conduction band or 3. an electron recombines into a lower levelled acceptor state. *Right:* Density of states of the donors for the respective donor concentrations.

conduction band. The electric current comprises of the electron transport in the conduction band and the impurity band:

$$\sigma = \sigma_{imp} + \sigma_c \tag{2.3}$$

σ_{imp} and σ_c are the conductivities of the impurity band and conduction band respectively. For cryogenic temperatures $\sigma_c = 0$ and the electron transport is dominated by conduction of the impurity band only.

2.1.2 The BIB structure

The hopping conduction is stopped by introducing a blocking layer, consisting of highly resistive silicon, on top of the heavily doped active layer. Figure 2.2 shows the band structure of such a BIB structure device. Only electrons in the conduction band can pass the blocking layer and can drift to the first readout node. This mechanism is called Blocked Impurity Band principle. Without the blocking mechanism the hopping conduction leads to a leakage current, which is an additional noise source. The blocking layer is grown epitaxially at the front side of the active layer. The ohmic contacts at the front side and the back side are n^+ shallow implants. In the following, it is referred to figure 2.2 and the BIB structure is described in terms of the space charge, the electric fields and the potential distribution.
The electrons in the acceptor states cannot be emitted back to the donor state because of the low thermal energy in comparison to the band gap energy. The acceptors in the active layer cause the donors to ionize and the amount of ionized donors equals the amount of ionized acceptors:

$$N_A^- = N_D^+ \tag{2.4}$$

The shallow donors cover the whole solid and every acceptor recombines with an electron provided by a donor. Therefore, it can be written:

$$e \cdot N_A^- = e \cdot N_A \tag{2.5}$$

In thermal equilibrium, when no voltage is applied, the density of ionized donors equals the density of acceptors and the whole device is neutral:

$$e \cdot N_A^- + e \cdot N_D^+ = 0 \tag{2.6}$$

When a positive voltage is applied at the n^+-contact of the blocking layer, the electrons in the impurity band of the active layer are attracted towards the blocking layer. At low temperatures of about 5 K to 10 K, the blocking layer functions as an insulator.
Because all acceptors are ionized the space charge ρ is given by:

$$\rho = e \cdot N_A^- = e \cdot N_A$$

The extension of the depleted width w can be calculated from the Poisson equation [15]:

$$w = \sqrt{2\epsilon\epsilon_0 \cdot \frac{V_B - V_{bi}}{qN_A} + b^2} - b \tag{2.7}$$

V_B is the applied bias voltage, V_{bi} is the built in bias and b is the width of the blocking layer. The electric field in the active layer can be written as:

$$E(x) = \frac{qN_a}{\epsilon\epsilon_0}(w - x) \tag{2.8}$$

The electric field in the blocking layer E_{max} is constant as it functions as an insulator. Because the electrons are frozen out and can only exist in the impurity band, the electrons hop towards the blocking layer. They occupy the free vacant sites of the donor states. The donors can only be filled by electrons from the hopping mechanism. In the space charge region the donors are neutral:

$$N_D^+ = 0 \tag{2.9}$$

Thus, the occupation of the free donors results in a negative space charge, which corresponds to the ionized acceptors (equation 2.5). When the detector is exposed to light, free electrons generated by photons that have been absorbed within the depletion region will be collected at the positively biased contact. Electrons excited in the neutral region will recombine with a nearby ionized donor. The ionized donor charge state travels to the negative contact. The combined motion of the positive donor states and the electron results in a photoconductive gain of one. If the detector bias is high enough such that electron impact ionization becomes likely, the photoconductive gain will be greater than unity.

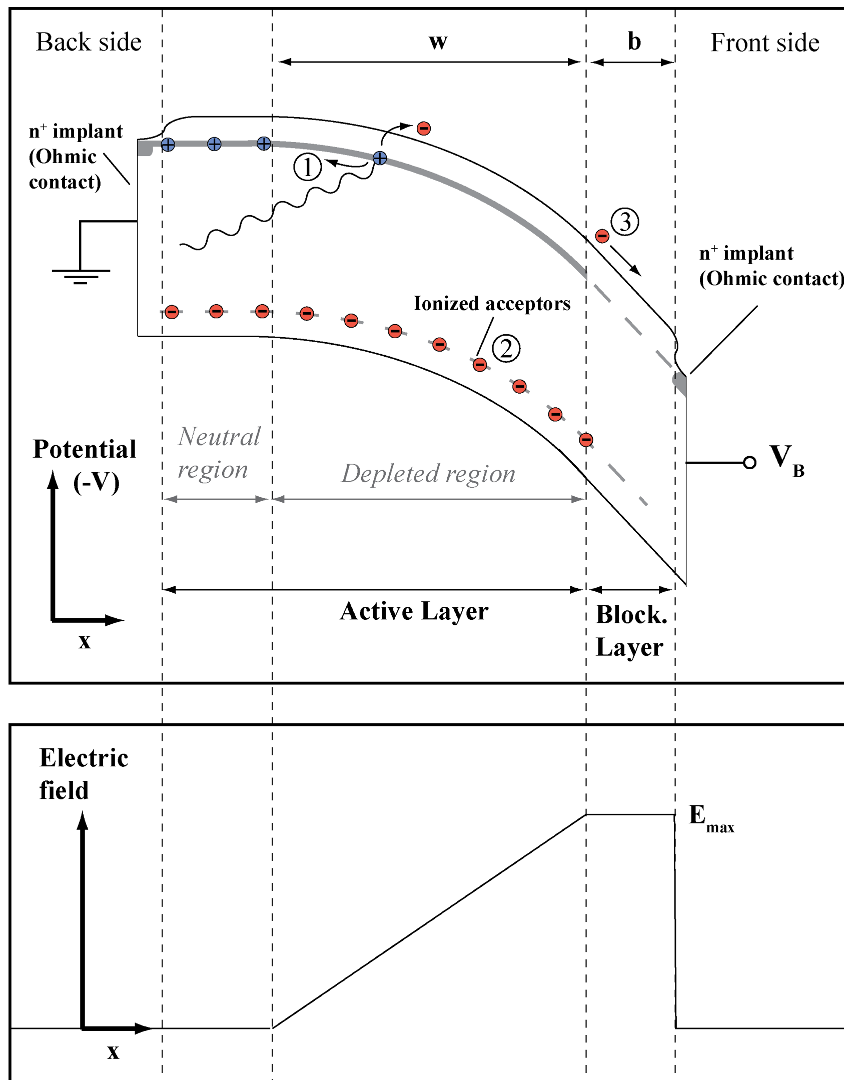

Figure 2.2: Energy band structure of a BIB structure device, when a bias voltage is applied. The following processes are shown: 1. Hopping conduction in the active layer. 2. Ionized acceptors. 3. Electron transport in the conduction band via the blocking layer. Below the electric field distribution is plotted. The blocking layer functions as an insulator, which results in a constant electric field.

2.2 The DEPFET detector concept

The sensors which are developed in the MPI (Max Planck Institute) semiconductor laboratory so far are devices based on reverse biased pn-junctions and metal-oxide-semiconductor (MOS) structures. The materials are high-resistivity silicon with a basic doping concentration of about $1 \cdot 10^{12}\ \frac{1}{\text{cm}^3}$ to achieve sensitive widths up to 500 μm. In the optical regime, from 300 nm to 1000 nm, these detectors can reach a quantum efficiency of close to 100 % [16]. In the x-ray regime they perform well from 100 eV up to 30 keV as spectroscopic imaging detectors. Furthermore, they can be used for particle tracking in elementary particle physics.
The idea of the DEPFET goes back to the invention of J. Kemmer and G. Lutz and it combines the sensor and the first amplification stage to a monolithic device [2]. This concept allows to collect the primary signal charges to the readout node of one pixel, where they can be instantly readout. Metallic wires or bonds do not exist between the sensor and the first amplifier, which reduces the interconnection stray capacitances to a minimum. Additionally, the signal charges can be stored and readout on demand. DEPFET devices were developed, where the collected signal charges were measured several times to reduce the statistical error. It was possible to minimize the readout noise in the sub-electron regime [17].

2.2.1 Functional principle

The DEPFET concept is based on the sidewards depletion principle, which was proposed by E. Gatti and P. Rehak [18]. Figure 2.3 shows a three dimensional schematic of a DEPFET with the p-channel Metal Oxide Semiconductor Field Effect Transistor (MOSFET) being the amplifier [2]. In the following, the functional principle of the DEPFET based on a p-channel MOSFET is described.
A p-channel MOSFET and a close-by n-type clear contact are placed on a fully depleted n-type silicon substrate. The large diode at the back side of the wafer, the n^+- and the p^+-contacts of the FET deplete the substrate.
Figure 2.4 shows the potential of high resistive n-bulk with p^+-implants at the front- and back side. When the back side voltage equals the depletion voltage a potential minimum for electrons forms underneath the channel of the transistor (Cut a in figure 2.3). This deep-n implantation layer underneath the transistor region, which is the internal gate in the actual device, further confines the potential minimum. The internal gate is the global potential minimum for electrons for one pixel as indicated in the potential distribution along cut b 2.3 across the wafer in the gate region. The electrons created by ionizing radiation in the sensitive bulk region are collected into this internal gate and increase the

[2] N-channel MOSFETs or Junction Field Effect Transistors (JFETs) are also possible.

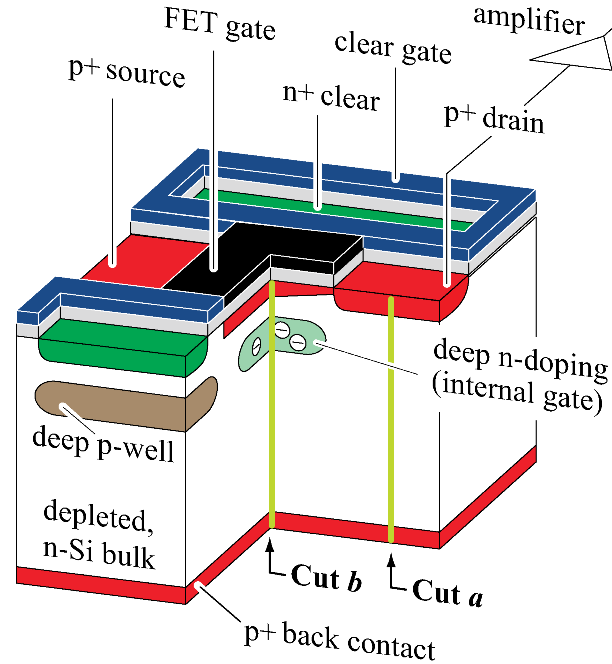

Figure 2.3: Three dimensional schematic of a linearly structured DEPFET.

channel conductivity by inducing holes in the channel. The holes, which are created by the ionization, drift to the back contact.
In order to obtain the optimum noise performance and prevent baseline shift as well as internal gate overflow, the electrons collected in the internal gate must be completely removed by a clear pulse after an integration cycle. The n-type clear contact is pulsed by a sufficiently positive voltage providing a punch-through into the internal gate. In this way the collected signal electrons are removed after the collection time. The clear contact is separated from the detector bulk by a deep p-implanted well. To ensure a complete clear, the clear contact is surrounded by an additional MOS clear gate as shown in figure 2.3. During signal integration and readout, the clear gate is set to a negative voltage to define a potential well that restricts electrons to the internal gate and prevents the injection of electrons from the clear contact to the internal gate. During the reset both clear contact and clear gate are set to positive voltages.
The advantages of the DEPFET are:

1. The amplification of the signal charge at the position of its generation avoids any charge transfer.

2. In contrast to hybrid pixel sensors, the generated electrons do not pass external metallic contacts such as Indium bump bonds or aluminum wires. These are sources

for stray capacitances, which are reduced to a minimum in a DEPFET. The input capacitance is about 20 fF, so that low-noise measurements of signal electrons are possible.

3. The internal gate can be fully depleted, in this case no free carrier charges exist. The signal output of the empty internal gate is the reference for the correlated double sampling (CDS) readout. Thus, no reset noise does exist. The readout method is described in subsection 4.1.2.

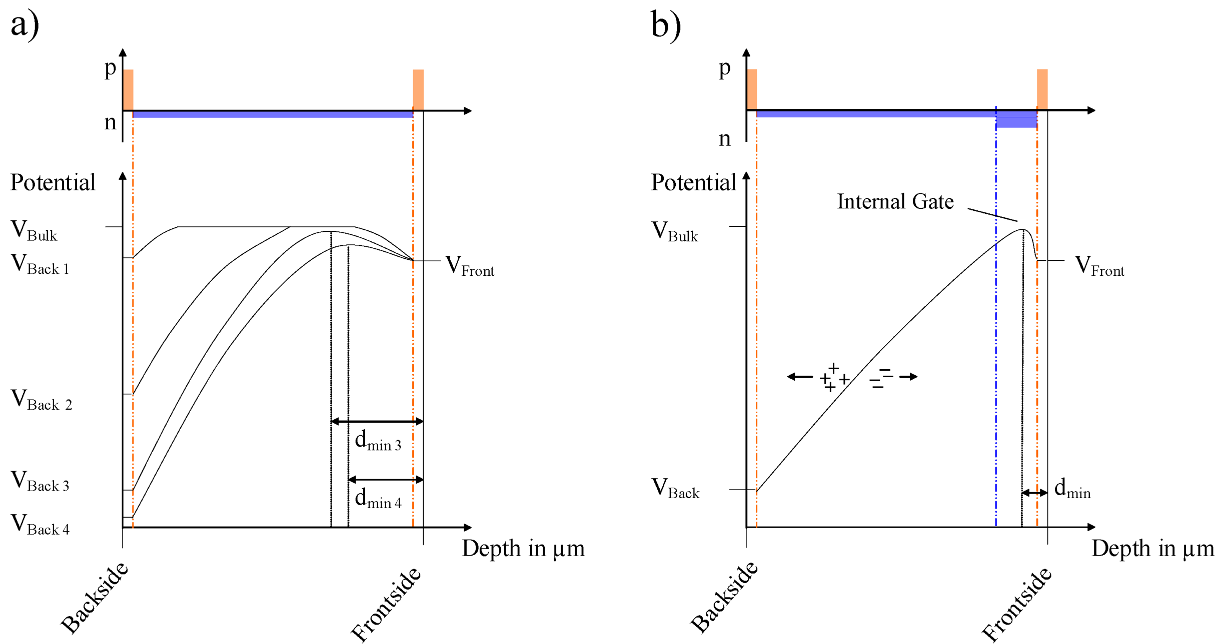

Figure 2.4: Basic principle of sideward depletion. a) The potential is plotted along cut *a* in figure 2.3. The n-doping of the bulk is blue, while the p-doping is labeled with orange. When the back side voltage is lower than V_{back3} the device is fully depleted and a potential minimum for electrons is formed beneath the front side. b) By increasing the n-doping beneath the front side, the minimum is shifted towards the front side. The potential is plotted along cut *b* in figure 2.3. This picture is taken from the phd-thesis by Stefan Wölfel [17].

2.3 The combination DEPFET - BIB

The BIB detector ranks among the most advanced infrared sensors in terms of noise. This makes it an ideal detector for detection of signals from faint astrophysical objects in the infrared regime. Furthermore, future projects foresee a suppression of the background radiation from instruments by cooling down the mirror to liquid helium temperature. SPICA is the first satellite project, which realizes this technical approach. In this case, the dominating noise source is the readout of the front end electronics. Existing BIBs are connected via bump bonds to the first amplification stage and a readout noise of 10 e^{-} ENC can be obtained [19], [20]. The disadvantage of the first amplification stage is the presence of interconnection stray capacitance, which contributes to the readout noise. The aim is to develop a BIB detector which suppresses the readout noise to a minimum of about 2 e^{-} ENC. This shall be achieved by processing the DEPFET on top of the BIB structure.
Figure 2.5 shows a three-dimensional schematic of the infrared sensor combination DEPFET - BIB. The amplifier structure of the DEPFET is integrated on top of the blocking layer of the BIB structure. The working principle is similar to the DEPFET, which is explained in the previous section.

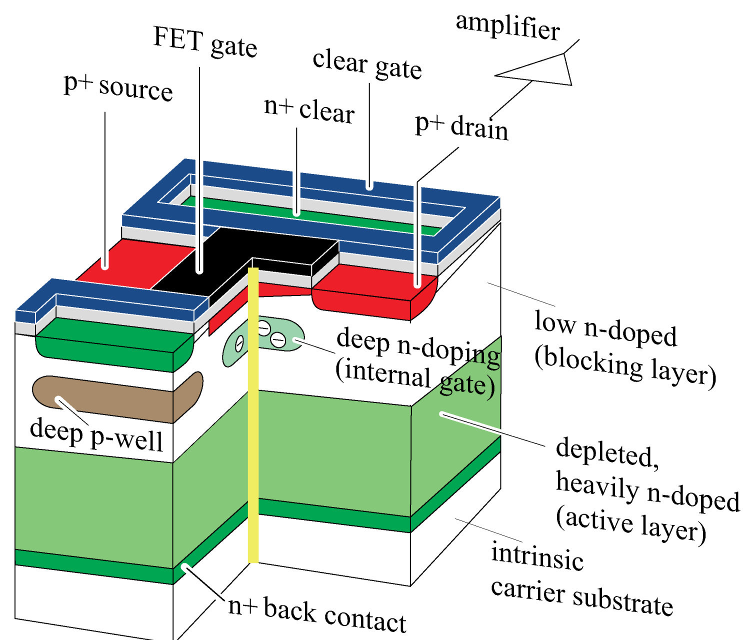

Figure 2.5: Three-dimensional schematic of a pixel of the DEPFET - BIB structure.

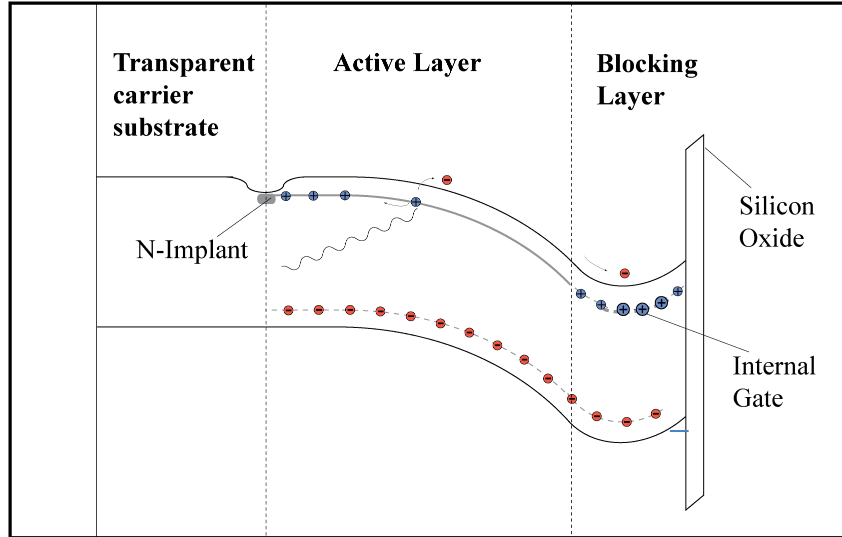

Figure 2.6: b) Potential curve, which is indicated with the yellow line at the schematic in figure 2.5. The signal charge is generated in the active layer and is collected in the internal gate. The internal gate is located in the blocking layer.

In figure 2.6 the one-dimensional potential distribution along the yellow line in figure 2.5 is illustrated. It represents a schematic drawing and combines the potential distributions of the BIB structure and the DEPFET. The electrons are generated in the heavily doped active layer and are collected in the internal gate, which is located in the blocking layer. On the one hand, the blocking layer inhibits the electrons in the impurity band to generate leakage current as described in section 2.1. On the other hand, with the deep n-implantation, it functions as the collection regime for incoming signal electrons.

For the realization of the DEPFET - BIB detector, a basic understanding of the individual detector types has to be established. Therefore, first of all, the approach is to perform measurements, which prove the functional operation. The operating temperature of the BIB detector is 5 K to 10 K, which means that the DEPFET has to work under this condition. Due to low thermal energy, it is expected, that the devices suffer from impact ionization and freeze-out effects. Successful input and output characteristics of the DEPFET show that these effects do not occur in the transistor channel. The BIB structure can be operated in the dark as the hopping conduction and the blocking mechanism were identified.
The next step is to identify the problems, which make successful operation impossible. It was found out that the freeze-out of signal electrons in the internal gate leads to incomplete clear. It was not possible to remove all signal electrons by one clear pulse.
The idea was developed to prevent freeze-out during the clear process. By applying elec-

tric fields at the position of the signal electrons, the binding energy of the shallow donors is reduced. In this way the electrons are emitted from the trapped state into the conduction band. However, the emitted electrons can be captured by the shallow donors before they reach the clear contacts. In order to understand the physical processes of electric field dependent emission and recombination during the reset, the complex potential distribution of the internal gate has to be taken into account. Simulations of the potential and the electric field distribution of the internal gate were performed. Additionally, a simulation program was developed, which calculates the electron concentration in the internal gate during the clear process. For this purpose the physical processes of electric field dependent emission and recombination were implemented. The results from the simulations were compared with the experimental results.
The reset problem of the DEPFET at cryogenic temperatures represents the main part of the thesis and was worked out from the initial idea to the creation of a physical model.

Chapter 3

The properties of doped semiconductors at cryogenic temperatures

The intention of this chapter is to give a fundamental understanding of the physics of shallow donor states in semiconductors at cryogenic conditions. The potential distribution of shallow donors and the electrical behaviour of extrinsic semiconductors at different doping concentrations are discussed. Here, the discussion is restricted to n-doped silicon.

3.1 The hydrogen model of shallow donor states

Semiconductors are materials, which have a resistivity between metals and insulators. The transition between insulators and semiconductors are gradual and they have a resistivity between 10^{-2} Ωcm and 10^{9} Ωcm at room temperature. They have the specific property, that the electrical conductivity can be tuned by adding minor amounts of impurities. For example the addition of group V donor impurities such as phosphorous, arsenic or antimony into silicon can decrease the resistivity because they have an extra valence electron compared to the silicon they replace substitutionally. Figure 3.1 shows the effect, when a phosphorous atom is built into the silicon lattice. The addition of acceptor impurities such as boron have one fewer valence electron compared to silicon and contribute a positive hole as a charge carrier, which can also decrease the resistivity. The theoretical treatments of both of these types of impurities are fundamentally similar. A phosphorous atom which occupies a substitutional site on the silicon lattice acts as an electron donor because it has five valence electrons in its outermost orbital compared to only four for silicon. It also has an extra proton compared to the silicon atom which it replaces.

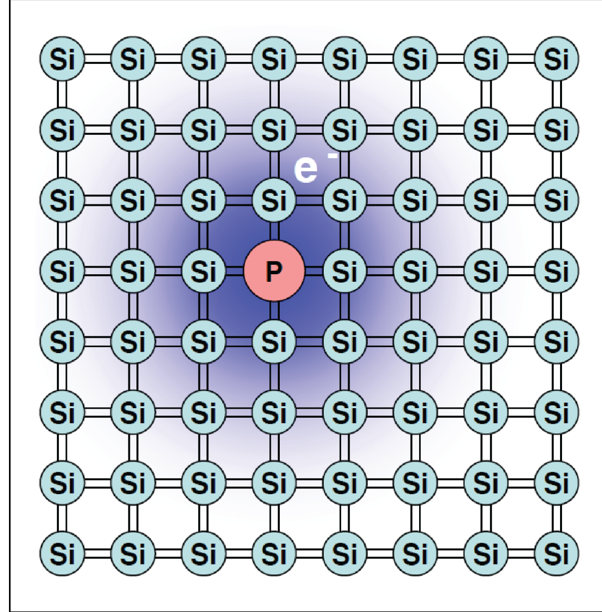

Figure 3.1: Schematic of the effect, when a silicon atom is substituted by a phosphorous atom. (Picture from R. Gross, Festkörperphysik/Halbleiterphysik)

The fifth impurity electron cannot participate in bonding between the silicon atoms; however, it still interacts with the coulomb field of the excess proton. The electron-proton coulomb interaction within the silicon matrix can be modeled as a hydrogen atom that has been screened by the lattice. The wavefunction of a donor electron is of the form of a Bloch function that has been modulated by a hydrogenic envelope function localized at the defect center. Such donors are therefore frequently referred to as hydrogenic, or shallow level impurities. The energy states of an electron interacting with a proton in a hydrogen atom are given by [11]:

$$E_n = \frac{1}{n^2}\frac{m_0 e^4}{8\epsilon_0 h} \tag{3.1}$$

where n is the main quantum number. As the electrons are not moving in the vacuum but in the semiconductor, the free electron mass m_0 is modified by the lattice structure [11]:

$$m^* = \hbar^2[\frac{d^2E}{dk^2}]^{-1} \tag{3.2}$$

where E is the energy at the conduction band edge. As the energy in the region of the lower conduction band edge can be approximated by a parabolic function, m^* is constant with respect to the wave vector k. The conductive effective mass of an electron in Silicon is $m^* = 0.26 \cdot m_0$.
The screening of the electron-proton interaction can be accounted for by the static dielectric constant of silicon. The relative static dielectric constant is a complex function of position within in the unit cell, and depends upon the charge polarization due to the proton-like impurity center, the valence band electrons localized in bonds, and the weakly bound donor electron. The average dielectric constant ϵ_{Si} can be used as an approximation, however, if the electron probability density is assumed to be widely spread over many thousand lattice points. The energy states of donor states can be written as:

$$E_n = \frac{1}{n^2} \frac{m^* e^4}{8\epsilon_0 \epsilon_{Si} h} \tag{3.3}$$

Furthermore, the radius of the donor state a_1 is determined from the Bohr orbit of a hydrogen atom a_0:

$$a_1 = \frac{m_0}{m^*} \epsilon_{Si} a_0 \tag{3.4}$$

$a_0 = 0.53$ nm is the first Bohr orbit. For silicon, the radius of the donor is about 30 nm and is extended over several lattice constants. Therefore, the use of the average dielectic constant is justified in terms of the screening.

3.2 The Poole-Frenkel effect

In this section, the potential of the shallow donor is debated in the presence of an electric field. As mentioned in the previous section the potential of the shallow donor state is described by the hydrogen atom, which is modified by the permittivity of silicon:

$$V(r) = -\frac{q^2}{4\pi\epsilon_0 \epsilon_{Si} r} \tag{3.5}$$

The potential distribution changes, when the donor state is exposed to an electric field:

$$V(r) = -\frac{q^2}{4\pi\epsilon_0 \epsilon_{Si} r} - \left|\vec{E}\right| r \tag{3.6}$$

In this case the potential distribution does not follow a pure $1/r$-characteristic. In figure 3.2 the potential distribution for a shallow donor is shown for $\left|\vec{E}\right| = 0\ \frac{\text{kV}}{\text{cm}}$ and $\left|\vec{E}\right| = 5\ \frac{\text{kV}}{\text{cm}}$. The electric field causes a local potential maximum, which defines the barrier height. The barrier is lowered and is determined by [21]:

$$E_{PF} = e\sqrt{e\left|\vec{E}\right|/\epsilon} \tag{3.7}$$

The barrier lowering is called the Poole-Frenkel effect. The binding energy of the phosphorous shallow donor state in silicon is $E_b = 45.7$ meV. It is reduced by about 20 meV, when the donor state is exposed to an electric field of $\left|\vec{E}\right| = 5\ \frac{\text{kV}}{\text{cm}}$.
At cryogenic temperatures, in the temperature range of 5 K to 40 K, the thermal energy is $k_B T = 0.4$ meV to $k_B T = 3.2$ meV. This is much lower than the binding energy, which has the consequence, that the electrons occupy the ground state. The Poole-Frenkel effect has influence on the thermal excitation of the electrons into the conduction band. This property can be observed in BIB structures as discussed in chapter 5. As well, besides thermal excitation, at sufficiently high electric fields, the electrons can tunnel into the conduction band. This feature is exploited to reset the DEPFET at cryogenic temperatures as discussed in chapter 6 in detail.
The interaction of the shallow donor state with the electric field is fundamental for the discussion of the device physical effects of the BIB structure and the DEPFET at cryogenic temperatures. It is used, when different physical mechanisms are discussed, such as electric field dependent emission from donor states and recombination into these states.

3.3 The metal-insulator transition

The hydrogen model is only valid, when the distance between the ground states of the donors exceeds the size of the donor. As the doping concentration in the silicon material increases the distance between the donors decreases. When the distance reaches the diameter of a donor, the states correlate with each other.
For the further discussion, n-doped silicon is considered and its impact on the conductivity at cryogenic temperatures. It is distinguished between three regimes of doping. The insulating, the metallic and an intermediate regime are illustrated. Some parts of the following subsections are extracted from the PhD-thesis of B.L. Cardozo [1].

[1] Title: *GaAs Blocked-Impurity Band Detectors for Far-Infrared Astronomy*

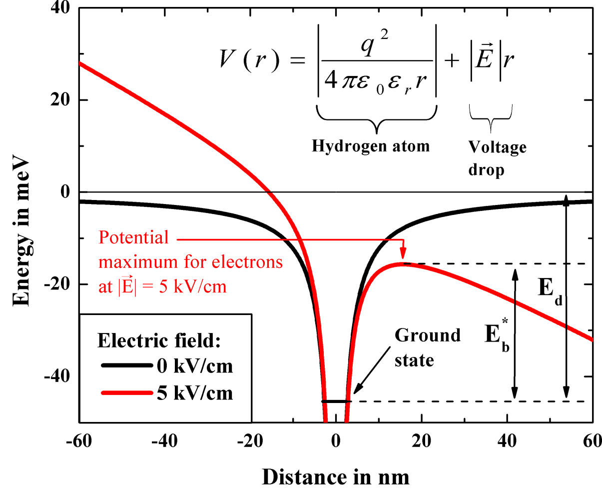

Figure 3.2: Potential of one shallow donor state at an electric field of 0 $\frac{\text{kV}}{\text{cm}}$ and 5 $\frac{\text{kV}}{\text{cm}}$. The binding energy is reduced by E_{PF}.

3.3.1 Insulating regime

$N_D < 10^{17}\ \frac{1}{\text{cm}^3}$

"Hydrogenic impurities, in the limit of low concentration, create discrete electronic energy states within a semiconductor host. These states typically occupy the forbidden energy gap near the band edges. The low temperature electrical properties of a doped semiconductor depend greatly upon the concentration of both the majority and minority impurity species. Considering the case of donor impurities with no compensating acceptors electrical conduction can occur via two mechanisms. The first is the thermal excitation of a bound electron (by absorption of an acoustic phonon) into the conduction band. The conductivity due to this mechanism depends exponentially on the ratio of the donor electron binding energy E_D to the available thermal energy k_BT. At very low temperature, the thermal energy required for electronic excitation into the conduction band is not available and all donor states will be occupied by electrons." Extrinsic photodetectors base on this material as described in section 1.4.

3.3.2 Intermediate regime

$10^{17}\ \frac{1}{\text{cm}^3} < N_D < 3 \cdot 10^{18}\ \frac{1}{\text{cm}^3}$

"In the presence of compensating acceptor impurities a second conduction mechanism becomes active. The minority acceptors will be ionized by electrons, creating an equal

number of ionized donors. Under an applied electric field, an electron in a neutral donor state can move to a neighboring empty site via the absorption and subsequent emission of a phonon." This is called hopping conduction and the conductivity can be formulated as:

$$\sigma = \sigma_0 \exp(-E_A/k_B T) \tag{3.8}$$

where E_A is the activation energy to transfer one bounded electron to a free vacant site of a donor state. Thus, the shallow donors beneath the conduction band form an impurity band, which is a conductive band even at low temperatures. One example for a device in this concentration regime is the active layer of a BIB structure (section 2.1). It is important to have a conductive impurity band, where one state can only be occupied by one electron. The blocking layer inhibits the conduction of the impurity band. When biased, the electrons fill the ionized donors, which results in neutral donors and ionized acceptors. Therefore, the space charge is defined by the lower concentrated ionized acceptors.

3.3.3 Metallic regime

$N_D > 3 \cdot 10^{18} \, \frac{1}{\mathbf{cm}^3}$

"When the doping is increased beyond a critical value that depends upon the semiconductor and dopant species under study, the conductivity switches to metallic character." The degeneration is abolished and no single states do exist. The impurity band can provide two free states for each electron (spin up and spin down). The impurity band rises in energy with increasing doping concentration and merges with the lower conduction band edge. The Fermi level is the energy, where the electron has its highest energy at $T = 0$. Semiconductors in this doping regime are used as ohmic contacts. By implanting a high dose of $10^{15} \, \frac{1}{\text{cm}^2}$ with an energy of 50 keV on a silicon wafer an ohmic contact with a thickness of about 100 nm and a peak concentration of $10^{20} \, \frac{1}{\text{cm}^2}$ is formed.

3.4 Mobility

In this subsection the transport behaviour of the electrons in the conduction band at a certain electric field is reported. This is given by the mobility μ, which is defined as follows:

$$\mu = \frac{v}{|\vec{E}|} \tag{3.9}$$

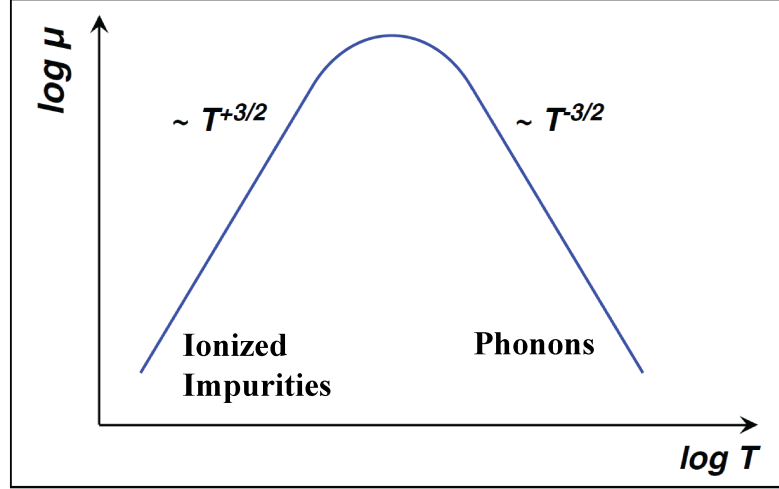

Figure 3.3: Qualitative plot of the mobility against the temperature. Acoustic phonon and impurity scattering are accounted for. (Picture from R. Gross, Festkörperphysik/Halbleiterphysik)

The mobility is a function of the electric field, temperature and doping concentration. In the following, a qualitative overview of the mobility is given in dependence of the temperature and a detailed description via the Boltzmann transport equations is disclaimed [22]. The Drude model is applied, where the electrons are accelerated in the presence of an electric field until it scatters with a phonon, lattice atom, etc. During scattering the velocity slows down and after the scattering process the acceleration by the electric field continous. This is repeated several times with short time constants. Therefore, this process can be summarized in a macroscopic constant velocity. The mobility is proportional to the scattering time:

$$\mu = \frac{e\tau_s}{m^*} \tag{3.10}$$

τ_s is the average time between two scattering processes and is given by:

$$\frac{1}{l} = \frac{1}{\langle v \rangle \tau} \propto S \tag{3.11}$$

S is the scattering cross-section and l is the mean free path of the electron. In contrast to metals, where $v = v_F$ is used, the mean value of all electrons in the conduction and valence band has to be taken to get $\langle v \rangle$. In semiconductors the Boltzmann-statistics can be applied and the average velocity $\langle v \rangle$ is determined to:

$$\frac{1}{2}m^{*}\langle v\rangle^{2}=\frac{3}{2}k_{B}T \tag{3.12}$$

$$\Rightarrow \langle v\rangle \propto \sqrt{T} \tag{3.13}$$

The scattering on acoustic phonons is discussed. For the scattering cross-section one obtains [11]:

$$S_{ph}=T \tag{3.14}$$

With the equations 3.11, 3.13 and 3.14, the mobility is given by:

$$\mu_{ph}=T^{-3/2} \tag{3.15}$$

Then, the scattering of the electrons on ionized defects is discussed. Because ionized donors and acceptors belong to those defects, this effect is very important for semiconductors. It can be described by the Rutherford scattering problem:

$$S_{def}\propto\langle v\rangle^{4}\propto T^{-2} \tag{3.16}$$

where $\langle v\rangle \propto \sqrt{T}$ is the thermal mean-value of the velocity. Again, from the equations 3.11 and 3.13 the following relation is derived:

$$\mu_{def}=T^{3/2} \tag{3.17}$$

The entire mobility can be derived by the Matthiesen-rule, where the reciproces of the mobilities are added:

$$\mu=\frac{\mu_{ph}\mu_{def}}{\mu_{ph}+\mu_{def}} \tag{3.18}$$

At low temperatures the mobility increases with $T^{3/2}$ and comes to a maximum. Then it decreases with $T^{-3/2}$ as shown in figure 3.3.

Chapter 4

The investigation of the DEPFET at cryogenic conditions

Two kinds of measurements were performed to prove the functional principle of the DEPFET. First, input and output characteristics give information about the transistor properties of the p-MOSFET. Furthermore, the effective mobility of the holes in the transistor channel is extracted from the slope of the input characteristics. Second, the spectroscopic measurements with x-rays originating from a ^{55}Fe source allows to investigate the complete functional principle of the DEPFET. In this connection, the clear performance and the intrinsic amplification were debated.

4.1 Setup for the DEPFET

For the investigation of the DEPFET under cryogenic conditions the DEPFET chip is thermally seperated from the whole readout electronics. It is necessary as the complex readout electronics cannot work properly at these extreme conditions. Therefore, it must be operated at room temperature. It is required to cool down only the device under test, which is the DEPFET chip.
The DEPFET is mounted in a liquid helium cryostat, where temperatures of 4.5 K can be achieved. A single pixel DEPFET, which is embedded in a small linearly structured matrix of 32 x 24 pixels was investigated at temperatures down to 6 K. A three dimensional schematic of one pixel is shown in figure 2.3. The sensitive thickness of the sensor is 450 μm.

4.1.1 Thermal control

The DEPFET chip is mounted on the ceramic, which is integrated in the cryostat and has contact to the temperature reservoir of 4.2 K (see figure 4.1). The bottom is cooled with liquid helium. To achieve higher temperatures the chip on the ceramic can be heated up by driving a current through the heat resistance, which is fixed at the mounting device next to the hybrid as shown in figure 4.2. The temperature is determined at the mounting device with a cryogenic temperature sensor [1]. It is controlled by a feedback loop between the measured temperature at the mounting device and the amount of dissipated power of the heat resistance. The mounting device is made of stainless steel to suppress heat flow to the temperature reservoir of 4.2 K and to prevent an excess evaporation of the liquid helium. Therefore, this configuration allows to measure at relatively high temperatures from 6 K to 300 K (relative to the temperature of liquid helium of 4.2 K).

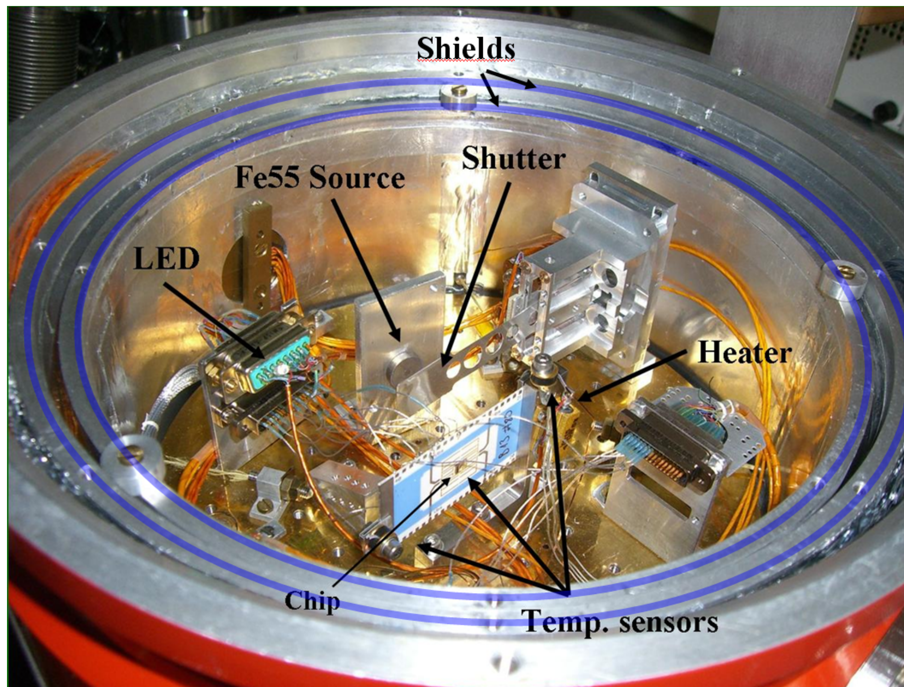

Figure 4.1: The cryostat is equipped to characterize the DEPFET at a temperature range from 4.5 K to 300 K. The bottom has contact with liquid helium and cools down the connectors, carriers, ^{55}Fe source and the shutter. The temperature of the shields are 20 K, 77 K and 300 K to prevent heat radiation from outside.

[1] Cernox (CX-SD) thin film resistance cryogenic temperature sensor from Lakeshore

Because of the easy implementation for the mounting device stainless steel as a bad thermal conductor was used. The cooling from room temperature to cryogenic temperatures requires two days and occurs via two cooling steps. In the first step the bottom is cooled down to liquid nitrogen (77.2 K) and in the second step liquid helium (4.2 K) is used. Equilibrium is achieved when the temperature at the mounting device is constant at 6 K. The cryostat has two thermal shields which isolate the chip from heat radiation. The electrical cables to the electronics outside the cryostat are made of stainless steel to suppress heat conduction. Temperature stability in the range of 10 mK are obtained. Under those conditions it is possible to perform stable temperature dependent measurements. Additionally, the temperature was measured with an on-chip pn-diode, which is located about 500 μm next to the DEPFET structure. It is a pn-diode, which is forward biased at a constant current. The voltage drop is measured and is plotted against the temperature as shown in figure 4.3. It can be observed that the voltage follows a linear behaviour in terms of the temperature. This can be explained by the current equation for a forward biased pn-diode:

$$I = I_0 \cdot [\exp(\frac{U}{k_B T}) - 1] \tag{4.1}$$

$$\Rightarrow U = [k_B \cdot \ln(\frac{I}{I_0} + 1)] \cdot T \tag{4.2}$$

Equation 4.2 is valid predominantly for room temperature. In general, pn-diodes show a kink in the linear plot in the temperature regime from 20 K to 30 K [23]. Freeze-out effects of the free charge carriers leads to an increase of the voltage drop. It was shown that pn-diodes have a persistent linear behaviour at cryogenic and room temperature, when the junction is heavily doped [24]. This is the case for the DEPFET temperature diode.

4.1.2 Readout

For spectroscopic measurements, the DEPFET signal is further amplified outside of the cryostat. For this, the Single Pixel Board (SPIX-Board) [17] is used, which was developed for the investigation of a large variety of DEPFETs. This measurement setup allows to investigate the DEPFET in dependence of the temperature, integration time, applied voltages and pulse duration generated from the SPIX-Board.
The amplification of the DEPFET output is processed with two amplification stages. The first stage is a current-voltage converter and the second an inverting amplifier as shown in figure 4.4. The bandwidth is further reduced by a low-pass after each amplifier stage.

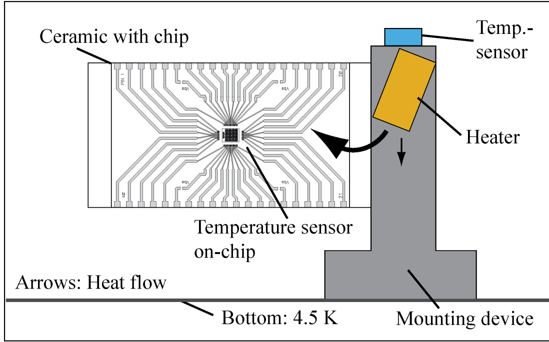

Figure 4.2: Setup of the ceramic in the cryostat. The heater and the temperature sensor are fixed at the mounting device, which is made of stainless steel.

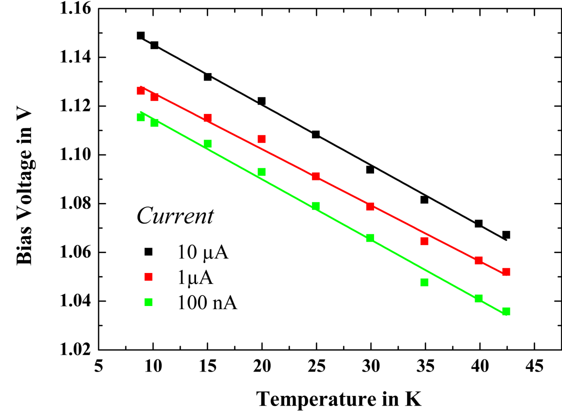

Figure 4.3: Measured characteristic of the integrated temperature diode of the DEPFET. Shown is the voltage drop of a forward biased pn-diode in dependence of the temperature for different currents. At cryogenic conditions the voltage is a linear function of the temperature.

This configuration is feasible to achieve a low input capacitance and output impedance to drive the analog digital converter (ADC). The source-drain voltage V_{SD} of the DEPFET is kept constant, so the change of the channel conductivity is connected with the change of the current. The entire current I_{Ent} across the transistor consists of the base current I_{Base} and the current, which is induced by the electrons in the internal gate I_{Meas}:

$$I_{Ent} = I_{Base} + I_{Meas} \tag{4.3}$$

with

$$I_{Meas} = g_q \cdot q. \tag{4.4}$$

q is the amount of charge in units of electrons and $g_q = \frac{\partial I}{\partial q}$ is the charge amplification of the transistor. This is a function of the transistor geometry, the drain current and operating conditions. With linearly structured DEPFETs with a gate length of 5 μm a g_q of 700 $\frac{\text{pA}}{\text{e}^-}$ has been achieved. The increase of the current is proportional to the amount of electrons in the internal gate.

The operation of the DEPFET requires several modules as shown in figure 4.5:

1. The cryostat The cryostat is the core of the setup. The DEPFET chip on the ceramic is mounted as described in the previous section. It is irradiated with x-rays originating from an ^{55}Fe source to generate free signal charges in the bulk. A shutter ensures, that the x-ray photons do not hit the sensor, if this is desired in the experiment. The shutter is constructed for cryogenic applications, where the positions Open/Close are controlled by magnets made of coils. The temperature sensor and the heater are used for the thermal control. The output of the DEPFET, being the drain contact, is connected with the readout board (figure 4.4) outside the cryostat. The readout board is one part of the SPIX measurement setup. The DC input voltages for the DEPFET come from the power supplies. The multiplexer board and the pulse generator provide the pulsed voltages for the clear and clear gate contacts.

2. The SPIX setup The SPIX setup represents the central electronic unit of the setup. The readout board is integrated, which is used to further amplify the DEPFET output signal. The output of the readout board (ROB) is digitalized with the ADC, which is integrated in the PC. Additionally, the multiplexer (MUX) board is integral part of the SPIX board and provides the pulsed voltages. The clear and clear gate contacts at the DEPFET are connected with the MUX board. During the clear process the contacts are pulsed to high voltages of up to 20 V to remove the electrons from the internal gate. The USB board is the central element to organise the trigger signals for the analog digital converter (ADC) and the MUX board. The sampling of the output by the ADC must be correlated with the clear process. A scheme for readout is shown in figure 4.6 and is called the correlated double sampling (CDS) technique. With CDS the output is measured twice, after reseting the collected signal electrons (sample-nr. 1) and after the collection time (sample-nr. 2). The difference of the measured states is proportional to the amount of the collected signal electrons. This method allows to measure the signal height with reference to the empty internal gate. Thus the reset respective kTC noise is completely absent. A detailed description of the SPIX setup is given in [17].

3. The external devices The external devices are instruments to feed the DEPFET and the MUX board with analog voltages. Additionally, the oscilloscope is used to observe the output signal of the DEPFET during the measurement. Instead of using the MUX board, the pulse generator can be alternatively applied to provide pulsed voltages for the clear and clear gate contacts.

4. The PC The output of the readout board is digitalized with the ADC, which is integrated in the PC. The PC is used to process the output of the ADC; additionally

it is needed to control the trigger signals from the USB board. As shown in figure 4.6, the ADC samples and the time points of the clear pulses must be correlated to measure the signal height. Via software it is possible to set the duration and the time points for the trigger signals.

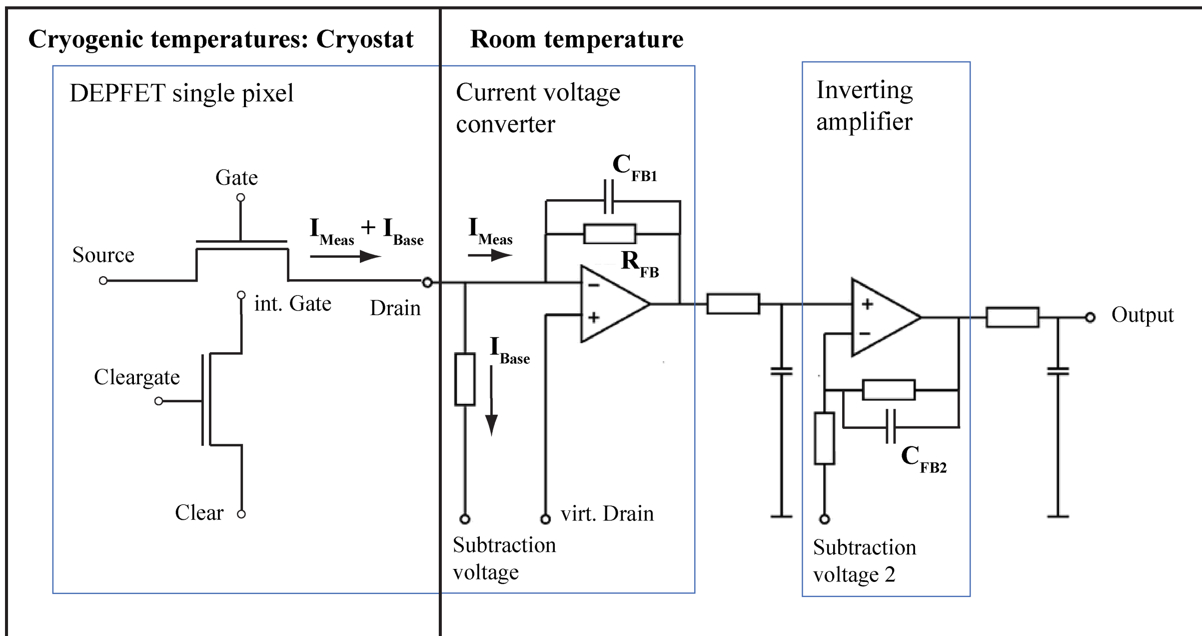

Figure 4.4: The drain-readout concept foresees a current-voltage converter at the drain contact. The drain node at the non-inverting input at the operation amplifier is kept fixed. The change in conductivity is equivalent with the change of current. The output voltage of the signal is given by the transistor current multiplied with the feedback resistor.

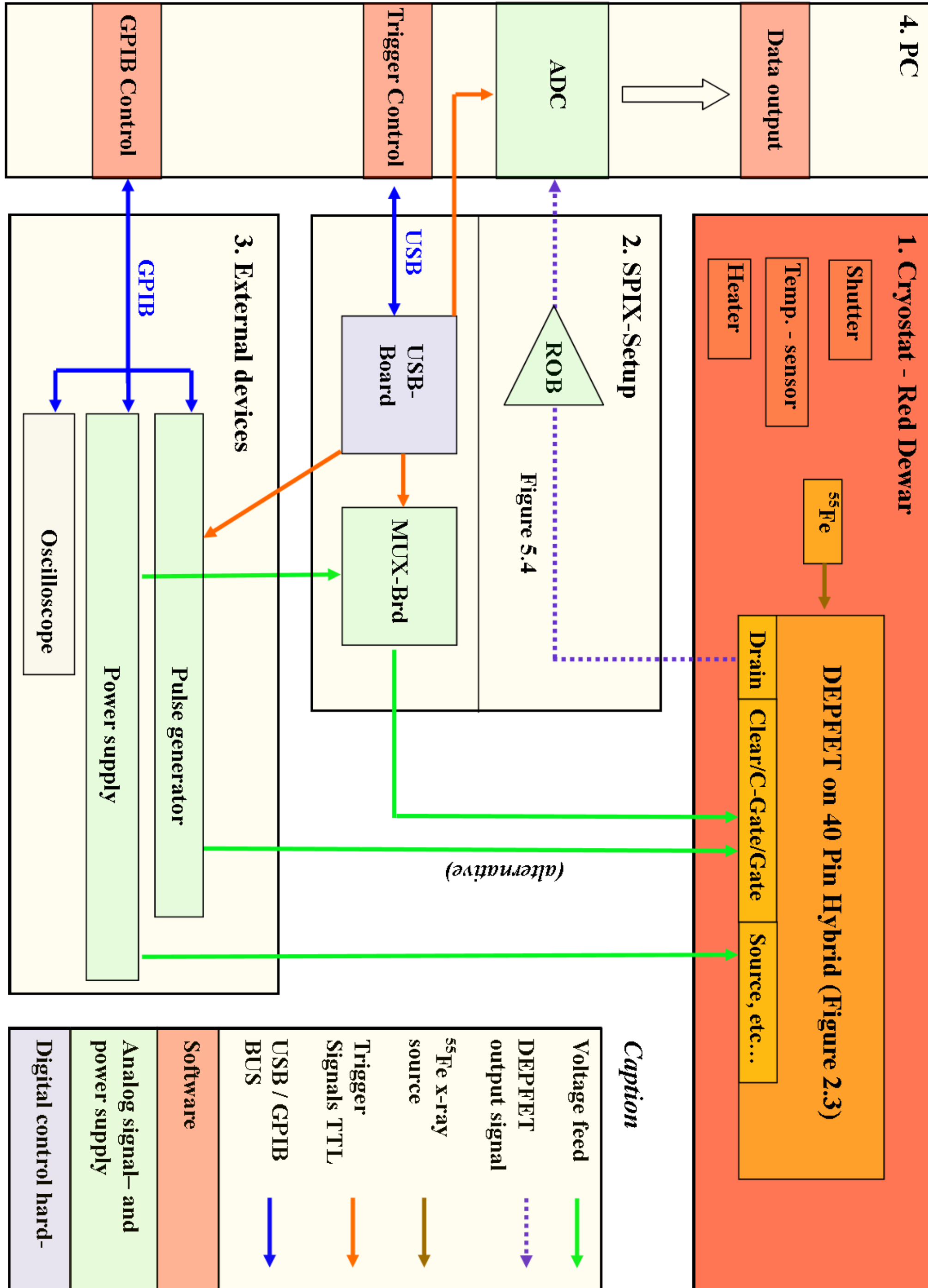

Figure 4.5: Schematic of the DEPFET-setup. It describes the interaction between the software, the analog signal- and power supply and the digital control hardware. The whole setup is subdivided in four components: 1. The cryostat, where the DEPFET chip is mounted on a cold plate and can be irradiated by a ^{55}Fe source. 2. The SPIX-setup, where the output signal of the DEPFET is processed and the USB board provides the trigger signals for the MUX-Board. 3. External devices. The power supplies and the pulse generator yield the analog voltages for the DEPFET in the cryostat. With the oscilloscope, the output voltage of the readout out board is observed. 4. The PC, where the software processes the incoming data from the ADC, edits the trigger signals for the USB board and the GPIB signals for the power supply, pulse generator and the oscilloscope.

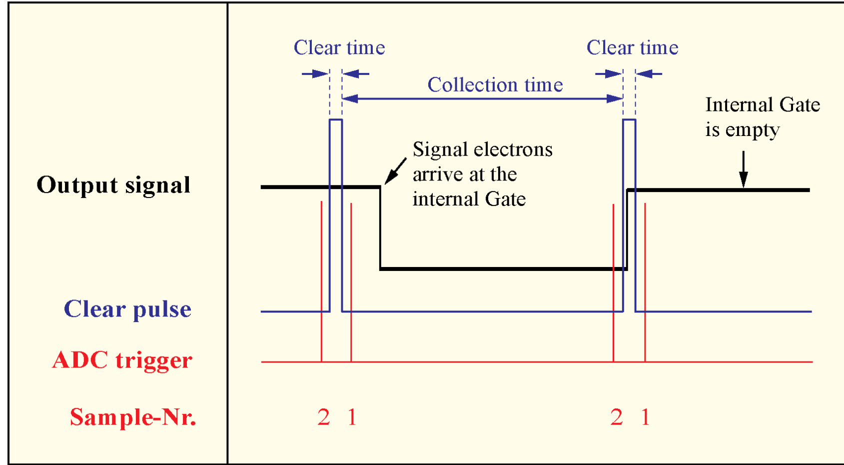

Figure 4.6: Schematic of the CDS. Sample 2 is taken after collection. Sample 2 measures the state, when the internal gate is empty. The difference gives the signal height. The sensor can be calibrated with a ^{55}Fe-source.

4.2 Characterisation of the p-MOSFET

Temperature dependent characteristic measurements were performed from 5 K to 300 K. First results are shown in figure 4.7. The input characteristics show a threshold voltage shift up to $\Delta V_T = (1.8 \pm 0.1)$ V at 5.8 K. Also, the slope is steeper with lower temperature showing the rise of the transconductance g_m. In the saturation regime the transconductance can be written as [25]:

$$g_m(T) = \frac{\partial I_D}{\partial V_{GS}}|_{V_D=const.} \propto (V_{GS} - V_T) \cdot \mu_{eff}(T) \tag{4.5}$$

where I_D is the drain current, V_{GS} is the gate-source voltage and V_T is the threshold voltage. According to the above formula, the effective mobility is proportional to the transconductance at constant $V_{GS} - V_T$. In figure 4.9 the function is plotted against the temperature at $V_{GS} - V_T = 2$ V. Increasing mobility at lower temperatures, down to 80 K, was already measured from other groups [26]. It shows, that the transconductance, and consequently the effective mobility, increases with decreasing temperature, which should be shown in an increase of the transistor current. However, a higher current with higher temperature in the output characteristics (figure 4.8) is observed. This reflects the threshold voltage shift, because at a lower temperature a higher gate-source voltage is needed to form the inversion layer in the source-drain channel.
The shift of the threshold voltage is explained by the displacement of the Fermi level E_F

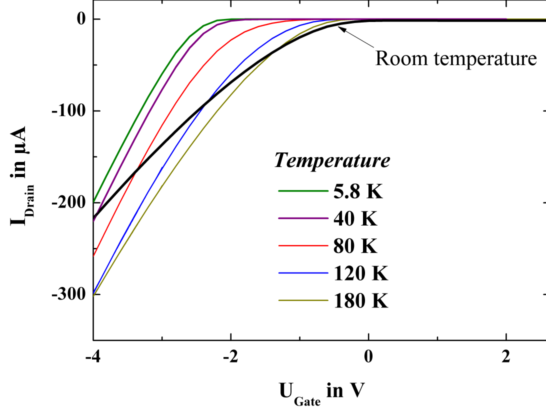

Figure 4.7: Measured input characteristics of the DEPFET for different temperatures. $V_{source} = 0$ V, $V_{drain} = -5$ V. The measurements are performed at $V_{clear} = V_{cleargate} = 9$ V.

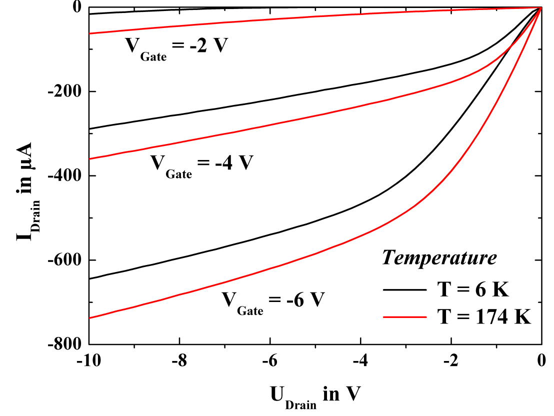

Figure 4.8: Measured output characteristics of the DEPFET for different gate voltages at 6 K and 174 K. The measurements are performed at $V_{clear} = V_{cleargate} = 9$ V.

at cryogenic temperatures relative to room temperature. The threshold voltage is given by [25]:

$$V_T = V_{FB} + 2\phi_B + \frac{\sqrt{2\epsilon_s \epsilon_0 q N_A (2\phi_B)}}{C_{SiO_2}} \tag{4.6}$$

where V_{FB} is the flat band voltage, $\epsilon_s = 11.7$ is the permittivity of silicon, ϵ_0 is the permittivity of the vacuum and $N_A = 10^{17}\ \frac{1}{\mathrm{cm}^3}$ is the concentration of the shallow p-implantation. C_{Si0_2} is the capacity per unit area of the gate:

$$C_{Si0_2} = \frac{\epsilon_{SiO_2} \epsilon_0}{d_{SiO_2}} = 1.08 \cdot 10^{-4}\ \frac{\mathrm{F}}{\mathrm{m}} \tag{4.7}$$

with $\epsilon_{SiO_2} = 2.2$ being the permittivity of silicon dioxide and $d_{SiO_2} = 180$ nm the thickness of silicon dioxide. ϕ_B is the bulk potential with:

$$\phi_B = E_F - E_i \tag{4.8}$$

At room temperature the Fermi energy in a p-doped material is in the middle of the band gap of silicon. The Fermi energy decreases with decreasing temperature and approaches

the upper valence band edge at cryogenic temperatures [25]. It is a strong function of the impurity concentration and one obtains for the bulk potential at cryogenic and room temperature $\phi_{B,6K} = 0.55$ eV and $\phi_{B,300K} = 0.45$ eV respectively [25]. It is assumed that the flat band voltage does not vary and $V_{F,300K} - V_{F,6K} = 0$. With these values and equation 4.6 it is possible to calculate the difference of the threshold voltage at 6 K and 300 K:

$$V_{T,300K} - V_{T,6K} =$$

$$= 2(\phi_{B,300K} - \phi_{B,6K}) + \frac{2\sqrt{\epsilon_s \epsilon_0 q N_A}}{C_{Si0_2}}(\sqrt{\phi_{B,300K}} - \sqrt{\phi_{B,6K}}) = -1.9 \text{ V} \tag{4.9}$$

As a result, the threshold voltage decreases with lower temperature by a value of 1.9 V, which coincides very well with the experimental value of $\Delta V_T = (1.8 \pm 0.1)$ V.
Low temperature effects such as impact ionization or freeze-out effects were not observed [27]. The lack of impact ionization is explained by the presence of doping impurities in the transistor channel. Between the source and drain contacts there is a shallow Boron implantation, which has a concentration of about $10^{17} \frac{1}{\text{cm}^3}$. At 5.8 K and in this concentration regime the scattering lifetime of the holes in the inversion layer is dominated by impurity scattering. In this case the mobility is in the range of $100 - 500 \frac{\text{cm}^2}{\text{Vs}}$ [28], which is lower than the mobility of valence band holes in intrinsic silicon. The mean free path of the holes is low so that they cannot gain sufficiently high energy to generate electron-hole pairs by impact ionization.

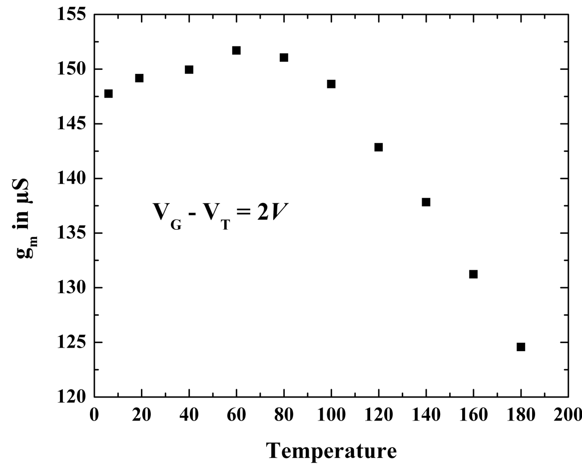

Figure 4.9: Experimentally determined transconductance in dependence of the temperature.

Additionally, freeze-out effects in the source-drain channel do not occur. By applying a negative voltage an inversion layer is created at the interface (figure 4.10). In this case the surface potential ϕ_s is twice the bulk potential $\phi_B = \mu - E_i$ [25]:

$$\phi_s = 2 \cdot \phi_B \tag{4.10}$$

where μ is the chemical potential and E_i the intrinsic potential. This equation is also valid for low temperatures [29]. Figure 4.10 also shows the bending of the valence band edge E_V of silicon near the oxide layer up to the depletion width d. The right diagram shows an enlargement of the band structure at the interface SiO_2/Si. At the interface, the upper valence band edge E_V is higher than the chemical potential μ in silicon. The chemical potential is located below the upper valence band edge, which results in a metallic character at the interface. The hole states of the thin conductive hole layer beneath the oxide are located in a triangular potential, which is formed by the oxide barrier and the valence band at the interface. This results in empty electron states in the valence band or free holes. The holes in the valence band are degenerated and are mobile along the interface. The electrons occupy the lowest energy states in the conduction band, which are below the chemical potential. Therefore, they cannot be trapped by any energetically lower states. As a result, freeze-out effects in the transistor channel do not occur and the transistor works similar to room temperature.

4.3 Spectroscopic measurements

The amplification and the clear performance of the sensor are characterized with spectroscopic measurements. The measurement setup and the readout scheme are described in section 4.1. The sensor is irradiated from the front side with x-rays. They originate from a ^{55}Fe source to generate free signal charges in the bulk. The diameter of the source is 3 mm.

In subsection 4.3.1 the sample schemes at cryogenic and at room temperature are described. They are necessary to understand the amplification and the clear performance, which are discussed in the subsections 4.3.2 and 4.3.3 respectively.

4.3.1 Sample schemes

In figure 4.11 the output voltage and the sampling schemes to determine the signal height V_{sig} of the ADC are shown. At room temperature, one clear pulse is needed to remove all signal electrons from the internal gate. After the integration cycle, where the signal electrons arrive in the internal gate, the output voltage goes to the baseline. Either the

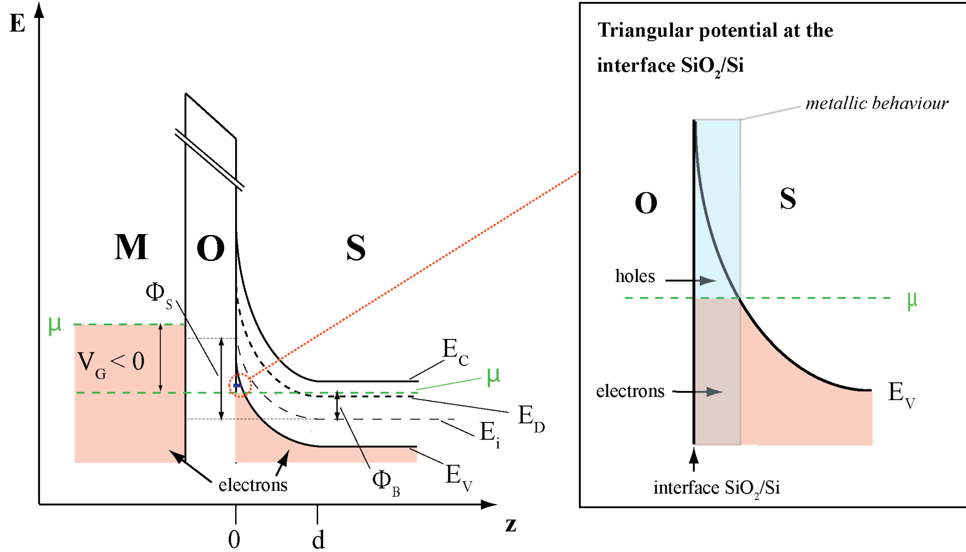

Figure 4.10: Band structure of a p-MOS, when a negative voltage is applied. The right diagram shows the enlargement of the bandstructure at the interface SiO_2/Si. As the chemical potential is below the upper valence band edge at the interface SiO_2/Si the material gets a metallic character in this regime.

output voltage is measured at the beginning and at the end of the collection time (sample scheme A); the difference is the signal voltage V_{sig}. Or the output voltage is measured before and after the clear pulse is applied (sample scheme B) and then, the difference is taken to obtain V_{sig}. However, at cryogenic temperatures, as the collected signal electrons in the internal gate cannot be removed completely by one clear pulse the output voltage does not reach the baseline. The reason for that is explained in the next subsection. Therefore, only with sample scheme B it is possible to determine the signal height [30]. The difference of the two sample values is the signal height V_{sig}:

$$V_{sig} = V_1 - V_2 \tag{4.11}$$

where V_1 and V_2 are the values of the samples at the beginning and end of the collection time in digital units. The sampling, which is needed to obtain the spectrum, is independent of the fill level of electrons in the internal gate and consequently to the clear performance.
Figure 4.12 shows a ^{55}Fe spectrum of the DEPFET at room temperature and at 6 K. At room temperature it is possible to distinguish between the K_α - and K_β - lines; it is more diffcult to identify the K_β - line at 6 K as it merges with the K_α - line. From these

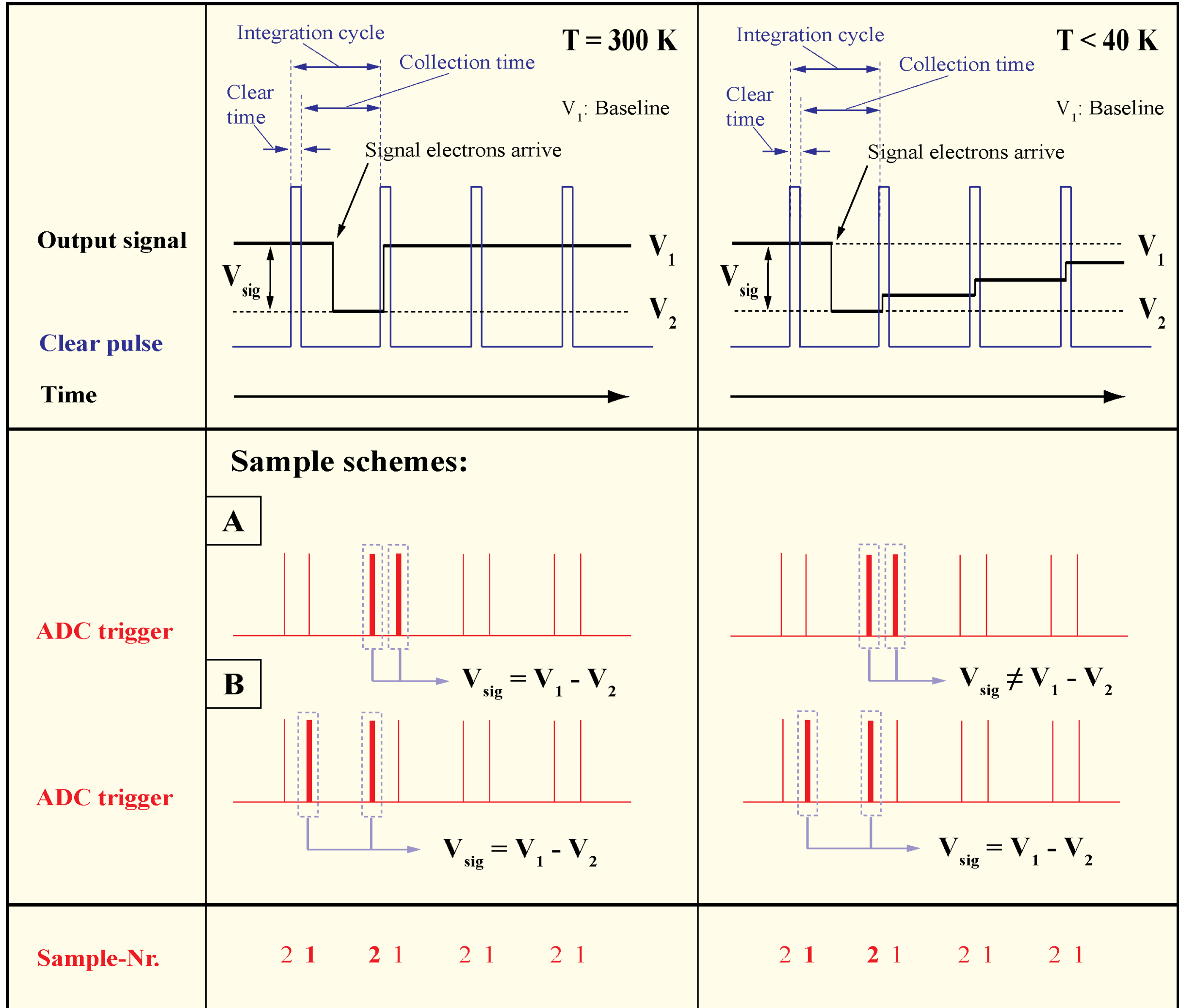

Figure 4.11: Output voltage and sample schemes of the DEPFET at 300 K and temperatures lower than 40 K. *Room temperature:* One clear pulse is needed to remove all signal electrons from the internal gate. After the integration cycle, where the signal electrons arrive in the internal gate, the output voltage goes to the baseline. Either the output voltage is measured at the beginning and at the end of the collection time (sample scheme A); the difference is the signal voltage V_{sig}. Or the output voltage is measured before and after the clear pulse is applied (sample scheme B) and then, the difference is taken to obtain V_{sig}. *Cryogenic temperature:* As the collected signal electrons in the internal gate cannot be removed completely by one clear pulse the output voltage does not reach the baseline. Therefore, with sample scheme A it is not possible to determine the signal height.

results following conclusions are drawn for the linearly structured DEPFET at cryogenic temperatures:

1. Signal charges are generated in the sensitive bulk.
2. The generated signal charges are collected at the readout node, which is the internal gate of the DEPFET.
3. The readout proceeds by an amplifier (p-channel MOSFET), which is steered by the charge collected in the internal gate.

The current at 6 K is chosen to be lower than 60 μA, otherwise it would heat up the device significantly. The amplification and the reset at cryogenic temperatures behave completely different from room temperature measurements, which are described in the following subsections in more detail.

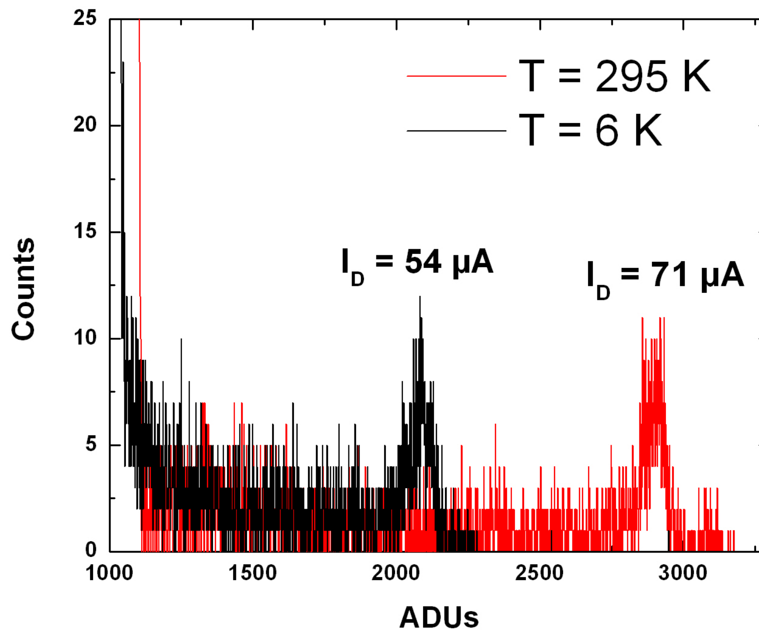

Figure 4.12: ^{55}Fe-spectrum at room temperature and at 6 K.

4.3.2 Clear performance

Figure 4.11 shows schematically the output voltage at cryogenic temperatures when a signal arrives. When signal electrons arrive at the internal gate, the output voltage drops to a lower voltage level. As the output voltage level reaches the baseline after several clear sequences, it is concluded that only few electrons from the internal gate after each clear pulse can be removed. In this case it is not possible to reach the baseline after one clear pulse. Individual signal charges are trapped in shallow donors, which are microscopic potential minima of several meV. They can be emitted with a time constant of several milliseconds. Experimentally, this is identified as the freeze-out of the signal charge. The thermal energy at 6 K is not sufficient to emit the signal charge from the microscopic potential minima into the conduction band in appropriate time constants.
The amount of the removed electrons N_{e^-} from the internal gate after one clear pulse can be calculated by:

$$N_{e^-} = \frac{\Delta V}{V_{sig}} = \frac{E_{K_\alpha}}{3.6\ \text{eV}} \cdot \frac{\Delta V}{X_{K_\alpha} - X_R} \tag{4.12}$$

where ΔV is the voltage jump after one clear pulse in digital units. One example is shown in figure 4.13 for $T = 30$ K, where the output voltage is shown in dependent of the number of clear pulses. Approximately 900 to 1000 clear pulses are needed to reach the baseline. The clear process is one of the crucial points to prevent internal gate overflow and proper baseline reset. For low noise measurements it is desirable to perform Correlated Double Sampling (CDS). For CDS, the drain current is sampled before the clear pulse and immediately after clearing the pixel. In this case the empty internal gate is the reference for the signal level. Calculations have shown, that the non perfect clear leads to an additional noise source. It was found out that the noise increases with an increasing number of non-cleared electrons in the internal gate [17].
At room temperature the clear efficiency is determined by the voltage level at the clear and clear gate [31]. Under cryogenic conditions, below 40 K, it was found out, that it is not possible to remove the signal charge by only switching the clear and the cleargate. Chapter six describes a new method, which makes it possible to clear the internal gate completely at cryogenic temperatures.

4.3.3 Amplification

The current amplification per electron g_q of the DEPFET was calculated, which can be determined from the location of the K_α-Peak in the spectrum:

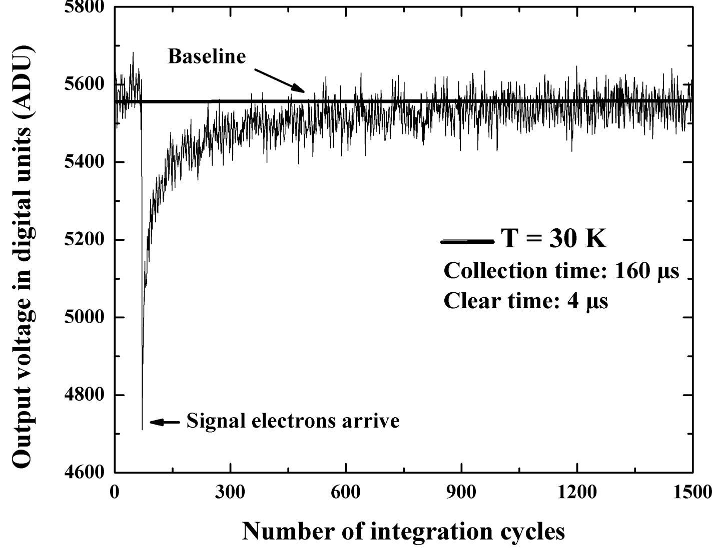

Figure 4.13: Measured output voltage of the DEPFET in dependence of the integration cycles at a temperature of 30 K. The collection time is 160 μs and the clear time is 4 μs.

$$g_q[\frac{\text{pA}}{\text{e}^-}] = \frac{X_{K_\alpha} - X_R}{\frac{E_{K_\alpha}}{3.6\text{eV}}} \cdot \frac{1}{f \cdot k} \quad (4.13)$$

with X_{K_α} being the position of the K_α - Peak and X_R the position of the noise peak in digital units. f is the amplification of the current-voltage converter in V/A, k is the conversion factor of the ADC in ADU/V and $E_{K_\alpha} = 5890$ eV is the energy of the K_α - Peak. The position of the peak at 6 K respective to room temperature is reduced by a factor of about two. The amplification is a function of the mobility μ and the Drain-source voltage in the saturation regime of the transistor V_{DS}^{sat} [32]:

$$g_q = \frac{\mu(T)}{L^2} V_{DS}^{sat} \quad (4.14)$$

The mobility is the only temperature dependent parameter. From section 4.2 the transconductance of the p-MOSFET is determined experimentally and as a result, the mobility in the transistor channel increases with decreasing temperature. Consequently, the amplification and the amplitude of the spectrum should be higher at 6 K. The presumption

of charge loss is not right, because the ratio of the peak-to-background is similar. Additionally, the distance between the K_α and the K_β - peak is also scaled with the relative position of the K_α peak. The reduced amplification at cryogenic temperatures is explained by the location of the signal electrons in the internal gate. The electrons are collected in the region, where the steering impact is low.
Experiments have shown that the signal electrons are trapped into the shallow phosphorous states. As shown in figure 4.13 these electrons can be removed from the internal gate after more than 1000 integration/clear cycles. However, there is a region in the internal gate where the electrons cannot be emitted into the conduction band. They are permanently trapped and are not removed from the internal gate. In this region the emission time exceeds the clear time by several orders of magnitude. As shown in figure 4.14 a) the region in the internal gate where the electrons are permanently trapped is the potential maximum in the collection state. It is located in the middle of the internal gate with respect to the x-axis at a depth of $y = 0.6$ μm. The potential maximum is not exactly in the middle with respect to the z-axis but is shifted to the more positive source contact ($V_S = 0$ V and $V_D = -5$ V). During the collection and the clear time, in this region the electric field is zero or close to zero leading to a weak impact of the Poole-Frenkel effect and consequently, the emission of the trapped electrons is heavily suppressed. In contrast, at room temperature, during the clear process, the electrons are in the conduction band, where they can diffuse to the higher field region near the clear contacts. At cryogenic temperatures, a non negligible amount of electrons stay permanently in the internal gate, which has two effects explaining the low amplification at cryogenic temperatures:

1. The trapped electrons generate mirror charges at the inversion layer leading to an increased current density $j_{froz}(x)$ in the middle of the internal gate (see figure 4.14 b)). The edge of the transistor channel is not affected because the electrons can be removed during the clear process as the electric field caused by the positive clear and clear gate contacts is significantly higher. The current equation 4.3 is modified with the increased current I_{froz} caused by the presence of the trapped electrons in the middle of the internal gate. Therefore, the entire current of the transistor I_{Ent} consists of a base current I_{Base} given by the boundary conditions of the transistor contacts, the current induced by the signal electrons I_{Meas} and the increased current I_{froz}:

$$I_{Ent} = I_{Meas} + I_{Base} + I_{froz} = I_{Meas} + I_{Base} + N \cdot g_q \tag{4.15}$$

with

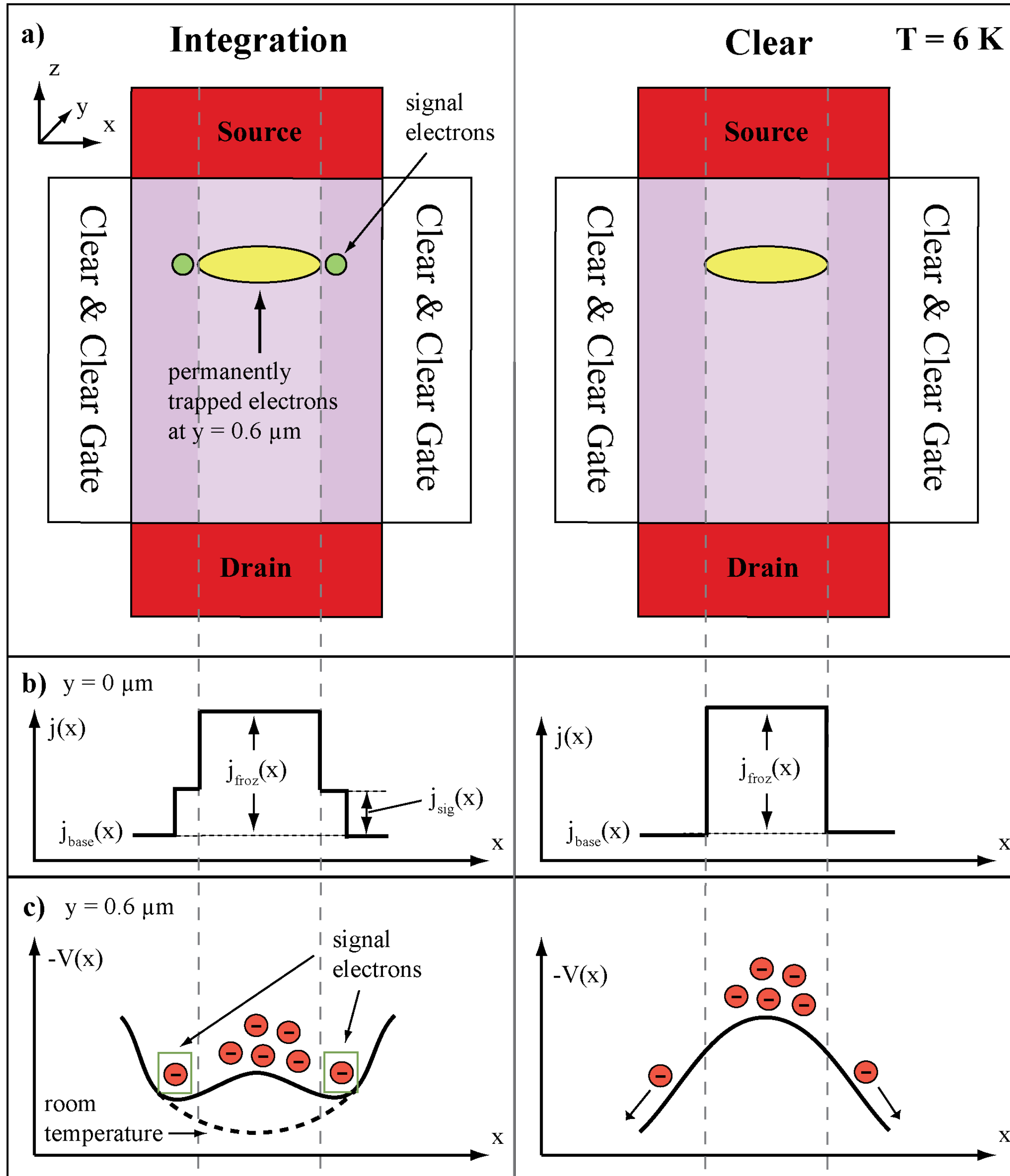

Figure 4.14: a) Schematic of the top view of the transistor during integration and the clear process. The yellow circle shows marks the region, where electrons are permanently trapped at a depth of y = 0.6 mm. The green circles is the region where the signal electrons, originating from the interaction of incident x-ray radiation with the bulk, are collected. b) Current density of the transistor along the x-axis. In the middle of the internal gate the current density is increased due to the permanently trapped electrons in the internal gate. c) Potential distribution of the internal gate along the x-axis at a depth of $y = 0.6\ \mu$m. The decreased potential in the middle of the internal gate caused by the negative space charge of the permanently trapped electrons forces the signal electrons to be collected at the edge of the transistor channel. Only these electrons can be removed from the internal gate during the clear process. The dashed line represents the potential distribution at room temperature, when no electrons are trapped in the middle of the internal gate.

$$I_{froz} = N \cdot g_q \tag{4.16}$$

and N being the number of trapped electrons.

2. The trapped electrons neutralize the positively charged ionized shallow donors which give rise to a repulsive potential for the electrons in the middle of the internal gate as shown in figure 5.14 c). The signal electrons, which originate from the interaction of the incident x-ray radiation with the bulk material, are not collected in the middle of the internal gate with respect to the x-axis. The collection region is at the edge of the transistor where they induce the measurable signal current I_{Meas} in the transistor channel. These electrons generate the positive mirror charges in the transistor channel, where the current I_{Base} flows. The amplification g_q is determined not by the entire transistor current I_{Ent} but by the lower base current I_{Base}.

With the amount of trapped electrons and the amplification at 6 K $g_{q,6K}$ it is possible to calculate the base current. Assuming that about 10^5 electrons are permanently stored in the internal gate. This value is the charge handling capacity of the detector. When reaching this amount of electrons in one pixel, it was shown that non-linear effects occur and the amplification is reduced [33]. These electrons are distributed in a volume of about 10 μm^3. The concentration of the electrons is $\frac{10^5}{10\ \mu\text{m}^3} = 10^{16}\ \frac{1}{\text{cm}^3}$, which is the phosphorous concentration of the internal gate. Therefore, every electron occupies one phosphorous donor state in the internal gate. The amplification at 6 K $g_{q,6K}$ can be calculated with equation 4.13 and has a value of 350 $\frac{\text{pA}}{\text{e}^-}$. From equation 4.16 the current induced by the trapped electrons I_{froz} is:

$$I_{froz} = N \cdot g_q = 10^5\ \text{e}^- \cdot 350\ \frac{\text{pA}}{\text{e}^-} = 35\ \mu\text{A} \tag{4.17}$$

The base current at 6 K is determined with equation 4.15:

$$I_{Base,6K} = I_{Ent,6K} - I_{froz} = 54\ \mu\text{A} - 35\ \mu\text{A} = 19\ \mu\text{A} \tag{4.18}$$

The effective steering current does not coincide with the transistor current as the signal charge steers the lower base current $I_{Base,6K}$ resulting in a reduced amplification $g_{q,6K}$. In general, the amplification g_q is proportional to the transconductance g_m, which is proportional to the square root of the transistor current I_{DS} [32]:

$$g_q \propto g_m \propto \sqrt{I_{DS}} \tag{4.19}$$

Therefore, the ratio of the amplification at 6 K and at 300 K is equal to the ratio of the square root of the respective base currents:

$$\frac{g_{q,6K}}{g_{q,300K}} = \sqrt{\frac{I_{Base,6K}}{I_{Base,300K}}} = 0.52 \tag{4.20}$$

This result coincides very well with the experimental value. It is found out experimentally that the K_α - line at 6 K is lower by a factor of 2 in terms of the K_α - line at 300 K as shown in figure 4.12. The trapped electrons are the reason that the signal electrons are collected in the region of the internal gate, where the steering impact is low. This leads to reduced amplification at cryogenic temperatures.

Chapter 5

The investigation of BIB detector test structures

For the first production of BIB structures single pixel chips were designed to investigate the physics of the device. Current-voltage characteristics in the operating mode of the BIB structure were performed to get information about the basic characteristic mechanisms. The readout of the BIB structure devices was not processed with the DEPFET on top of the blocking layer. The DEPFET was investigated seperately on a high resistivity silicon material as already described in chapter 4. In this chapter dark current measurements at different temperatures and bias voltages are presented.

5.1 Material and Design of the BIB structure device

The base material of our BIB structure device consists of antimony doped silicon (Si:Sb) with a doping concentration of greater than $10^{17}\frac{1}{\text{cm}^3}$. The blocking layer, which is an epitaxial layer of intrinsic Silicon on top of the wafer, was grown by the Institut für Mikroelektronik in Stuttgart. They used the Chemical Vapour Deposition technique and deposited an epitaxial silicon layer with a thickness of 5 μm. The concentration profile is determined by Secondary Ion Mass Spectrometry (SIMS) measurements which were performed by the company Evans Analytical Group (EAG) as can be seen in figure 5.1 left.

Figure 5.1 a) also shows the cross section of the layer structure with its contacts and the prepared layer structures (silicon dioxide and aluminum layers). The contacts for biasing at the front- and back side are shallow n^+- (phosphorous) implantations with doses of either $10^{15}\frac{1}{\text{cm}^2}$ or $5 \cdot 10^{13}\frac{1}{\text{cm}^2}$. A guard ring at the front side with the same implantation profile encloses the bias contacts. A shallow p^+- (boron) implantation between the guard ring and the bias contact on some chips is introduced in order to investigate the interaction

between a pn-diode and a BIB-diode. The metalization of all contacts consists of sputtered aluminum. The BIB structure chip is mounted on a ceramic as shown in figure 4.2.

5.2 Setup for the BIB structure measurements

BIB structure test structures were designed and produced as described in section 5.1. The question was, if the devices show the following properties:

1. The dark current is suppressed by the blocking layer and
2. impurity band conduction in the active layer occurs

Additionally, the question is asked, if other physical properties, such as intrinsic electric fields, can be characterized. Temperature dependent current-voltage characteristics give insight into these features. In order answer this question a setup was established, which has to fulfill certain requirements in terms of thermal control and biasing.

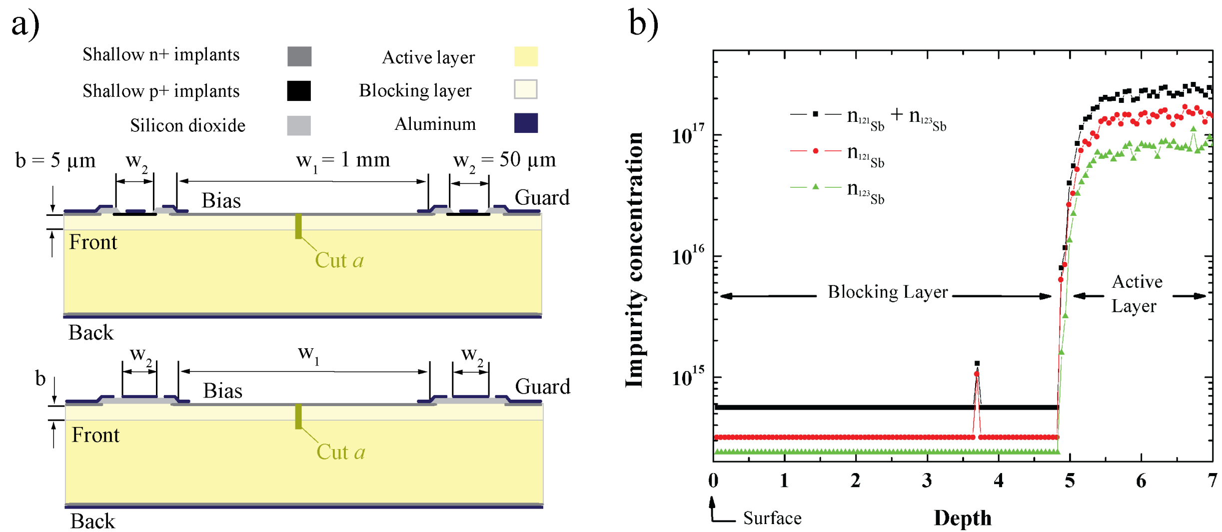

Figure 5.1: a) Design of two types of the BIB structure device with the basic structure in the center (bias) and the guard ring beside. The bias contact and the back side are shallow n^+-implantations. The contact, which is steered between the bias and the guard contact at the front side, consists of a shallow p^+-implantation or a silicon dioxide. b) Concentration profile of antimony of the BIB structure device along cut a. The heavily doped regime is the active layer.

5.2.1 Thermal control

The setup for the measurements of the BIB structures was designed to measure at cryogenic temperatures down to 4.5 K. The same cryostat[1] and mounting device as described in section 4.1 were used. The measurements are performed in the temperature range of liquid helium, which has a boilling point of 4.2 K. The device under test can be heated up to 30 K. Current-voltage characteristics are made in the dark, thus, no uncontrolled infrared light hits the detector. The inner shield of the cryostat has a temperature of 20 K and is source of background infrared light; therefore, an extra shielding for the chip was built as shown in figure 5.2. The temperature of the shielding is similar to the temperature of the bottom and is cooled down to 4.2 K.

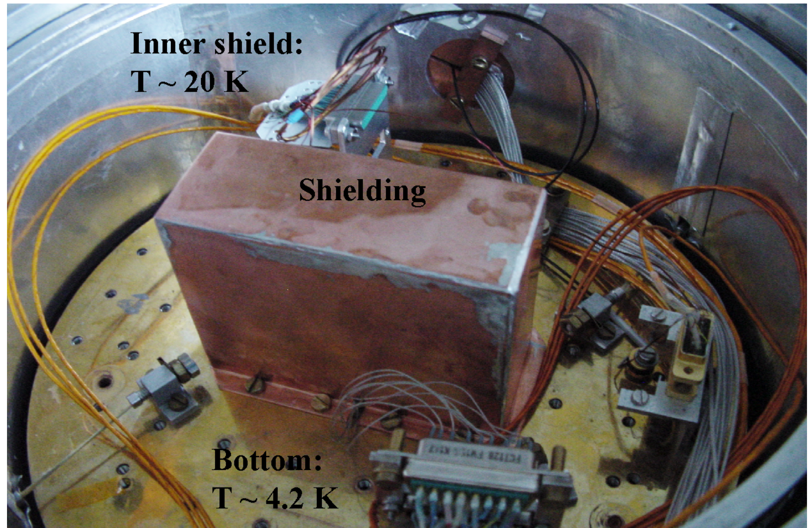

Figure 5.2: The cryostat is shown. The shielding for BIB structures is fixed with the bottom, which is cooled down to 4.2 K. The setup of the ceramic is similar to figure 4.2 and is mounted inside of the shielding.

5.2.2 Biasing and readout

Figure 5.3 shows the schematic of the circular BIB structure and the configuration of the applied voltages. The shallow p^+-implantation, which is called p^+-contact, surrounds the n^+ bias contact. The guard contact is a shallow n^+-implantation and surrounds the p^+-contact. The same voltage to the bias and the guard contact is applied. By shortening the bias and the guard contact it is ensured, that there is no voltage difference parallel to the surface. Consequently, no current flows from the guard contact or from the edge of the chip into the bias contact. In this biasing scheme the bias current is measured while the voltage at the p^+-contact is kept fixed.

[1] The shutter and the ^{55}Fe source are not part of the setup as they are not needed to investigate the BIB structures.

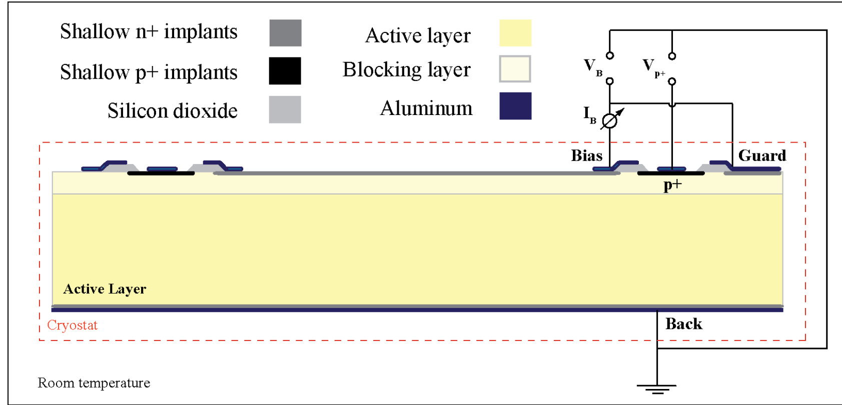

Figure 5.3: Schematic of the circular BIB structure and the position of the applied voltages are shown. The bias and the guard contacts are shortened. The voltage at the p^+-contact is kept fixed. The current is measured only at the bias contact.

5.3 Electron transport measurements

The investigation of the electron transport allows us to characterize basic properties of the device. One example is the suppression of the dark current by the blocking layer of the BIB structure device. Another characteristic is the impurity band conduction in the active layer. These features of our test structures are described in subsection 5.3.1. It is possible to get information about the intrinsic electric fields between the active and blocking layer as explained in subsection 5.3.2. In subsection 5.3.3 measurements of the dark current in dependence of the voltage of the p^+ contact are presented.

5.3.1 The blocking mechanism and impurity band conduction

The dark current of the BIB structure and the heavily doped material (same structure without blocking layer) were investigated as a fraction of temperature. The schematic is shown in figure 5.3. The p^+ contact is biased with -2 V, the bias contact is 0.2 V and the back contact is grounded. Figure 5.4 shows a semi-logarithmic plot of the dark current in dependence of $\frac{1}{T}$ of the BIB structure and the heavily doped silicon. As can be seen the current decreases with lower temperature. It is distinguished between two different temperature regimes:

1. **$T > 12$ K:**

   The origin of the dark current I_{dark} of both devices is the thermal excitation from the shallow donor states of the impurity band into the conduction band:

$$I_B = I_{dark} \propto exp(\frac{-E_b}{k_B T}) \tag{5.1}$$

where E_b is the binding energy of the shallow donor state in the active layer. Therefore, it is possible to determine E_b from the slope of the regression line (blue line in figure 5.4) of the Arrhenius-plot. It is expected that E_b coincides with the binding energy of a single antimony donor state, which has a value of 42.7 meV. The experimental value for the binding energy is $E_b = (27 \pm 1.1)$ meV, which does not correspond with the binding energy of a single Antimony donor state. The discrepancy can be explained by the reduction of the binding energy at high doping concentrations.

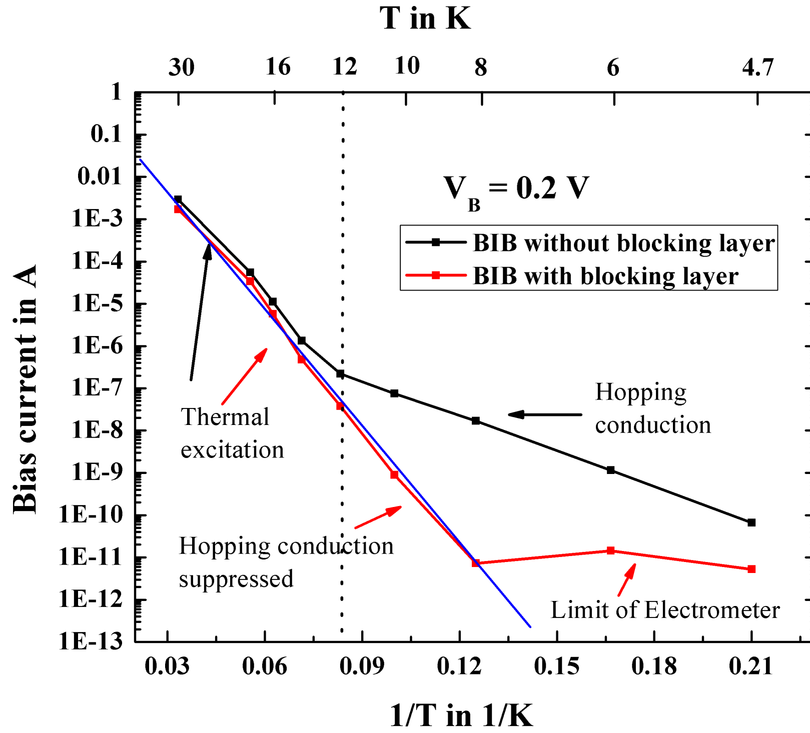

Figure 5.4: Measured dark current in dependence of $\frac{1}{T}$ (Arrhenius plot) of the BIB structure device with and without blocking layer at a bias voltage of $V_B = 0.2$ V. The blue line represents the regression line, which is needed to determine the slope. The left side of the vertical dotted line ($T > 12$ K) is the regime, where thermal excitation dominates in both devices. The right side side shows the dark current, where hopping conduction dominates (black curve) or is suppressed (red curve).

Figure 5.5 shows the energy band structure of low and heavily doped silicon. It demonstrates the mechanisms, which are responsible for the reduced binding energy in the high concentration regime. The active layer of the heavily doped silicon has a concentration of about $3 \cdot 10^{17} \frac{1}{\text{cm}^3}$ and the states are degenerated. The upper edge of the impurity band is closer to the conduction band than the state of a single donor. The impurity band width in dependence of the donor concentration was calculated by Baltensperger theoretically [34], [35]. The relative shift of the upper edge of the impurity band with respect to the state of a single shallow donor is $E_{imp} = 5.3$ meV. Additionally, the excited donor states also form impurity bands, which merge with the lower conduction band edge. Thus, the lower conduction band edge in a heavily doped material is even lower. The band-gap shrinkage $E_{c,low}$ was calculated theoretically in [36] and is 10 meV in the aforementioned concentration regime.

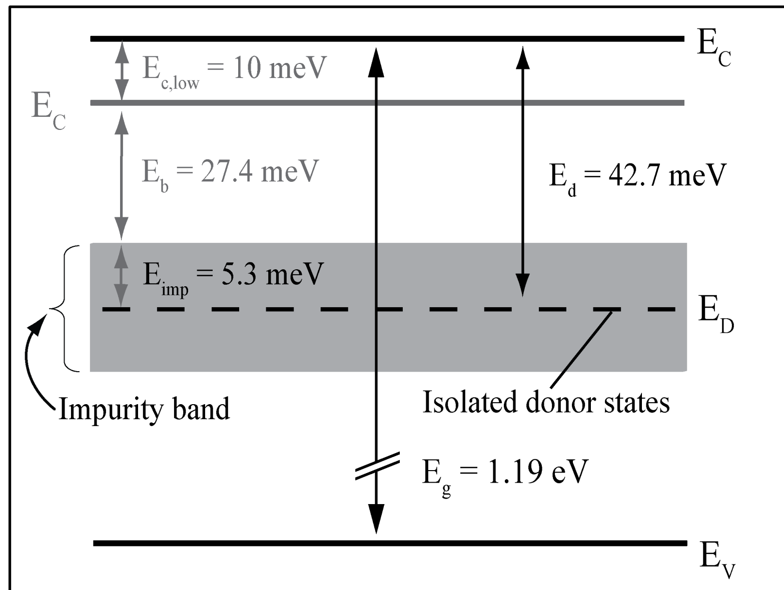

Figure 5.5: Simplified energy band structure of low (black) and heavily (grey) doped silicon at cryogenic temperatures. It illustrates the reduced binding energy E_b in heavily antimony doped silicon. The decrease of the lower conduction band edge E_C by 10 meV and the shift of the donor level E_D to the upper edge of the impurity band by 5.3 meV leads to a reduction of the binding energy from 42.7 meV to 27.4 meV. The valence band edge remains unchanged for low and heavily doped silicon.

Consequently, the binding energy of heavily doped material can be derived theoretically as follows:

$$E_b^t = E_d - E_{imp} - E_{c,low} = 42.7 \text{ meV} - 5.3 \text{ meV} - 10 \text{ meV} = 27.4 \text{ meV} \quad (5.2)$$

where E_b^t is the theoretical derived binding energy. It coincides very well with the experimentally obtained value of $E_b = (27 \pm 1.1)$ meV. From E_b the cutoff-wavelength can also be determined:

$$\lambda_c = \frac{hc}{E_b} = 40 \text{ } \mu\text{m} \quad (5.3)$$

This also corresponds to the spectral measurements from [37]. This group used Si:Sb BIB structures to measure the quantum efficiency in the mid-infrared regime. They observe that the detectors are sensitive from 10 μm to 40 μm.

2. **$T < 12$ K:**

   At low temperatures, the current of the BIB structure (red curve in figure 5.4) decreases with the same slope and is constant at temperatures lower than 8 K. The dark current of the heavily doped material (black curve in figure 5.4) is only slightly increasing with temperature. The flat slope of the dark current of the test structure without blocking layer is interpreted as hopping conduction. The current of hopping conduction I_{hop} is temperature dependent and was calculated by Mott et al. [13]:

$$I_{hop} = I_{dark} \propto exp(\frac{-E_a}{k_B T}) \quad (5.4)$$

   The activation energy is determined to 5.7 meV, which corresponds to the calculated activation energy of 5.7 meV at a donor concentration of $3 \cdot 10^{17} \frac{1}{\text{cm}^3}$ [38]. The electrons are not emitted into the conduction band. Instead, they hop from one donor state to the neighbouring one. As the blocking layer is not present, the electron transport is dominated by hopping conduction. In contrast, the slope of the red curve in figure 5.4 is constant and corresponds to the binding energy of $E_b = 27$ meV. It shows, that the current of the BIB structure is dominated from purely thermally excited electrons and no hopping conduction exists. This represents the blocking mechanism of the BIB structure. Instead, when the shielding for the

BIB structure is not mounted, the current-voltage characteristics is similar to the heavily doped material. In this case, background radiation, originating from the inner shield ($T = 20$ K), hits the detector. This results into an inefficient blocking mechanism [39].
The constant current level of a few picoampere at temperatures lower than 8 K can be explained by the sensitivity limits of the source meter. The source meter Keithley 2620 was used, which is limited in the picoampere range.

5.3.2 Intrinsic electric fields

The dark current was examined at different bias voltages up to 2 V, which is shown in figure 5.6. It can be seen that the slope of the Arrhenius plot decreases at higher bias voltages. Therefore, it is concluded that the binding energy of the shallow donors in the active layer decreases with higher bias voltages. This can be achieved when the donors are exposed to a sufficiently high electric field. As described in section 3.2, Poole and Frenkel stated a barrier lowering, which occurs at hydrogen-like quantum states in presence of an electric field.

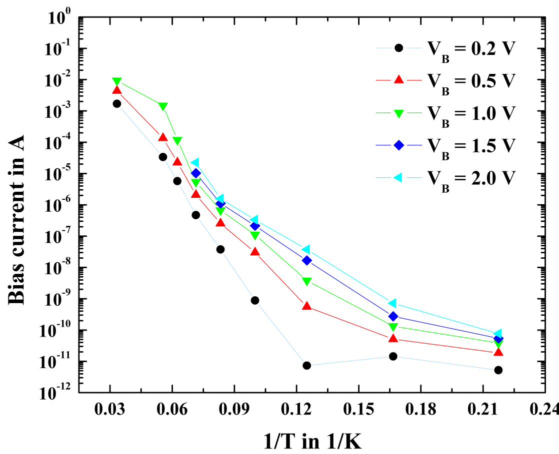

Figure 5.6: Measured dark current in dependence of $\frac{1}{T}$ (Arrhenius-plot) of the BIB structure device with blocking layer at different bias voltages.

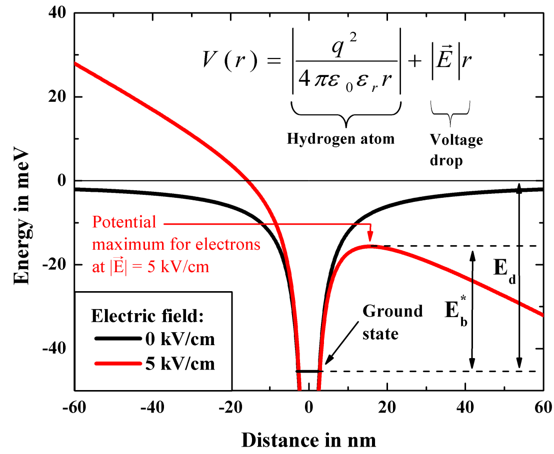

Figure 5.7: Potential of the shallow donor state, which is exposed to an electric field of $0\ \frac{\text{kV}}{\text{cm}}$ $(5\ \frac{\text{kV}}{\text{cm}})$. The barrier of the shallow donor state is lowered, when an electric field of $5\ \frac{\text{kV}}{\text{cm}}$ is applied. The potential is a linear combination of the potential of the hydrogen atom and the voltage drop.

One example is shown in figure 5.7, where the potential of a shallow Phosphorous state is shown at an electric field of 0 $\frac{\text{kV}}{\text{cm}}$ and 5 $\frac{\text{kV}}{\text{cm}}$. In addition to the potential of the hydrogen atom the linear voltage drop plays the decisive role. The term $|\overrightarrow{E}|r$ is responsible for the potential bending and for the forming of a potential maximum. This potential maximum defines the height of the binding energy E_b^*. The barrier lowering is linked with the electric field $|\overrightarrow{E}|$ as follows [21]:

$$\Delta E = e\sqrt{\frac{e|\overrightarrow{E}|}{\pi\epsilon_0\epsilon_r}} \tag{5.5}$$

where ΔE is the barrier lowering of the shallow donor and e is the elementary charge. From the Arrhenius plot in figure 5.6 the binding energy and the resulting electric field at different bias voltages are determined. The binding energy and the respective electric field in dependence of the bias voltage $|\overrightarrow{E}_{exp}|$ are shown in figure 5.8.

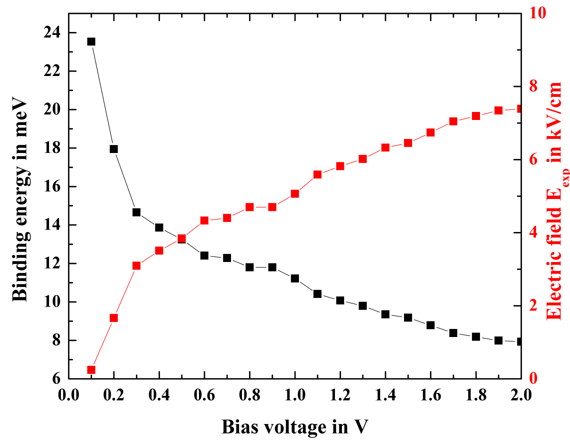

Figure 5.8: Experimentally derived binding energy (black curve) against the bias voltage from the slope of the Arrhenius-plot in figure 5.6. These values represent the shallow donors at the interface active/blocking layer, which are exposed to an electric field of E_{exp}. The respective electric fields (red curve) at the interface active/blocking layer are calculated with equation 5.5.

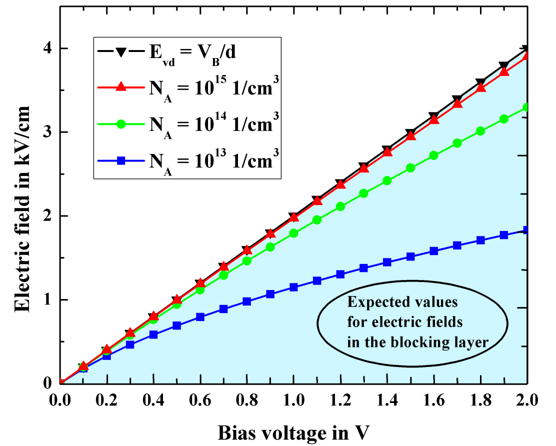

Figure 5.9: Calculated electric field in the blocking layer for different impurity concentrations in the active layer. The higher the concentrations the more the values of the electric field match with the electric fields resulting from the linear voltage drop E_{vd}. E_{vd} is the upper limit for the electric field in the blocking layer. The shaded area highlights the expected values for the electric fields at a given acceptor concentration.

These experimentally obtained values relate to the shallow donors at the interface active/blocking layer. At this position the electric field is highest. From the BIB structure theory the electric field at the interface equals the electric field in the blocking layer in the absence of fixed charges at the interface. Therefore, the electric fields in the blocking layer was calculated for different impurity concentrations in the active layer as shown in figure 5.9. The increased electric field at high concentrations can be explained by the voltage drop in the space charge region in the active layer and the blocking layer.
A schematic of a BIB structure under applied bias voltage is shown in figure 5.10. The space charge region in the active layer and the blocking layer have insulating behaviour. That is why one part of the voltage V_1 drops at the space charge region in the active layer and the other part V_2 drops at the blocking layer. The sum of V_1 and V_2 is the bias voltage. At high concentrations the depletion width is lower (equation 2.7), which results in a lower voltage drop in the space charge region of the active layer. As a consequence the voltage drop and the resulting electric field at the blocking layer V_2 increase with higher impurity concentration. Additionally, the electric field $E_{vd} = \frac{V_B}{d}$ is plotted in figure 5.9. It is the electric field, when the whole bias voltage drops in the blocking layer. d is the thickness of the blocking layer and has a value of 5 μm.

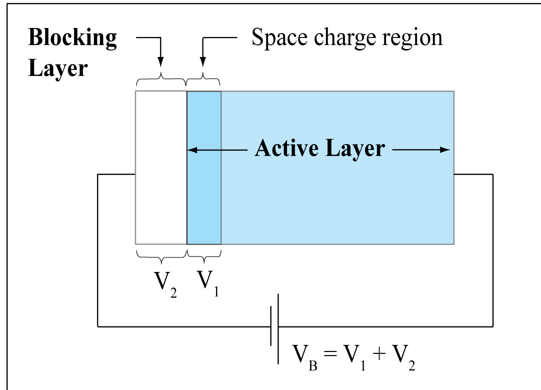

Figure 5.10: Simplified schematic of a BIB structure under applied bias voltage V_B. One part of the voltage V_1 drops at the space charge region and the other part $V_2 = V_B - V_1$ drops at the blocking layer V_2. The value of V_1 depends on the width of the space charge.

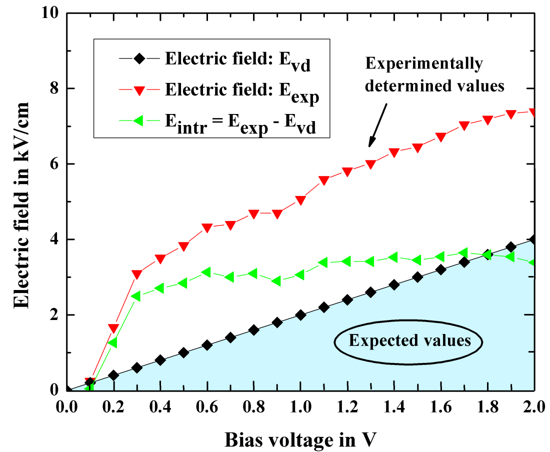

Figure 5.11: Electric field in dependence of the bias voltage. The experimentally determined electric field E_{exp} from the slope of the Arrhenius plot in figure 5.6, the theoretical expected electric field E_{vd} from figure 5.9 and the intrinsic electric field E_{intr} are plotted. The intrinsic electric field arises from the difference of E_{exp} and E_{vd}.

Independent from the applied bias voltage, in this case, the space charge region is very thin or does not exist. As the information of the acceptor concentration of the active layer is not available E_{vd} is taken as the upper limit for the electric field in the blocking layer.
The experimentally determined electric fields E_{exp} from figure 5.8 are compared with the expected fields, which result from the voltage drop E_{vd} over the blocking layer as shown in figure 5.11. The experimental values for the electric fields (red curve in figure 5.11) are higher than the expected values originating from the linear voltage drop E_{vd} at the blocking layer (black curve in figure 5.11). Consequently, additional intrinsic electric fields exist. The experimentally determined electric fields E_{exp} is composed of the expected fields E_{vd} and the intrinsic fields E_{intr}. As the Maxwell equations are linear, the following relation is obtained:

$$|\overrightarrow{E}_{exp}| = |\overrightarrow{E}_{vd}| + |\overrightarrow{E}_{intr}| \tag{5.6}$$

where $|\overrightarrow{E}_{intr}|$ is the intrinsic electric field. Equation 5.6 can also be written as:

$$|\overrightarrow{E}_{intr}| = |\overrightarrow{E}_{exp}| - |\overrightarrow{E}_{vd}| \tag{5.7}$$

$|\overrightarrow{E}_{intr}|$ is plotted in figure 5.11 (green curve). The intrinsic electric fields have a constant value of 3 $\frac{\mathrm{kV}}{\mathrm{cm}}$ at bias voltages higher than 0.2 V. The excess electric fields is interpreted with the space charge resulting from the interface transition between the active and blocking layer. A simplified energy band diagram, which illustrates the heavily doped region at the interface, is shown in figure 5.12. During the growth of the epitaxial silicon the donors of the active layer diffuse into the highly resistive blocking layer. The diffused donors build up a thin region at the interface, where silicon is heavily doped. However, the heavy doping is not sufficient to have hopping conduction. The concentration is in the range from 10^{14} $\frac{1}{\mathrm{cm}^3}$ to 10^{16} $\frac{1}{\mathrm{cm}^3}$ and the thickness is several 100 nm. Therefore, the ionized donors in this region cannot be neutralized by the hopping conduction process. The positive space charge of these donors is responsible for the intrinsic field. The electric field in the blocking layer is estimated by using the Maxwell equation in one dimension:

$$|\overrightarrow{E}_{bl}|(z_i) = \frac{1}{4\pi\epsilon_0\epsilon_r}\int_{z=0}^{z=z_i} \rho_{bl}(z)dz \tag{5.8}$$

The integral covers the range from the surface of the device ($z = 0$) to any position at the blocking layer ($z = z_i$). The maximum value of the upper integration limit z_i is the interface active layer/blocking layer x_{int}. x_{int} is denoted in figure 5.12. The interface x_{int}

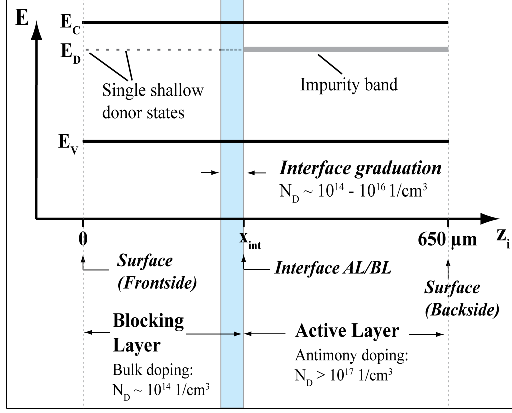

Figure 5.12: Schematic of the distribution of the donors at the interface active and blocking layer (AL/BL). The heavily doped interface is responsible for the excess intrinsic electric fields.

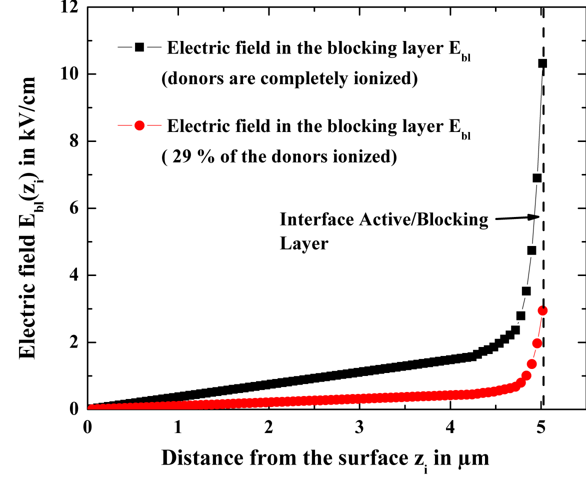

Figure 5.13: Electric field distribution in the blocking layer, when the donors are completely ionized (black curve) and when 29 % of the donors are ionized (red curve).

is the position, where hopping conduction begins and is about 5 μm at a concentration of 10^{17} $\frac{1}{\text{cm}^3}$. $\rho_{bl}(z)$ is the space charge in the blocking layer, which is composed of the doping concentration of the interface transition $\rho_{ig}(z)$ and the bulk concentration ρ_{bg} in the blocking layer:

$$\rho_{bl}(z) = \rho_{ig}(z) + \rho_{bg} \tag{5.9}$$

The bulk concentration is constant and is given by the doping during the epitaxial process. In our case it is $\rho_{bg} = 3 \cdot 10^{14}$ $\frac{1}{\text{cm}^3}$. The doping concentration of the interface transition can be determined by SIMS measurements as shown in figure 5.1 in section 5.1. The space charge region of the active layer, where hopping conduction occurs, is negatively charged. The donors are neutralized by the hopping conduction process and the acceptors are ionized and build the negative space charge region.
In contrast, the region in the blocking layer is positively charged, because the ionized donors cannot be neutralized by the hopping conduction process. The calculated electric field $|\overrightarrow{E}_{bl}|$ is shown in figure 5.13. The electric field in the blocking layer is not constant as one would expect from the BIB structure theory [2];. It can be explained by the ionized donor states in the blocking layer ($\rho_{ig}(z)$ and ρ_{bg}), which contribute to the electric fields.

[2] It is assumed, that charged donors/acceptors do not exist as described in section 2.1.

Ionization occurs by infrared background radiation or thermal excitation. If all donors are ionized, the peak electric field at the interface is at 10.5 $\frac{\text{kV}}{\text{cm}}$. This value exceeds the experimentally determined value of 3 $\frac{\text{kV}}{\text{cm}}$. This can be explained by the presence of frozen electrons in the donor states. The ratio I between ionized and neutral donors ρ_{io} and ρ can be estimated:

$$\mathrm{I} = \frac{\rho_{io}}{\rho} = \frac{E_{intr}}{E_{bl}} = \frac{3\ \frac{\text{kV}}{\text{cm}}}{10.5\ \frac{\text{kV}}{\text{cm}}} = 0.29 \tag{5.10}$$

It means, that 29% of the donors are ionized. 71% of the donors are neutral and do not contribute to the space charge. As a result it is desirable to have an abrupt interface. This can be achieved by using the MBE[3] technology to grow the blocking layer. As the MBE process temperature is in the range of 600 °C diffusion of the impurities is heavily suppressed.

5.3.3 Influence of the p$^+$-contact

The voltage at the p$^+$-contact was varied and the dark current of the BIB structure was measured. As can be seen from figure 5.14 the potential of the p$^+$-contact does not affect the current characteristics. This behaviour can be understood as follows:
The n$^+$-contacts and the embedded shallow p$^+$-implantation function as a pin-diode. The depletion width d_p in the active layer can be estimated by [40]:

$$d_p = \sqrt{\frac{2\epsilon_r\epsilon_0 \cdot V_{p+}}{N_D}} \tag{5.11}$$

where V_{p^+} is the voltage at the p$^+$-contact and $N_D = 2 \cdot 10^{17} \frac{1}{\text{cm}^3}$ the antimony concentration in the active layer. This equation is valid, when the p$^+$-contact is embedded on top of the heavily doped active layer. However, the p$^+$-implantation is on top of the blocking layer. Thus, the depletion width is lower than the calculated width of m from equation 5.11. As a result the solution of equation 5.11 is an upper limit for the depletion width. For $V_{p^+} = -20$ V one obtains $d_p = 354$ nm, which is even shorter than the interface transition between the active layer and the blocking layer. From figure 5.1 the width of the interface transition is determined to 1 μm. The depletion zone caused by the p$^+$-contact does not penetrate the active layer.
As discussed in subsection 5.3.1 the current of the BIB structure test structures results

[3] Molecular Beam Epitaxy

from thermally excited electrons in the active layer. Consequently, as the depletion zone does not penetrate the active layer, the p^+-contact has a very low steering impact on the current in the active layer. The right plot of figure 5.14 shows a slight increase of the bias current of about 1 % with decreasing V_{p+}. The p^+-contact surrounds the bias contact and influence the interface potential between the active layer and the blocking layer only at the border of the bias. In this regime the effective bias voltage is reduced with decreasing V_{p+} resulting in a reduced bias current.
This feature is important for the combination DEPFET - BIB, because the DEPFET is directly integrated on the blocking layer. The source and drain contacts of the p-channel MOSFET are shallow p^+-implantations, which are embedded on top of the blocking layer. The p^+-contacts of the BIB structure test structures simulate the behaviour of a source or drain contact. Typical values for transistor operations are: $V_{source} = 0$ V and $V_{drain} = -5$ V. From the presented experiment with the BIB structure test structures, it was found out that the current does not depend on the voltage of the p^+-contact. Therefore, no dependencies on the photocurrent in the active layer caused by the potentials of the source or the drain at the DEPFET - BIB is expected.

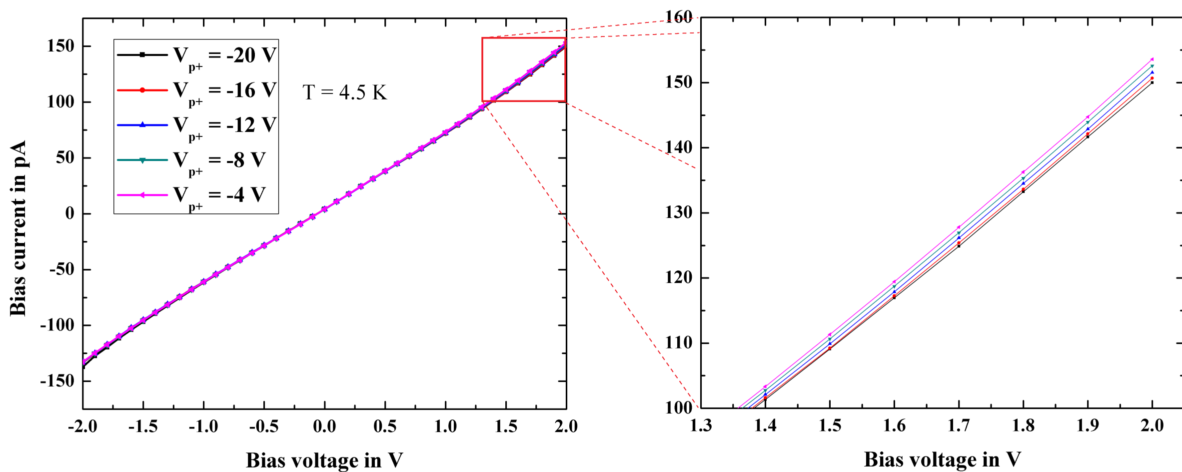

Figure 5.14: Measured dark current of the BIB structure test structure for different voltages at the p^+-contact.

Chapter 6

The reset mechanism of the DEPFET at cryogenic temperatures

This chapter deals with the reset of electrons in the internal gate of linearly structured DEPFETs at cryogenic temperatures. Experiments on the DEPFETs were performed to examine the clear performance in detail. Additionally, a physical model was developed to explain the behaviour of the electrons during the clear process. The theoretical results from the model are discussed and compared with the experimental results.

6.1 The reset problem at cryogenic temperatures

6.1.1 Freeze-out of free charge carriers

As described before a voltage pulse at the clear contact does not entirely remove the signal electrons from the internal gate. The reason for incomplete charge clear at cryogenic temperatures can be explained by the freeze-out of the signal electrons in the donor states of the internal gate. The internal gate is the global potential minimum of one pixel with a peak concentration of phosphorous in the range of $10^{16}\ \frac{1}{\mathrm{cm}^3}$. The positively ionized donor states are shallow phosphorous states with a binding energy of 45.7 meV. They can be seen as microscopic potential minima at the lattice location of the phosphorous donors, where the signal electrons get trapped at low temperatures. At room temperature the thermal energy of electrons of 25 meV is high enough, so that the electrons are emitted into the conduction band. In contrast, the thermal energy at 6 K is $k_B T = 0.49$ meV and it is not possible to emit the electrons from the shallow phosphorous states into the conduction band. For the understanding of the proposed model for the reset it is necessary to understand the freeze-out at equilibrium and non-equilibrium conditions.

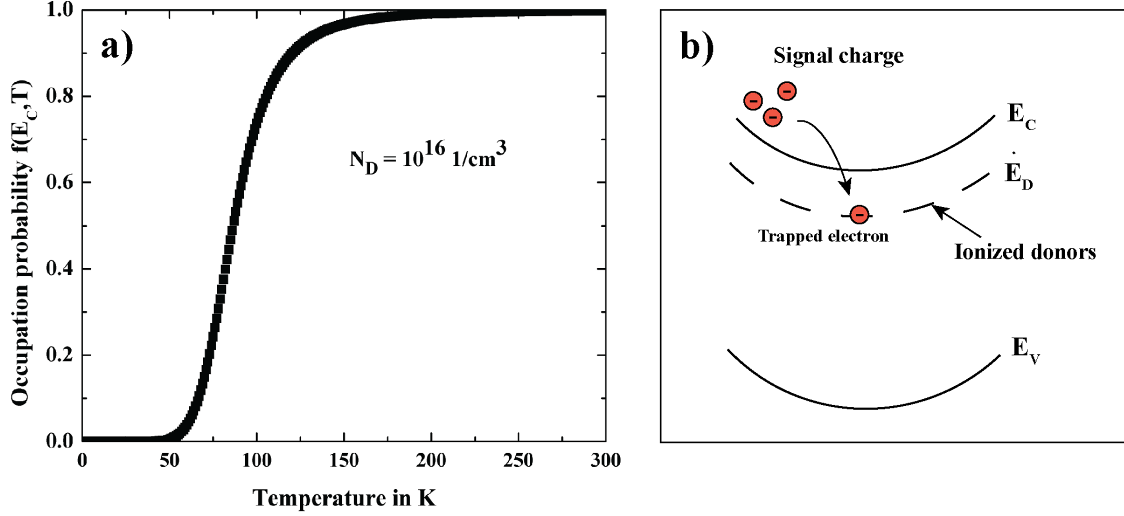

Figure 6.1: a) Calculated Fermi distribution of electrons in n-doped Silicon with a binding energy of 45.7 meV at the conduction band edge E_C. The freeze-out effects occur at temperatures lower than 50 K. b) Schematic of the macroscopic potential minimum of the internal gate. The ionized donors are microscopic potential minima in the internal gate. Trapping of the signal charges into the ionized shallow donors is indicated.

Freeze-out at equilibrium conditions

The occupation probability in the conduction band at thermal equilibrium in dependence of the temperature is described by the Fermi statistics. In thermal equilibrium it is written as [11]:

$$f(E,T) = 1 - \frac{1}{1 + \exp(E - E_F/k_B T)} \tag{6.1}$$

where E_F is the Fermi energy. For an extrinsic semiconductor the Fermi energy is calculated by [41]:

$$E_F = \frac{E_C + E_D}{2} + \frac{1}{2} k_B T \cdot \ln(\frac{N_D}{N_C}) \tag{6.2}$$

with N_C being the effective density of states in the conduction band, N_D the doping concentration, E_C the energy level of the lower conduction band edge and E_D the energy

level of the shallow donor state. Therefore, the occupation probability of the electrons in an n-doped semiconductor is described by the temperature, the binding energy and the doping concentration.
The calculated Fermi statistic at the conduction band edge $f(E_C, T)$ is plotted in figure 6.1 a) at a doping concentration of $N_D = 10^{16} \, \frac{1}{\text{cm}^3}$ and a binding energy of $E_d = E_C - E_D = 45.7$ meV. The edge of the Fermi distribution indicates the temperature, where freeze-out in a doped semiconductor occurs. At temperatures lower than 50 K the probability of the electrons to occupy the conduction band is close to zero. The electrons do not have a sufficiently high thermal energy to emit them from the shallow donors into the conduction band. The Fermi statistic is only valid at thermal equilibrium.

Freeze-out at non-equilibrium conditions

In case of non-equilibrium, i.e. in presence of electric fields, the following additional conditions have to be fulfilled for the freeze-out of the electrons into shallow donors at low temperatures:

1. Free electrons have to exist in the conduction band.
2. The donor states are ionized and function as trapping states for the free electrons.
3. The drift time of the electrons is higher than the recombination time into the shallow donor states. The interaction time between the shallow donor and the electron decreases with increasing drift velocity. The electron is trapped if the dwell time of the electron at a shallow donor state is sufficiently high.

These conditions are fulfilled in the internal gate of the DEPFET. By incoming radiation free electrons in the bulk are generated and drift to the internal gate. As the electrons arrive they are trapped into the ionized donor states (figure 6.1 b)). During the collection time (figure 4.11) the dwell time of the electrons in the internal gate exceeds the recombination time. The recombination time of electrons into shallow donors is calculated in section 6.2.2 and is 10 ps at 6 K[1]. Typical collection times are in the microsecond range. The dwell time of the electrons is the time from the arrival of the electrons into the internal gate until the beginning of the clear time. During the clear time the transport of the collected electrons in the internal gate to the clear contact is strongly suppressed by the freeze-out process.

[1] The result is anticipated from section 6.2.2.

6.1.2 A new method for the reset

The aim is to clear the internal gate completely by one clear pulse. Therefore, it is necessary to emit the trapped electrons in appropriate time intervals of nano- to microseconds. As illustrated in subsection 4.3.2, the emission time exceeds the clear time several milliseconds. The emission time is a strong function of the binding energy E_d and the temperature. $E_d = E_C - E_D$ is the barrier which must be overcome by the trapped electron. Lowering the binding energy and/or increasing the temperature leads to an increase of the emission of the trapped electrons into the conduction band. As the operating mode of the DEPFET is at cryogenic temperatures the lowering of E_d is the only option to enhance the emission. This can be achieved by applying high electric fields at these localized states to emit them into the conduction band. In this case, when an electric field $\left|\vec{E}\right|$ is applied, the potential barrier E_d is lowered by E_{PF} [21]:

$$E_{PF} = e\sqrt{e\left|\vec{E}\right|/\epsilon} \tag{6.3}$$

As a result an electron with an energy between $(E_C - E_{PF})$ and (E_C) is considered to be in the conduction band. This is called the Poole-Frenkel effect as already described in section 5.3.2.

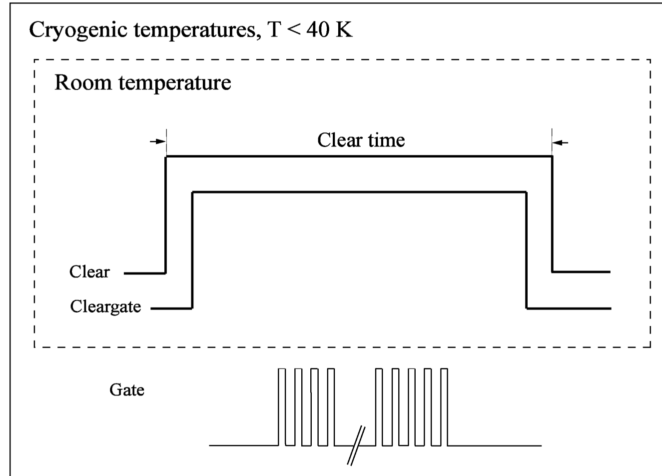

Figure 6.2: The pulse schemes of the clear and clear gate for room temperature and cryogenic applications are shown. At room temperature only the clear and clear gate contacts are pulsed to remove the electrons from the internal gate. Under cryogenic conditions gate pulses are used to exploit the electric field enhanced emission and improve the clear behaviour.

The ratio between the barrier height and the thermal energy as a function of the electric field is given by:

$$s(\left|\vec{E}\right|) = \frac{E_b}{k_B T}(\left|\vec{E}\right|) = \frac{E_d - E_{PF}(\left|\vec{E}\right|)}{k_B T} = \frac{E_d - q\sqrt{q\left|\vec{E}\right|/\epsilon}}{k_B T} \tag{6.4}$$

with $E_b = E_d - E_{PF}(\left|\vec{E}\right|)$ being the effective barrier height. $\left|\vec{E}\right|$ is the absolute value of the electric field, q is the unit charge and ϵ is the permittivity of Silicon.
The electric field is generated by pulsing an additional contact (figure 6.2). During the clear time, the gate contact is pulsed to generate a sufficiently high electric field at the position of the collected charge in order to release them from the shallow donor states into the conduction band. Figure 6.3 shows a schematic of the shift of the potential minimum and the electron movement in the collection state and the pulsed state. The additional pulsing results in a shift of the potential minimum. One fraction of the emitted electrons drifts to the new potential minimum and is retrapped. The other fraction reaches the clear contact. When pulsed back into the collection state, the same happens with the trapped electrons in the new potential minimum.

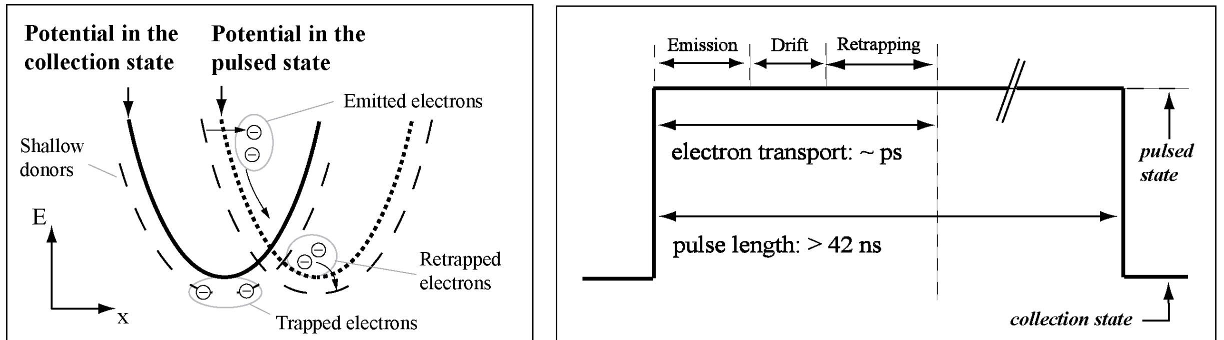

Figure 6.3: *Left:* Schematic of the potential minimum shift of the internal gate. This can be achieved by pulsing the gate. The electrons are emitted and drift to the new potential, where they are recaptured. Some of them drift to the clear contacts. *Right:* Scheme of one gate pulse. The movement of the electrons in the internal gate is indicated, which occurs after the gate pulse is applied.

6.2 Model

The idea in the previous section, using the Poole-Frenkel effect to emit the electrons from the trapped state, is the corner stone for successful reset. However, recombination processes occur, which inhibit that all electrons are removed from the internal gate. In order to understand the clear process at cryogenic conditions the interdependency of the emission and recombination processes has to be simulated.
In this section a model is presented, which describes the reset of the DEPFET under cryogenic conditions. Room temperature device physics is modelled with the Two-dimensional SemiConductor Analysis package (TESCA) [42]. It is based on the Poisson equations and continuity equations for electrons and holes, which are solved by a finite element method. As the DEPFET is a room-temperature device and can be modelled with TESCA, low temperature simulations are not foreseen. Freeze-out effects are not included. Since TESCA does not include important low temperature effects, a program was written, which takes into account the following physical mechanisms:

- **Electric field enhanced emission from shallow donor states into the conduction band (subsection 6.2.1)**
- **Electric field dependent recombination into the shallow donor states (subsection 6.2.2)**
- **Diffusion and drift of electrons in the internal gate (subsection 6.2.4)**

The behaviour of the trapped and free collected electrons in the internal gate during the clear time is modelled. Dynamic simulations were performed and the continuity equation for the electrons in the internal gate (section 6.3) was solved.
The following subsections describe the input parameters, which are needed for the simulation program. The parameters, like emission and recombination rates, were derived from the existing models and calculated as a function of the electric field in subsection 6.2.1 and 6.2.2 respectively. TESCA was used to calculate the potential and electric field distribution of the internal gate (subsection 6.2.3). The mobility and diffusion constants, taken from the literature, determine the diffusion and drift of the electrons in the conduction band as described in subsection 6.2.4.

6.2.1 Electric field enhanced emission

The main aspect of the model is the electric field enhanced emission of trapped charge carriers from the shallow donor states into the conduction band at cryogenic temperatures. Here, the electric field and temperature dependent emission rates are discussed.

The thermal emission rate ϵ_{th} from an impurity state into the conduction band is given by [40]:

$$\epsilon_{th} = \sigma \cdot v_{th} \cdot N_C \cdot \exp(-E_d/k_b T) \tag{6.5}$$

with $N_C = 2(\frac{2\pi m_e k_B T}{h^2})^{3/2}$ being the effective density of states in the conduction band, v_{th} the thermal velocity and σ the capture cross section. The emission rate changes in presence of an electric field by modifying the barrier height as shown in figure 6.4 a). The potential of a shallow donor can be modeled similarly to a hydrogen atom, corrected by the permittivity of silicon ϵ_r. It can be described by the function:

$$V(r) = -\frac{q^2}{4\pi\epsilon_0\epsilon_r r} - \left|\vec{E}\right| r \tag{6.6}$$

The binding energy of a shallow phosphorous atom is 45.7 meV. In presence of an electric field the binding energy is reduced by E_{PF} and thus, the thermal emission is enhanced. At an electric field of 5 $\frac{\text{kV}}{\text{cm}}$ the binding energy is lowered by 20 meV as can be seen in figure 6.4. The modified emission rate is formulated by:

$$\epsilon_{PF} = \epsilon_{th} \cdot \exp(E_{PF}/k_b T) \tag{6.7}$$

ϵ_{PF} is the thermally assisted emission rate. Furthermore, the electric field leads to a decrease of the barrier width between the localized state and the conduction band. This enables tunneling of the electrons into the conduction band. The tunneling emission rate ϵ_{TU} is given by [43]:

$$\epsilon_{TU} = \frac{U}{6\hbar} \cdot (\frac{U}{E_D})^2 \cdot \exp\left\{\frac{E_D}{U}^{3/2}\left[1 - (\frac{E_{PF}}{E_b})^{5/3}\right]\right\} \tag{6.8}$$

where $U = (\frac{3q\hbar\left|\vec{E}\right|}{4\sqrt{2m^*}})^{2/3}$ and $\hbar$ is Planck's constant. ϵ_{TU} is the emission rate, which results from pure tunneling. Instead of performing an isoenergetic transition from the impurity state to the conduction band, the electron in the impurity level can be excited by lattice phonons to an energy E closer to the conduction band, followed by tunneling through the hyperbolic barrier.

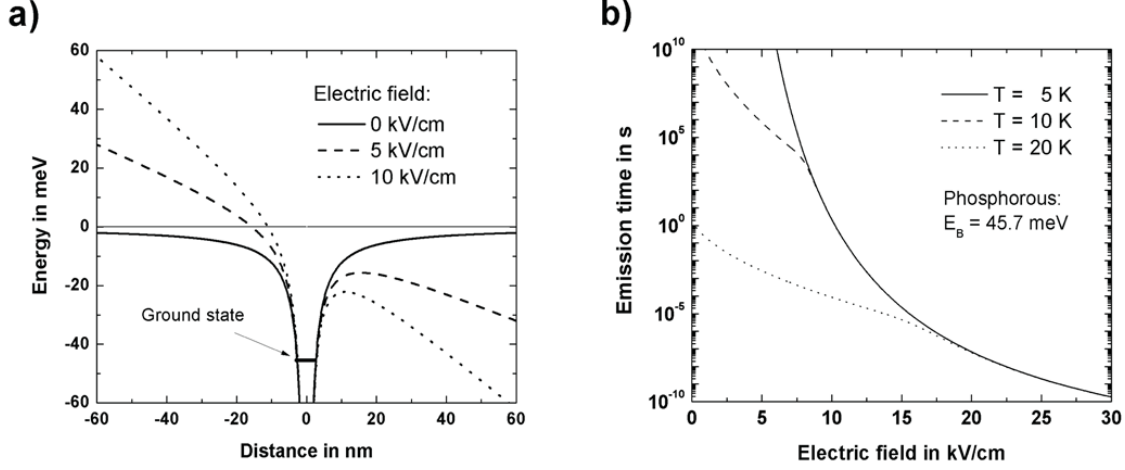

Figure 6.4: a) The potential of a single shallow donor state at different electric fields. At sufficiently high electric fields the barrier height and width of the potential are lowered. This leads to electric field enhanced emission. b) Calculated emission time against the electric field for different temperatures from equation 6.13.

The frequency of an excitation is given by [43]:

$$\nu = \sigma \cdot v_{th} \cdot N_C \cdot \exp(-\frac{E_D - E}{k_b T}) \tag{6.9}$$

and the contribution of this transition to the phonon-assisted emission rate is therefore [43]:

$$\nu = \sigma \cdot v_{th} \cdot N_C \cdot \exp(-\frac{E_D - E}{k_b T}) \cdot \exp\left\{-(\frac{E}{U})^{3/2}(1 - (\frac{E_D}{E})^{5/3})\right\} \tag{6.10}$$

where the second exponential term is the electron transparency of the hyperbolic barrier. The calculation of the one-dimensional emission rate requires an integration over energy from $E = E_{PF}$ to $E = E_D$ which yields [43]:

$$\epsilon_{PAT} = \frac{e_n}{2} \int_{\Delta E_{PF}}^{E} (\frac{U}{E})^{3/2} \exp\left\{\frac{E}{k_b T} - (\frac{E}{U})^{3/2}[1 - (\frac{\Delta E_{PF}}{E})^{5/3}]\right\} \frac{dE}{k_b T} \tag{6.11}$$

ϵ_{PAT} is the emission rate, originating from phonon assisted tunneling.

Summing up, the entire emission rate is composed of thermal, phonon assisted tunneling and pure tunneling emission:

$$\epsilon_G = \epsilon_{PF} + \epsilon_{TU} + \epsilon_{PAT} \tag{6.12}$$

The total emission time

$$\tau = \frac{1}{\epsilon_G} \tag{6.13}$$

is plotted against the electric field in figure 6.4 b).
At lower electric fields the emission is dominated by thermal excitation from the ground state into the conduction band. ϵ_G varies strongly with temperature at $0 < \left|\vec{E}\right| < 10\ \frac{\mathrm{kV}}{\mathrm{cm}}$. The values for the emission time are in the range of milliseconds to several weeks in the temperature regime from 10 K to 20 K. At higher fields ($\left|\vec{E}\right| > 17\ \frac{\mathrm{kV}}{\mathrm{cm}}$) the barrier width is in the range of nanometers. The electron wave function of the ground state overlaps with the conduction band. This results in tunneling into the conduction band, which is independent from temperature. At electric fields higher than $\left|\vec{E}\right| > 17\ \frac{\mathrm{kV}}{\mathrm{cm}}$ the emission time is in the range of microseconds. For the DEPFET it is necessary to achieve such electric fields at the position of the trapped charge.

6.2.2 Electric field dependent recombination

The Poole-Frenkel effect also plays a role in the calculation of the recombination into shallow donors. Therefore a fundamental understanding of the capture mechanism in respect to the electric field is required [44]. The figures 6.5 and 6.6 illustrate the potential of a shallow phosphorous donor when $\left|\vec{E}\right| = 0$ and $\left|\vec{E}\right| = 5\ \frac{\mathrm{kV}}{\mathrm{cm}}$ respectively. In a first approximation, the carrier is considered to be trapped by a shallow hydrogenic centre when it arrives in an excited state corresponding to an ionization energy of about k_BT; the energy of the excited state is located by a value of k_BT below the potential maximum (distance of the horizontal dashed lines in the figures 6.5 and 6.6). For smaller binding energies, the probability for re-emission is high (small sticking probability), while for larger binding energies the carrier will descend the ladder of excited states down to the ground state by multiple emission of phonons. This results in a critical radius r_c for thermal capture as shown in figure 6.5, corresponding to a binding energy of k_BT in the Coulomb potential of the ionized donor state.
When the donor state is exposed to an electric field a potential maximum is formed, which is the level of the reduced barrier E_{PF}. The excited states of the modified shallow donor

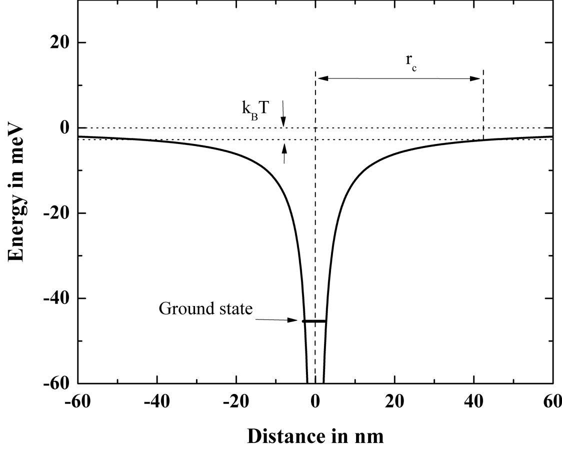

Figure 6.5: Potential of a single shallow donor state when $E = 0\ \frac{\mathrm{kV}}{\mathrm{cm}}$. Thermal capture is determined by the critical radius r_c.

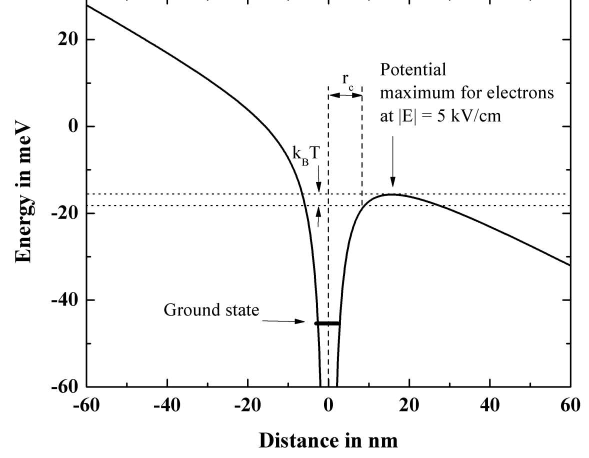

Figure 6.6: Potential of a single shallow donor state when $E = 5\ \frac{\mathrm{kV}}{\mathrm{cm}}$. r_c is reduced due to the reduction of the barrier.

can exist below this maximum. As the physical volume of the excited states is reduced the radius of thermal capture decreases simultaneously. The physical volume of these excited states is lower than the distance between the ground state and the potential maximum d_{max}. Figure 6.6 shows the potential of a single donor in an electric field of 5 $\frac{\mathrm{kV}}{\mathrm{cm}}$. In this case d_{max} is about 15 nm. The critical radius r_c for thermal capture is reduced and can be approximated by [45]:

$$r_c = \left(\frac{4\pi\epsilon k_B T}{q^2} + \sqrt{\frac{4\pi\epsilon \left|\vec{E}\right|}{q}}\right)^{-1} \tag{6.14}$$

Therefore, within the sphere of the critical radius, the electrons are captured with a high probability. Instead of being captured, the electrons can be scattered without being recombined into the excited states of the shallow donor. In order to calculate the capture cross-section it is necessary to include the mean free path λ. λ is the path, before the electrons suffer from inelastic scattering. If λ is the mean free path for an energy losing condition and $\frac{4}{3}r_c$ is the average distance across the sphere, $\frac{4r_c}{3\lambda}$ is the probability of a suitable collision if one hits the sphere [2]. πr_c^2 is the cross section for hitting the sphere. Thus, the capture cross section σ is assumed to be homogeneous in all directions and can

[2] The volume of a sphere divided by the surface of a circle: $4\pi/3r^3 : \pi r^2 = 4/3r$

be expressed as [44]:

$$\sigma = \frac{4\pi r_c^3}{3\lambda} \tag{6.15}$$

Assuming a proportionality between a favourable (capturing) collision and a normal scattering collision (determining the carrier mobility), λ can be expressed as λ_0/β. With the normal scattering collision, it is meant the scattering of the electron in the conduction band. Here, λ_0, is approximated by [45]:

$$\lambda_0 = \mu\sqrt{E_0 m^*}/q \tag{6.16}$$

with E_0 being the average carrier energy, while β is a semi-empirical factor, corresponding to the probability of an effective trapping event. All unknowns are combined in this factor, which is determined empirically from the zero-field cross section. The carrier energy is given by [45]:

$$E_0 = 1/2m^* v_d^2 + 3/2k_B T_e \tag{6.17}$$

where T_e is the effective carrier temperature, which can be developed as a function of the lattice temperature and of the average drift energy [46]:

$$k_B T_e = k_B T + \alpha m^* v_d^2 \tag{6.18}$$

with α a semi-empirical parameter, which depends on the carrier energy. This parameter can be considered as a kind of shape factor of the hot carrier distribution.

Figure 6.7 shows the calculated capture cross-section and the capture time in dependence of the electric field. When the electric field is increased from $\left|\vec{E}\right| = 0\ \frac{\text{kV}}{\text{cm}}$ to $\left|\vec{E}\right| = 10\ \frac{\text{kV}}{\text{cm}}$ the recombination decreases by three orders of magnitude. At $\left|\vec{E}\right| = 0$ the capture cross-section is determined by $\sigma_0 = 1.1 \cdot 10^{11}\ \text{cm}^2$. For the β-coefficient the value of $2 \cdot 10^{-3}$ is used and for the α-coefficient the value is 1 [45]. Norton and et al. investigated the recombination of electrons at ionized donors in Silicon at low temperatures and obtained $\sigma = 1.0 \cdot 10^{11}\ \text{cm}^2$ at $T = 10$ K and $\left|\vec{E}\right| = 0$ [47]. The capture time in the zero-field region is calculated as [47]:

$$\tau_r = \frac{1}{\sigma_0 \cdot v_s \cdot N_D} \tag{6.19}$$

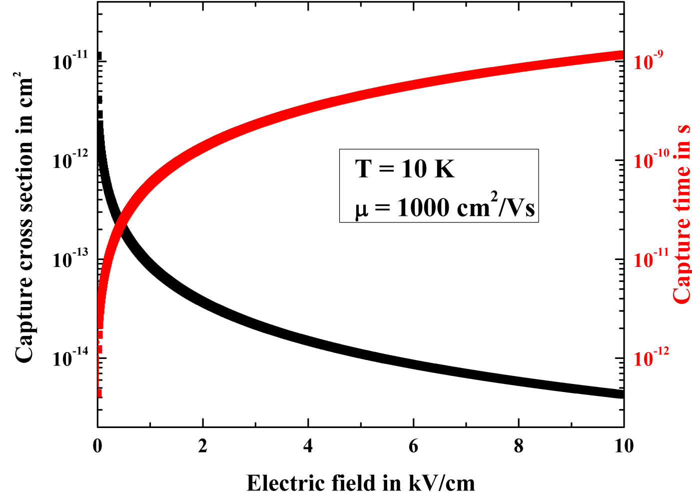

Figure 6.7: a) Calculated capture cross-section into a single shallow donor state and the capture time in dependence of the electric field at $T = 10$ K and $\mu = 1000\ \frac{\text{cm}^2}{\text{Vs}}$.

with $v_s = 2 \cdot 10^5\ \frac{\text{m}}{\text{s}}$ being the saturation velocity and $N_D = 10^{16}\ \frac{1}{\text{cm}^3}$ the doping concentration in the internal gate.
The freeze-out is connected with the electric field dependent recombination and plays an important role during the clear process. The critical region in the internal gate for the clear process is around the electron potential minimum, where the electric field is low.

6.2.3 DEPFET Simulation

The potential and the electric fields of the DEPFET in the collection and pulsed states (figure 6.3) can be calculated with the simulation program TESCA. TESCA solves the Poisson equation and the continuity equations for electrons and holes in semiconductors dynamically. As TESCA was not designed for cryogenic temperatures the validity of the results has to be limited.

1. Fully depleted internal gate

   The device is fully depleted, which means that the donors are completely ionized. The potential is defined by the concentration of the positively charged ionized donors and the boundary conditions at the contacts. So, the internal gate is assumed to be empty, unless signal charge arrives.

2. Small signal assumption

The DEPFET single pixel was irradiated with x-ray photons originating from a ^{55}Fe-source. The signal charge of a single event is 1600 electrons, which corresponds to a free carrier concentration in the internal gate of about $n = 10^{11}\ \frac{1}{\text{cm}^3}$. This concentration is below the ionized donor concentration in the internal gate, which is in the range of $10^{16} \frac{1}{\text{cm}^3}$. Consequently, the potential is not significantly influenced by the incoming signal charge.

3. Excessive presence of shallow donors

   The number of the shallow donors in the internal gate is much bigger than the number of incoming signal electrons. The dose of the deep implantation to create the internal gate is about $10^{12} \frac{1}{\text{cm}^2}$. The internal gate has a plain area (linearly structured DEPFETs) of about 8 μm x 6 μm = 48 μm^2. The number of the shallow donors can be estimated with $10^{12} \frac{1}{\text{cm}^2} \cdot 48 \mu\text{m}^2 = 4.8 \cdot 10^5$ and is bigger than the amount of incoming signal electrons per integration cycle. Therefore, every electron in the internal gate is captured by a shallow donor as long as it remains in the internal gate longer than the recombination time.

Potential distribution of the internal gate

Figure 6.8 shows the potentials of the internal gate for the cases, when the gate is in the collection state $V_{G,c} = -2$ V and in the pulsed state $V_{G,p} = +18$ V. For both cases the source and the drain-voltage are kept constant at $V_S = 0$ V and $V_D = -5$ V.

The potential maximum (electron potential minimum)[3] at $V_{G,c} = -2$ V is located near the source (position (x_1, y_1) in figure 6.8 a)). The transistor is turned on and an inversion layer is formed underneath the oxide of the gate. Consequently, the surface potential of the transistor channel depends on the source-drain voltage V_{SD}. The external gate is capacitively decoupled from the internal gate. The potential minimum is near the source, because it is more positive than the drain. The electrons in the internal gate are shifted in the direction of the source, but are still in the internal gate.
In contrast, at $V_{G,p} = +18$ V, the transistor is off and no inversion layer exists. Therefore, the internal gate is capacitively coupled with the external gate and the impact of the source or drain can be neglected. Consequently, the position of the potential maximum ((x_2, y_2) in figure 6.8 b)) is at the center of the transistor.
By increasing the gate voltage, the internal gate becomes more positive and the electrons are attracted towards the external gate. The internal gate minimum is shifted towards the external gate and the distance x_{12} between the electron potential minima of the pulsed and the collection state becomes higher:

[3] In the following chapters it is called the potential minimum.

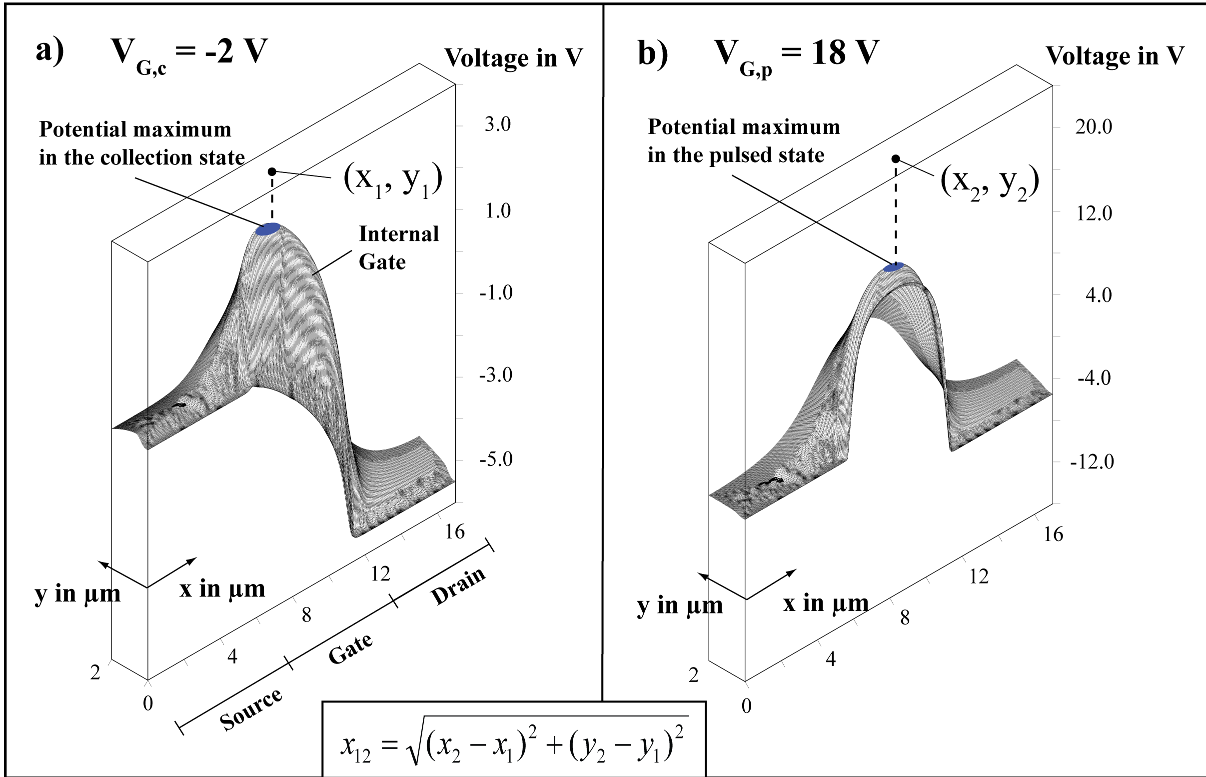

Figure 6.8: a) TESCA simulation of the potential maximum of the internal gate (potential minimum for electrons) in the collection state ($V_{G,c} = -2$ V). The source voltage is set to 0 V and the drain voltage is -5 V. The positive source results in a shift of the maximum towards the source. b) TESCA simulation of the potential maximum in the pulsed state ($V_{G,p} = +18$ V). The internal gate is coupled capacitively with the external gate and the maximum is located in the middle of the transistor.

$$x_{12} = \sqrt{(x_2 - x_1) + (y_2 - y_1)} \tag{6.20}$$

x_{12} is simulated and plotted against the applied gate voltage as shown in figure 6.9. It can be seen that x_{12} increases with a higher gate voltage. The potential minimum is in the middle of the internal gate at positive gate voltages, but it also can be shifted in y-direction. x_{12} is an important parameter, because it defines the average drift path of the electrons in the internal gate during the clear process.

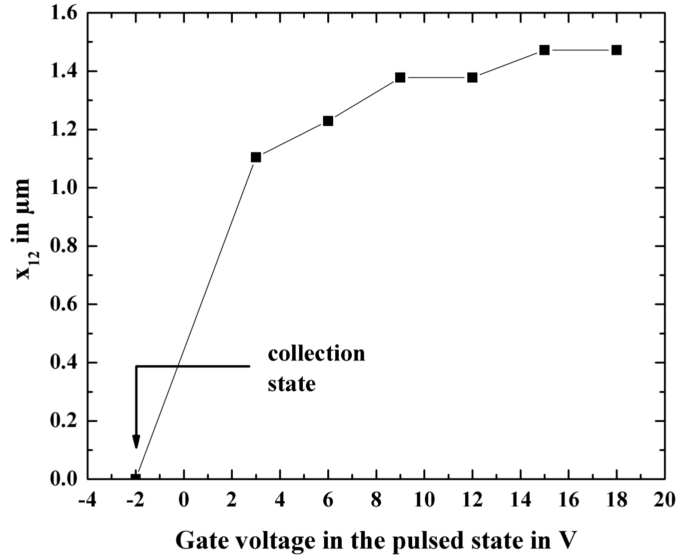

Figure 6.9: TESCA simulation of the distance x_{12} of the potential minima of state 1 and 2 against the pulsed gate voltage is shown. It presents the shift of the electron potential minimum, when the gate is pulsed from the collection into the pulsed state.

Electric field distribution

For modelling the reset mechanism, information about the emission times of each collected electron at a given gate voltage is needed. The electric fields are calculated, which are induced by the collected electrons in the internal gate, immediately after the gate is pulsed. Therefore, the DEPFET was simulated dynamically, when 1600 charge carriers are generated in the bulk. The charge cloud has an initial width of about 300 nm [48]. When the electrons arrive at the internal gate the electric fields in the collection state ($V_G = -2$ V) and in the pulsed state ($V_G = +6$ V, $+12$ V, $+18$ V) are calculated. Since TESCA simulates at room temperature, the free charge carriers are not trapped. In the simulation the electrons move from one potential minimum in the internal gate to the other instantly. Figure 6.10, left shows the spatial distribution of the free electron concentration in the internal gate in the collection state ($V_{G,c} = -2$ V). The position of the peak equals the position of the potential maximum in the collection state ((x_1, y_1) = (6.9 μm, 0.6 μm) as shown in figure 6.8, left. The dot matrix represent the lattice points, where the electron concentration is simulated. The sum of all dots of the simulated DEPFET is the simulation grid.

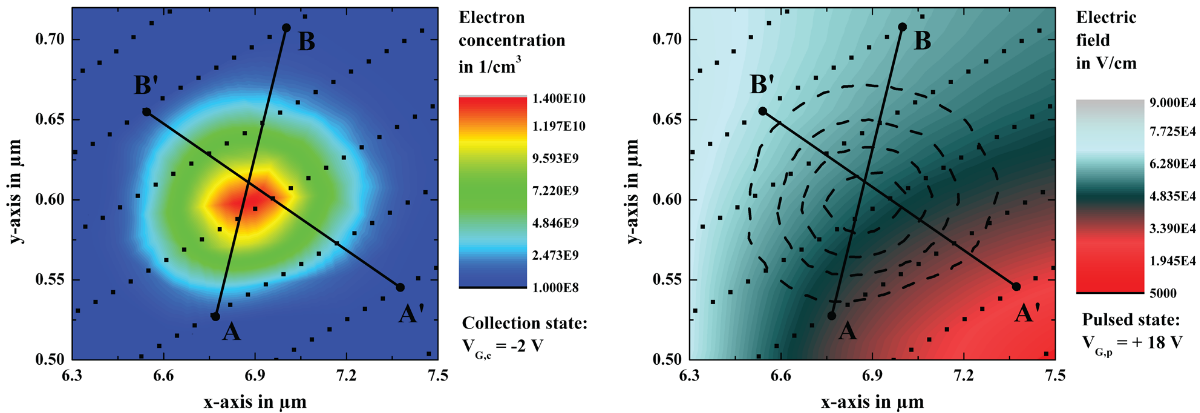

Figure 6.10: *Left:* TESCA simulation of the spatial distribution of the free electron concentration in the internal gate in the collection state ($V_{G,c} = -2$ V). The dot matrix represents the lattice points, where the electron concentration is simulated. The position of the peak equals the position of the potential maximum in the collection state ((x_1, y_1) = (6.9 μm, 0.6 μm) as shown in figure 6.8, left. *Right:* Spatial distribution of the electric field in the internal gate in the pulsed state ($V_{G,p} = 18$ V). The dot matrix represents the lattice points, where the electric fields were simulated. The position of the lattice points remains unchanged when simulating in the collection or pulsed state. The dashed circles illustrate the free electron concentration in the collection state. Therefore, the electric field can be determined, which is induced at the position of the collected electrons after pulsing the gate contact from $V_{G,c} = -2$ V to $V_{G,p} = 18$ V.

When the gate contact is pulsed from $V_{G,c} = -2$ V to $V_{G,p} = 18$ V, these electrons are exposed to an electric field. These fields force the electrons to emit into the conduction band as explained in subsection 6.2.1. The simulated electric field distribution including the lattice points are shown in figure 6.10. The position of the lattice points remains unchanged when simulating in the collection or pulsed state. Therefore, the electric field can be determined, which is induced at the position of each electron after pulsing the gate contact from $V_{G,c} = -2$ V to $V_{G,p} = 18$ V. The more precise the simulation grid the better the emission time constants for each electron can be determined.
Figure 6.11 shows the electric field distribution of the trapped electron concentration in the internal gate for different gate voltages in the pulsed state. The electron concentration and the electric field are only calculated at the lattice points, which reflects the discretized character of the distribution. The higher the gate voltage the higher the electric fields, which are induced at the position of the electrons. For each gate voltage two major peaks can be observed, which can be explained by the discretized lattice. In order to understand the electric field distribution a one dimensional cut along the lattice points is made (line A to B (or A' to B') in figure 6.10, right). The lines $\overline{AB}$ and $\overline{A'B'}$ are two examples and were randomly chosen.

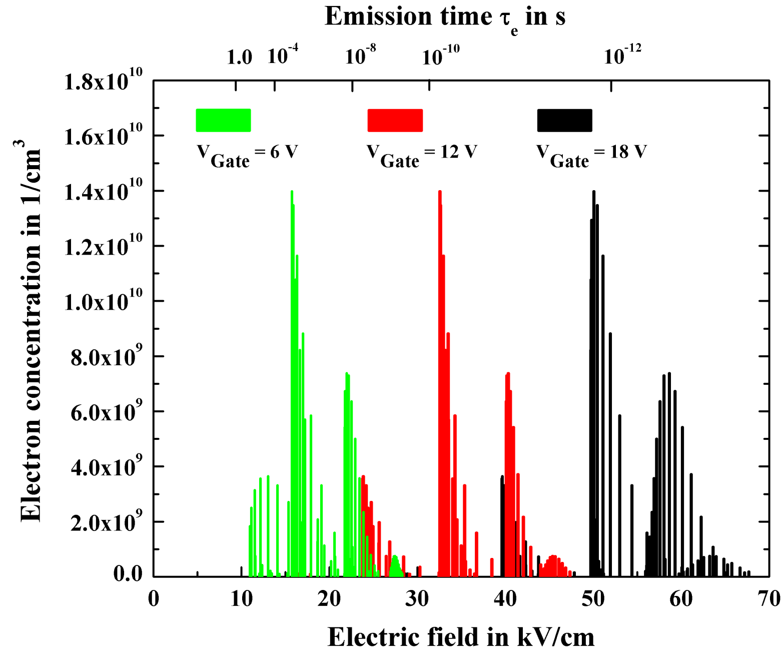

Figure 6.11: Electron concentration in the internal gate in dependence of the electric field, which is induced after pulsing the gate.[4]The electric field corresponds to an emission time constant, which is determined with equation 6.13 at a temperature of 6 K.

When following the line from point A (A') to point B (B') in figure 6.10, right, the electric field increases; besides, the electron concentration follows a Gaussian distribution in figure 6.10, left. It means, only for the one dimensional cut, the electron concentration is a Gaussian function of the electric field. Therefore, figure 6.11 is composed of a sum of one-dimensional Gaussian distributions.
The electric field distribution gives information for the emission time of the electrons, which is necessary for modelling the clear process at cryogenic temperatures and can be calculated by equation 6.13.

6.2.4 Electron transport in the internal gate

The electron transport after pulsing can be divided into two flow directions. Figure 6.12 shows the position of the internal gate minima in the pulsed and the collection state and the flow of the electrons after emission from the shallow donors. The transport from one potential minimum to the other (path a) in figure 6.12) is a pure drift current.

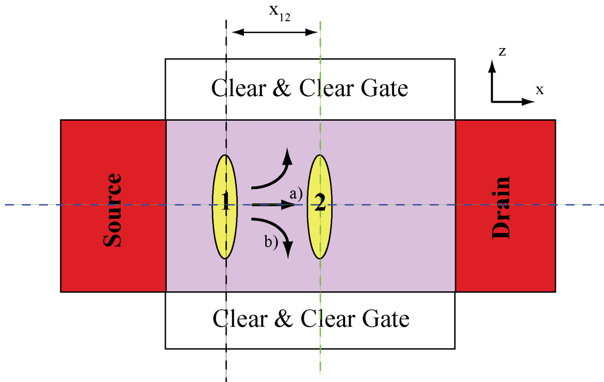

Figure 6.12: Top view of the internal gate. 1 denotes the potential minimum in the collection state and 2 for the pulsed state. The depth of 1 is 0.6 μm, while the positive gate voltage in the pulsed state shifts the electron potential minimum to 0.4 μm. The arrows indicate the flow of the electrons after they are emitted into the conduction band.

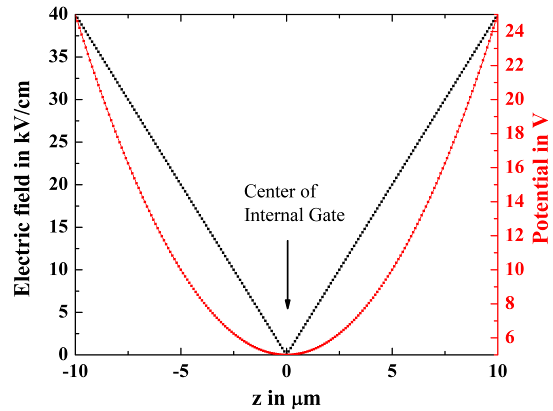

Figure 6.13: Calculated electric field in z-direction $E_z(z) = az$ and the potential $V(z) = a/2z^2$ along the green line in 6.12 at a depth of 0.6 μm ($V_G = -2$ V).

[4] The discrete values of the electric fields result from the discretization of the lattice.

The electrons drift in a potential gradient of about $\Delta V_{12} = 2.2$ V at $V_{G,p} = +18$ V from potential minimum 1 to minimum 2. In contrast, the movement perpendicular to path a) (path b) in figure 6.12) is composed of the drift and diffusion current. In the middle of the internal gate (dashed blue line in figure 6.12) the electric field in z-direction E_z is zero. The electrons near $z = 0$ diffuse to the clear contacts until they reach the high field regime induced by the clear contacts. In that region they drift without recombining.
The electron transport in the internal gate is modelled to find a solution for the electron concentration. The transport of the paths a) and b) is separated mathematically. As the electrons in path a) are exposed to an electric field in x-direction of $E_x = \frac{V_{12}}{x_{12}} \approx 12\ \frac{\text{kV}}{\text{cm}}$ they drift with the constant saturation drift velocity of $v_s = 2 \cdot 10^7\ \frac{\text{cm}}{\text{s}}$. For the electrons along path b), the drift and diffusion current in the internal gate in z-direction is determined. The equation for the current in one dimension can be formulated as follows [25]:

$$j_n = j_{drift} + j_{diff} \tag{6.21}$$

with

$$j_{diff} = eD \cdot \frac{\partial}{\partial z} n(z,t) \tag{6.22}$$

being the diffusion current and

$$j_{drift} = e \cdot n(z,t) \cdot \mu E_z(z) \tag{6.23}$$

the drift current. $D = \frac{\mu k_b T}{e}$ is the diffusion constant. The continuity equation is expressed by:

$$\frac{\partial n(z,t)}{\partial t} = \frac{1}{e}\frac{\partial}{\partial z} j_n - R(z) + G(z) \tag{6.24}$$

$R(z)$ and $G(z)$ are the spatial dependent recombination rate and the generation rate respectively. Equation 6.21 is inserted into 6.24 and one obtains a differential equation for n(z):

$$\frac{\partial n(z,t)}{\partial t} = D\frac{\partial^2}{\partial z^2} n(z,t) + \mu \cdot \frac{\partial}{\partial z}(n(z,t) \cdot E_z(z)) - R(z) + G(z) \tag{6.25}$$

The solution for the differential equation is the key to explain the reset at cryogenic temperatures. It includes all relevant physical processes: drift, diffusion, recombination and generation of electrons in the internal gate. The differential equation 6.25 is of first order in time and of second order in one spatial dimension. However, it is hard to solve the equation analytically. That is why, the problem is analysed by neglecting the recombination and generation and find an analytical expression for $R(z) = G(z) = 0$. A well known solution does exist for $E(z) = 0$, which is the Einstein-Smoluchowski equation [49]:

$$n_{diff}(z,t) = \frac{1}{\sqrt{\sigma_0^2 + D \cdot t}} \cdot \exp(\frac{-z^2}{\sigma_0^2 + D \cdot t}) \tag{6.26}$$

This equation presents the solution of the diffusion equation. In the depleted regime the potential is a parabolic function in dependence of z (figure 6.13). Thus, when the Maxwell equation is taken into account the electric field is a linear function in space $E_z(z) = a \cdot z$, where a is the electric field coefficient. It is a constant function. Consequently, the potential in z-direction can be formulated as $V(z) = a/2 \cdot z^2 + V_{iG}$. When the internal gate potential V_{iG} and the clear voltage V_{clear} are known it is possible to calculate the electric field coefficient a by using the parabolic equation for the potential:

$$V_{clear} = a/2 \cdot z^2 + V_{iG} \tag{6.27}$$

Diffusive transport dominates as long as the electrons are in the middle of the internal gate. The broader the electron cloud the more influence the electric field $E(z)$ has on the carrier transport. An ansatz with a time-dependent standard deviation is made:

$$n_{drift,diff}(z,t) = \frac{1}{\sqrt{f(t)}} \cdot \exp(\frac{-z^2}{f(t)}) \tag{6.28}$$

where $f(t)$ is a time-dependent function. When equation 6.28 is inserted into 6.25 and the initial condition 6.41 is taken into account the following relation for f(t) is obtained:

$$f(t) = \sigma_0^2 + \frac{4D}{\mu \cdot a} \cdot (\exp(2\mu a t) - 1) \tag{6.29}$$

f(t) is an exponential function of time and increases with mobility, the electric field coefficient a and time along the drift path in x-direction t_x. The drift time t_x is calculated by:

$$t_x = \frac{x_{12}}{v_s} \tag{6.30}$$

x_{12} is the distance between the electron potential minima as plotted from figure 6.9. With the saturation velocity $v_s = 2 \cdot 10^7\ \frac{\text{cm}}{\text{s}}$, the drift time, t_x ranges between 5.5 ps and 7.3 ps.
It is shown, that the Gaussian form of the electron cloud is conserved, when the electric field is a linear function of z. The standard deviation for the diffusive transport of $\sqrt{\frac{Dt}{4}}$ is replaced by $\sqrt{\frac{f(t)}{4}}$. When recombination processes occur, the free electron concentration is reduced and can break the Gaussian form. Equation 6.25 cannot be solved analytically and therefore, numerical methods are used.

6.3 The finite difference method

6.3.1 Description

For $R(z) \neq 0$ and $G(z) \neq 0$, it is hard to find an analytical expression for $n(z)$ as the recombination term is a complicated function of z. When $z = 0$, the recombination term is big enough to break the Gaussian form of $n(z)$ in equation 6.28. To explain the clear process of the DEPFET at low temperatures, it is necessary to describe the recombination and generation into/from the shallow donor states. Therefore, a model was developed, which contains the drift, diffusion, recombination and generation using the finite element method.
The advantage of this method is, that nearly all differential equations can be solved. The disadvantage is the complexity in implementation. During the calculation a huge amount of data is produced, which leads to high calculation times. As well, instabilities can occur when using an inappropriate proportion of space- and time steps [50].
Corresponding to numerical rules the derivations in terms of z and t are transformed as follows:

$$\frac{\partial n}{\partial z} \rightarrow \frac{n_{i+1}^t - n_{i-1}^t}{2\Delta z} \tag{6.31}$$

$$\frac{\partial^2 n}{\partial z^2} \rightarrow \frac{n_{i+1}^t - 2n_i^t + n_{i-1}^t}{\Delta z^2} \tag{6.32}$$

$$\frac{\partial n}{\partial t} \rightarrow \frac{n_{i+1}^t - n_i^t}{\Delta t} \tag{6.33}$$

The partial differential equation 6.25 is used to calculate the drift and diffusion. Equation 6.25 is discretized in values of Δz in space and in values of Δt in time:

$$\frac{n_i^{t+1} - n_i^t}{\Delta t} = D\frac{n_{i+1}^t - 2n_i^t + n_{i-1}^t}{\Delta z^2} + \mu a z_i(\frac{n_{i+1}^t - n_{i-1}^t}{2\Delta z}) + \mu a n_i^t \tag{6.34}$$

where $n_i^t = n(z_i)$ and $\tau_i^t = \tau(z_i)$ at the timestep t. At first, the generation $G(z)$ and the recombination $R(z)$ are examined seperately and set to $R(z) = G(z) = 0$. To calculate n_i^{t+1} equation 6.34 is rewritten in matrix form:

$$n_i^{t+1} = \mathbf{A}_{i,j}(\Delta z, \Delta t) \cdot n_j^t \tag{6.35}$$

where $\mathbf{A}_{i,j}$ is the matrix with the spatial indices i and j. i and j are the rows and columns respectively. n_i^{t+1} and n_j^t are vectors with i and j dimensions. Equation 6.35 is a linear equation with respect to the matrix elements of $\mathbf{A}_{i,j}$:

$$A_{i,i} = (\frac{-2D}{\Delta z^2} + \mu a)\Delta t + 1 \tag{6.36}$$

$$A_{i,i+1} = (\frac{D}{\Delta z^2} - \frac{\mu a z_i}{2\Delta z})\Delta t \tag{6.37}$$

$$A_{i,i-1} = (\frac{D}{\Delta z^2} + \frac{\mu a z_i}{2\Delta z})\Delta t \tag{6.38}$$

n_i^{t+1} is calculated for each timestep. Recombination is not included in equation 6.35. Therefore, the recombined electron concentration $n_{rec,i}^t = n_i^t \frac{\Delta t}{\tau_i}$ is calculated after each timestep and this value is subtracted from n_i^{t+1} for each lattice constant. $\tau_i = \tau_i(E(z_i))$ is the recombination time at a certain lattice point i in an electric field $E(z_i)$.
The measurable factor in the experiment is the amount of signal of electrons N_{rec}^T, which are frozen out and rest in the internal gate after reseting. Therefore, the concentration of recombined electrons n_{rec}^T is extracted after each pulse length T from equation 6.34. For N_{rec}^T, it is integrated over the whole internal gate (potential minima 1 and 2):

$$N_{rec}^T = \int_V n_{rec}^T dV = \int_{Pot_1} n_{rec}^T dV + \int_{Pot_2} n_{rec}^T dV \tag{6.39}$$

where the first term of the right side is the integral over the first potential minimum and the second term over the second potential minimum. In order to compare the experimental data with the data from the model, the factor ν_T is introduced, which is the proportion of N_{rec}^T and the total amount of collected electrons N:

$$\nu_T = \frac{N_{rec}^T}{N} \tag{6.40}$$

For the generation in potential minimum 1, the TESCA simulation data $n(\left|\vec{E}\right|)$ is used as described in chapter 6.2.3. The electric field corresponds to an emission time, which can be calculated with equation 6.13. The concentration of generated electrons $n_{gen}^t = n(\left|\vec{E}\right|)^t \frac{\Delta t}{\tau_e}$ is determined for the respective electric field after each timestep, where $\tau_e = \tau_e(\left|\vec{E}\right|)$. The generated electron cloud is in the conduction band and drifts towards potential minimum 2, while the electrons drift/diffuse towards the clear contacts.
The algorithm of the program is described as follows (figure 6.15):

1. **Generation**
   The electrons in the potential minimum 1 are emitted into the conduction band by electric field enhanced emission.

2. **Drift/Diffusion**
   The emitted electrons drift along path a) to the new potential minimum without being recombined. They diffuse/drift to the clear contacts along path b).

3. **Recombination**
   Only when the electrons arrive at the potential minimum 2 the recombination process occurs.

After the pulse length T, the gate is pulsed back from the pulsed state to the collection state and the algorithm runs in reverse direction. The recombined electrons in the second potential minimum are emitted into the conduction band. These electrons drift to the first potential minimum, where some of them recombine into the donors. This mechanism is repeated until the whole internal gate is empty. The schematic of building the equations for the numerical calculations and the complete algorithm of one loop is described in figures 6.14 and 6.15 respectively.

6.3.2 Electron dynamics

The algorithm is computed with the language C++. In this subsection the calculated electron concentrations $n(z)$ and $n_{rec}(z)$ in the second potential minimum after certain timesteps are discussed.

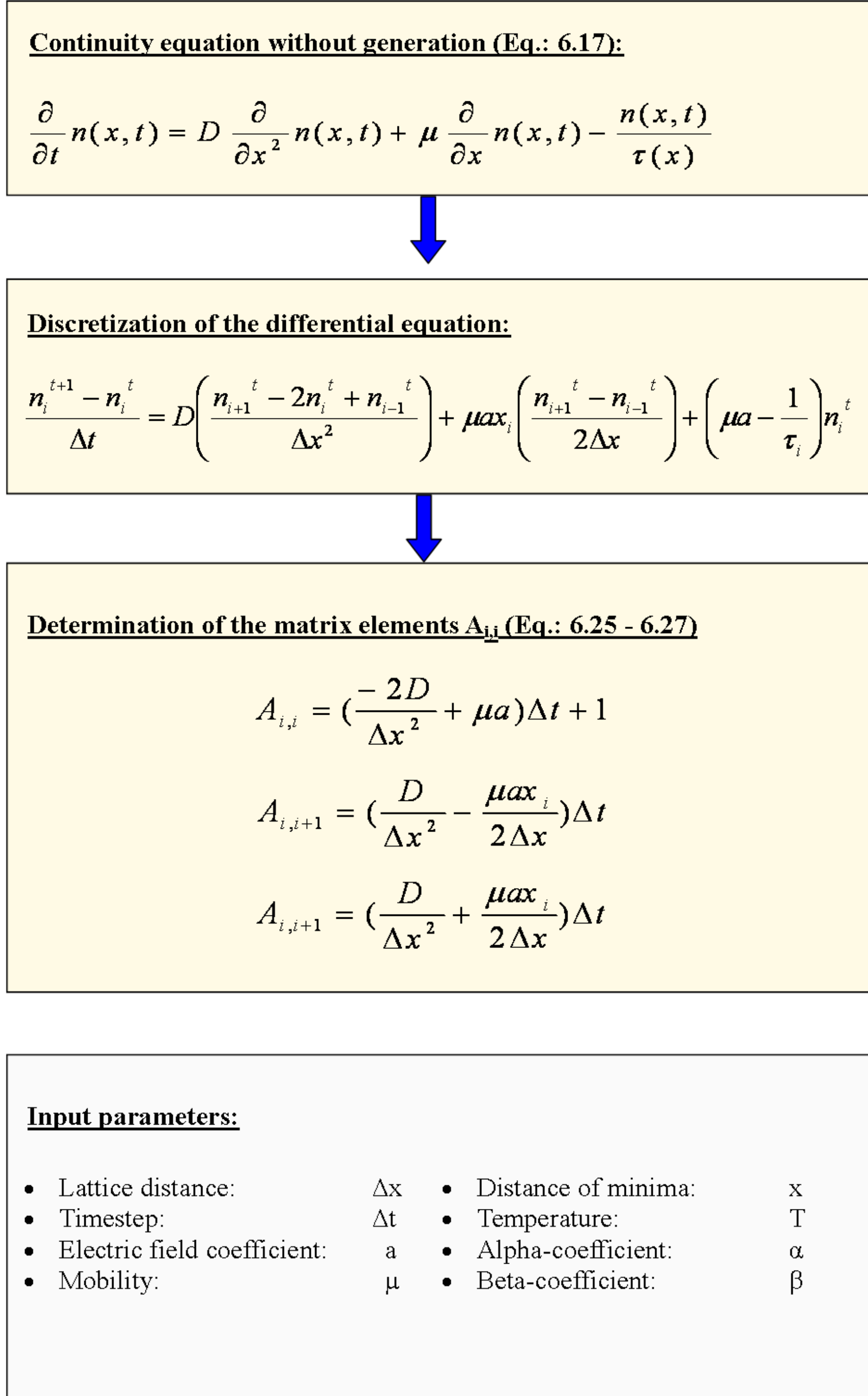

Figure 6.14: Schematic of building the equations for the numerical calculation. Additionally, there are the input parameters, which are needed for simulation.

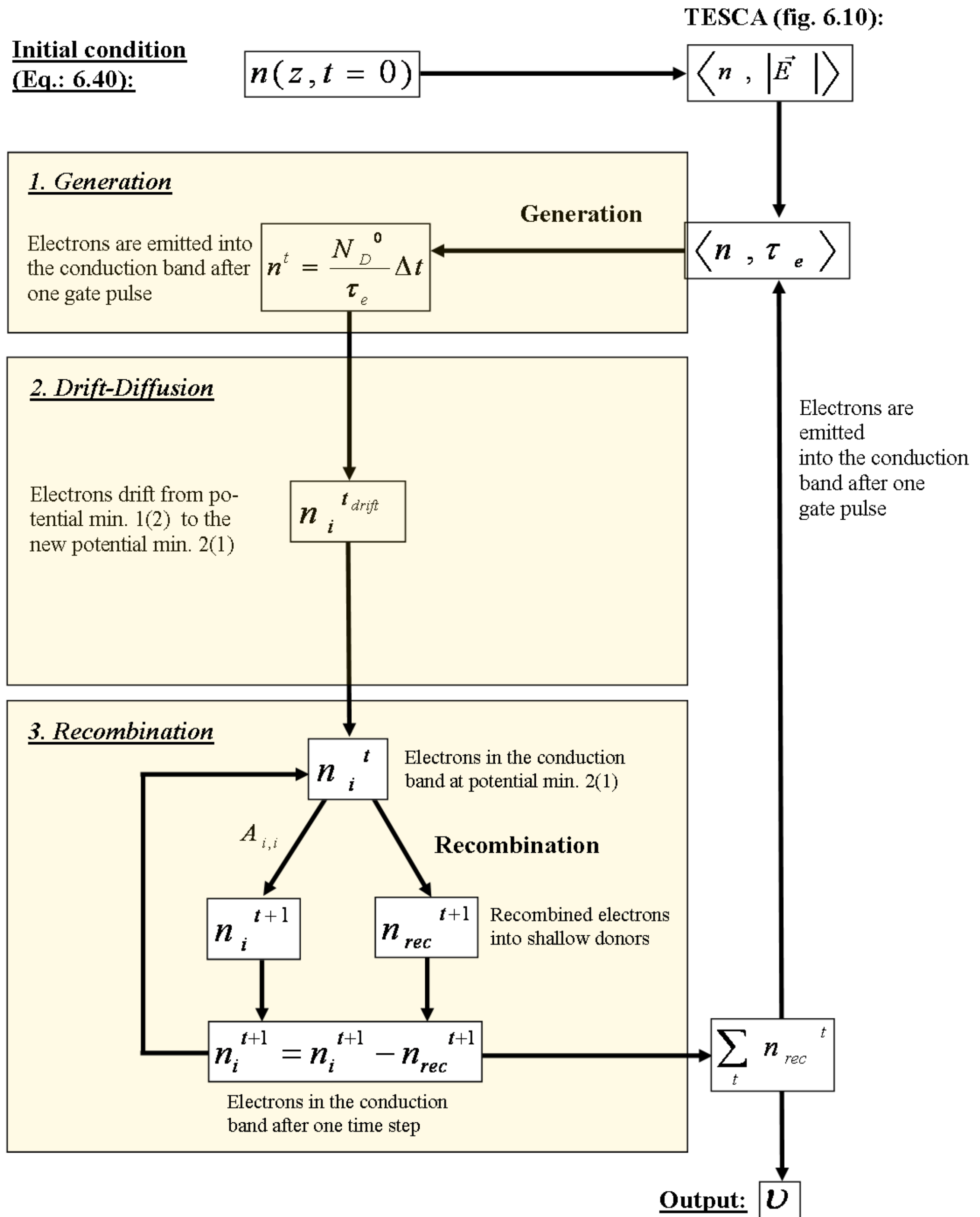

Figure 6.15: Algorithm to calculate the fraction ν_T of the amount residual recombined electrons after one gate pulse and the whole amount of signal electrons.

Initial condition

The simulation of the differential equation 6.34 needs an initial condition in order to calculate the further points in time. For the collected electrons in the internal gate a Gaussian function is assumed:

$$n(z, t = 0) = \frac{1}{\sqrt{2 \cdot \pi \sigma_0^2}} \cdot \exp\left(\frac{-z^2}{2\sigma_0^2}\right) \tag{6.41}$$

$t = 0$ is the time, when the gate is pulsed and before the electrons are emitted by electric field enhanced emission. σ_0 is the standard deviation of the electron cloud in the internal gate. Equation 6.41 is the initial condition for the differential equation in 6.34.

Input parameters

The input parameters are discussed, which are used to run the simulation program. The following values at the gate voltage in the pulsed state $V_{G,p} = +18$ V are chosen:

- Lattice distance: $\Delta z = 40$ nm
- Time step: $\Delta t = 10$ fs
- Electric field coefficient: $a = 3 \cdot 10^{11}\ \frac{\text{V}}{\text{m}^2}$
- Mobility of electrons: $\mu = 1 \cdot 10^3\ \frac{\text{cm}^2}{\text{Vs}}$
- Distance between the pot. maxima in collection and pulsed state: $x_{12} = 1.47\ \mu$m
- α-coefficient: $\alpha = 1$
- β-coefficient: $\beta = 10^{-3}$
- Temperature: $T = 6$ K

In the following these parameters are discussed. Before running the program, the stability of the numerical equation 6.34 must be checked. It is important to prove the conditions, which lead to a stable simulation program. Therefore, the Neumann stability analysis is used. The independent solutions, or eigenmodes, of the difference equations are all of the form [50]:

$$n_i^t = \xi^t \cdot e^{jki\Delta z} \tag{6.42}$$

where k is a real spatial wave number, j is the imaginary unit and $\xi = \xi(k)$ is a complex number, that depends on k. k can reach any value. The time dependence of a single eigenmode is the successive integer powers of the complex number ξ. Accordingly, equation 6.34 is unstable if $|\xi(k)| > 1$ for some k. $\xi(k)$ is called the amplification factor. Equation 6.42 is substituted into 6.34 and one gets for the absolute value of the amplification factor:

$$|\xi(k)| = \sqrt{(2D\Delta t\frac{cos(k\Delta z)}{\Delta z^2} + 1)^2 + (\mu a z_i \Delta t\frac{sin(k\Delta z)}{\Delta z})^2} \tag{6.43}$$

$|\xi(k)|$ is plotted in dependence of k in figure 6.16 for different Δz and Δt. If $\Delta x = 4$ nm and $\Delta t = 100$ fs one obtains $\xi(k) > 1$ for $6.5 \cdot 10^8 < k < 9.2 \cdot 10^8$. It means, that these input parameters result in unstable solutions after a certain iteration step. If Δt is too large or Δz too low, the left side of equation 6.35 increases too fast. The electron concentration of the lattice points becomes unrealisticly high, which result in unstable solutions. Consequently, the timestep must be small enough to generate stable solutions, but high enough to calculate a long pulse length. Another approach is to increase Δz. However, this results in a low resolution of the hole lattice. A stable solution for $\Delta z = 40$ nm and $\Delta t = 10$ fs at a diffusion constant of $D = \frac{\mu k_B T}{e} = 0.51 \cdot 10^{-4}\ \frac{\mathrm{m}^2}{\mathrm{s}}$ at $T = 6$ K is found. If the stability criterion is not fulfilled, the solution does not converge.

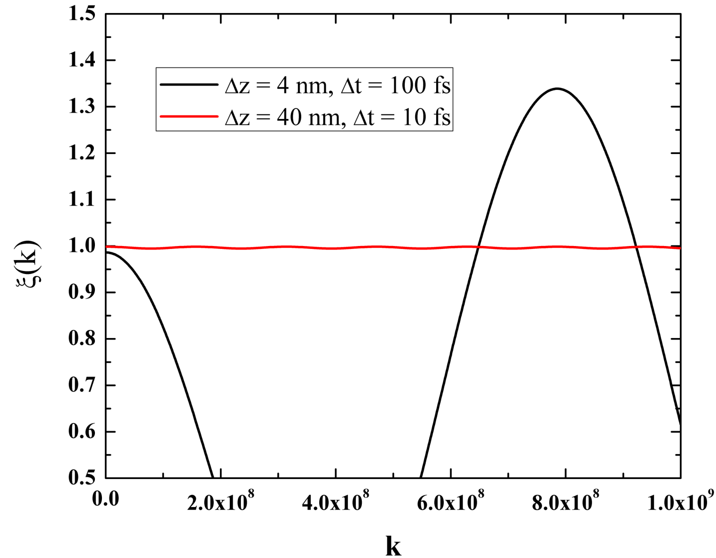

Figure 6.16: Calculated amplification factor $\xi(k)$ in dependence of k for different values of Δz and Δt.

The calculations lasted five days on a state of the art PC for a pulse length of $T = 1$ ns. For the electric field coefficient a the potential distribution along the cut 'clear - internal gate - clear' in the pulsed state and collection state for $V_{G,p} = 18$ V and $V_{clear} = 25$ V was calculated. Important is the relative potential between the clear contact V_{clear} and the internal gate V_{iG}. The distance between the two points is estimated from design plots of linearly structured DEPFETs and is 10 μm. Then, the electric field coefficient a can be determined from equation 6.27:

$$V_{clear} = a/2 \cdot (10\mu\text{m})^2 + V_{iG} \tag{6.44}$$

$$\Rightarrow a = 2 \cdot \frac{V_{clear} - V_{iG}}{(10\mu\text{m})^2} \tag{6.45}$$

The internal gate potential in the pulsed state is $V_{iG,p} = 15$ V and in the collection state $V_{iG,c} = 4.8$ V. In the pulsed state one obtains $a = 2 \cdot 10^{11}\ \frac{\text{V}}{\text{m}^2}$ and in the collection state $a = 4 \cdot 10^{11}\ \frac{\text{V}}{\text{m}^2}$.
The mobility at cryogenic conditions is strongly dependent on the doping concentration and the temperature. The mobility was determined by a semi-empirical model and is $\mu = 10^3 \frac{\text{cm}^2}{\text{Vs}}$ at $N_D = 10^{16}\ \frac{1}{\text{cm}^3}$ and $T = 10$ K [26].
The recombination time τ_i at the position z_i is calculated by using following expression:

$$\tau_i = \frac{1}{v_s \cdot N_D \cdot \sigma_i} \tag{6.46}$$

where v_s is the saturation velocity, N_D is the concentration of ionized donors in the internal gate and σ_i is the capture cross section at the position z_i. The electric field at each lattice point is determined by the relation $E_i = E(z_i) = a \cdot z_i$. The capture cross section σ_i at each lattice point is calculated as described in subsection 6.2.2. The probability of an effective trapping event is described by the semi-empirical factor β. It is determined by calibrating the zero-field capture cross-section of equation 6.15 with the experimental value of $\sigma = 1.0 \cdot 10^{11}$ cm^2 at $T = 10$ K [47]. In this case β has the value $2 \cdot 10^{-3}$. It means, when the electron crosses the shallow donor, the mean probability to capture an electron is 0.1 %. As discussed in subsection 6.2.2 the α-coefficient has the value 1 [45].

Results of the simulation

Figure 6.17 shows the time evolution of the free electron concentration in the second potential minimum of the internal gate (figure 6.12). The recombined electrons n_{rec} are

shown in figure 6.18.
After 12.5 ps, first electrons, which are emitted from the first potential minimum, reach the second potential minimum. There, the recombination rate is highest as the electric field is zero. At the same time, when the electrons accumulate at the second potential minimum after 13 ps, the Gaussian form of the free electron cloud begins to split. On the one hand the electric field forces the electrons to drift to the clear contacts. On the other hand the diffusion is effective in the opposite direction. The electrons at the left edge of the right cloud diffuse to the middle of the internal gate, which leads to an increased recombination. The electrons recombine into the shallow donors in the middle of the internal gate as long as free electrons do exist. The electric field causes the split electron cloud to disperse in the respective direction. After 24 ps no free electrons are in the middle of the internal gate and two seperate electron clouds arise. The concentration of the recombined electrons does not increase significantly as the free electrons are in the higher field regime.

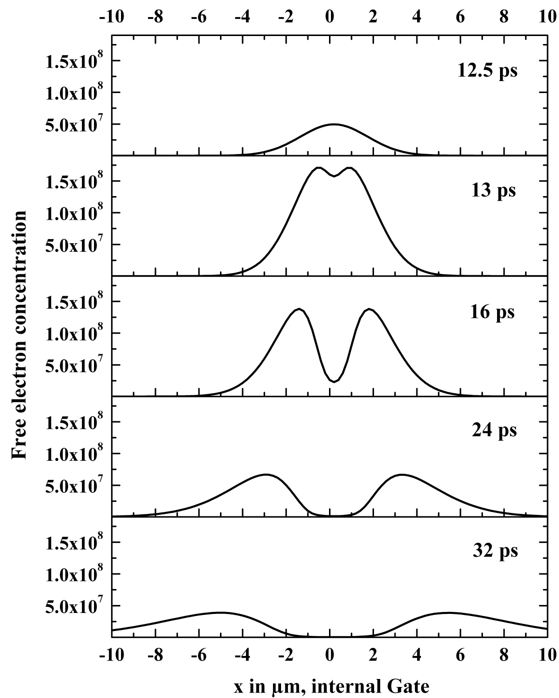

Figure 6.17: Simulation of the free electron concentration at the potential minimum 2 (figure 6.12) at different time steps.

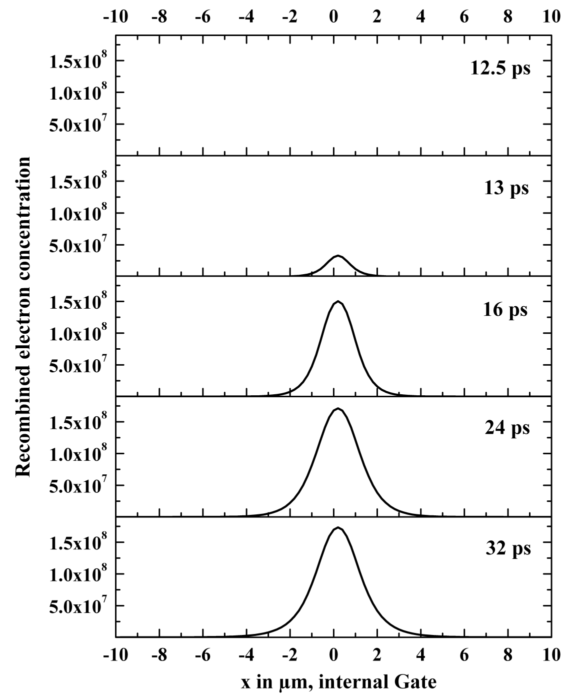

Figure 6.18: Simulation of the recombined electron concentration at the potential minimum 2 (figure 6.12) at different time steps.

After 32 ps the electric field $\overrightarrow{E} \approx 15\ \frac{\text{kV}}{\text{cm}}$ is strong compared to the diffusive forces. The free electrons drift to the clear contacts without recombining, while the recombined electrons remain in the internal gate.
The results show that one part of the emitted electrons are recaptured in the second potential minimum. The other part reaches the clear contacts. The important parameter is the fraction of recombined electrons ν_T after one pulse, because this indicates the clear performance of the DEPFET. In figure 6.19 ν_T is plotted in dependence of the number of clear pulses for different doping concentrations. It can be seen that a decrease of the doping concentration to about $N_D = 10^{15}\ \frac{1}{\text{cm}^3}$ in the internal gate can enhance the reset significantly. First the recombination rate is decreased by one order of magnitude. The electrons have more time to drift to the clear contacts before they recombine into shallow donors. Additionally, the mobility is enhanced by a factor of 2 [26]. This results from the fact, that the electrons scatter on a lower concentration of impurities. As the scattering time at cryogenic temperatures is limited by the impurities, the mobility (see appendix, subsection 3.4) increases with lower doping concentration. This has the consequence, that the recombination rate is reduced again according to equation 6.16. Also, the electrons can drift faster to the clear contacts.

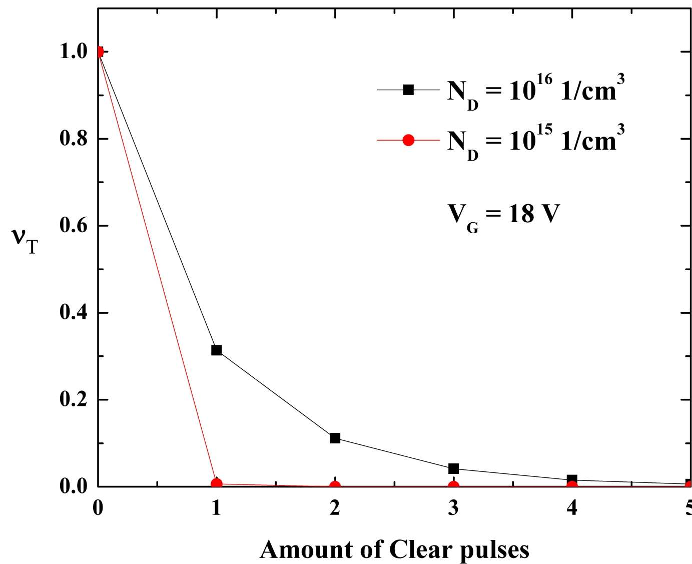

Figure 6.19: Simulated fraction of recombined electrons ν_T against the number of clear pulses for different doping concentrations of the internal gate.

The reduction of the doping concentration enhance the clear process significantly, but reduces the charge handling capacity. With existing DEPFETs ($N_D = 10^{16}\ \frac{1}{\mathrm{cm}^3}$) it is possible to collect about 100.000 electrons without degrading the performance, i.e. the linearity [33]. Therefore, reduction of doping concentration only makes sense if few photons per integration cycle (up to 10.000 generated electrons) are detected.
However, the enhancement of the clear performance by reduction of the doping concentration is not valid in every case. It depends on the average emission time of the collected electrons which exceeds the pulse width or not. There are two cases:

1. **The emission time is shorter than the pulse width:** If the electric field is high enough, all electrons are emitted into the conduction band in a time, which is shorter than the pulse width. The electrons drift/diffuse to the new electron potential minimum. Drift/diffusion and recombination dominate the electron dynamics. As the drift/diffusion is characterized by the mobility and the recombination is dependent on the doping concentration, the clear performance can be enhanced by a reduction of the doping concentration.

2. **The emission time is larger than the pulse width:** If the electric field is low, the electrons stay in the shallow donors of the potential minimum and are not emitted. The electrons are exposed to the electric field as long as the pulse lasts. As the frozen electrons do not drift/diffuse and do not recombine, the mobility and the doping concentration do not change the number of recombined electrons. Only, when the electrons are in the conduction band the mobility has a significant impact on the drift/diffusion and recombination. Therefore, the reduction of the doping concentration does not have an impact on the clear performance.

In section 6.4 the two cases are discussed with respect to the experimental results.

6.4 Experimental results and discussion

The aim is to map the model described in section 6.2 with the experimental results. Therefore, the parameter ν is discussed, which is the fraction of the residual electrons N_{e^-} in the internal gate to the whole number of the electrons induced by the signal N_{sig} after the m-th clear pulse:

$$\nu(m) = \frac{N_{e^-}(m)}{N_{sig}} \tag{6.47}$$

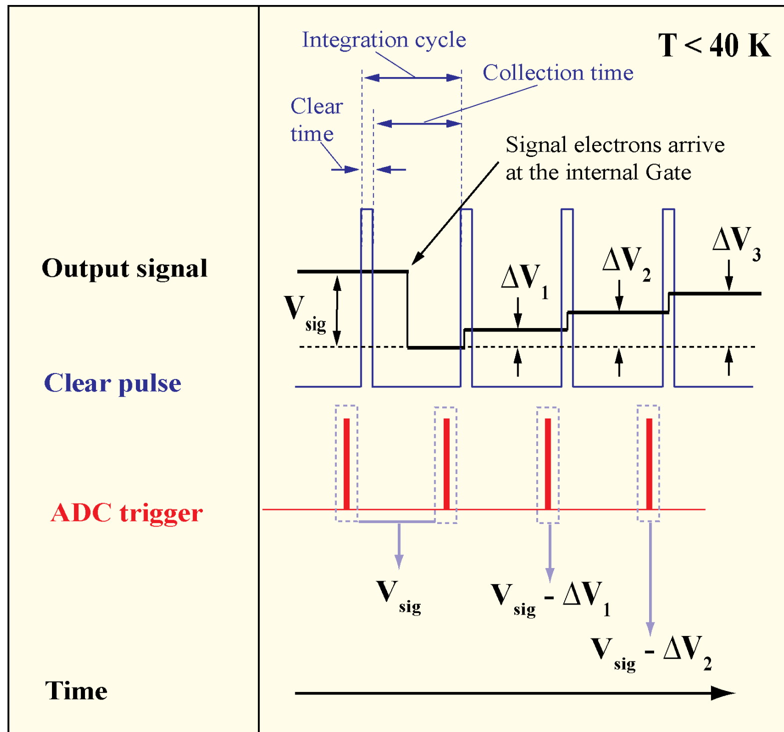

Figure 6.20: Sample scheme to determine the output voltage jump ΔV_m. The signal height is determined as illustrated in figure 4.11. After applying the clear pulse the output voltage is increased by a value of ΔV_m.

The theoretical ν_T was discussed in section 6.3 and was defined in equation 6.40:

$$\nu_T(m) = \frac{N_{rec}(m)}{N_{sig}} \tag{6.48}$$

In section 4.3 the fraction of the residual electrons in the internal gate to the whole number of the electrons induced by the signal N_{sig} after the m-th clear pulse is determined experimentally. In figure 6.20 the sample scheme to obtain the output voltage jump ΔV_m is shown. The experimental ν_E in dependence of the number of clear pulses m is a function of the output voltage jump ΔV_m and the signal height V_{sig} from equation 4.11:

$$\nu_E(m) = 1 - \frac{\Delta V_m}{V_{sig}} \tag{6.49}$$

ν_E is determined as a function of gate voltage, gate pulses and pulse widths to investigate the clear performance in terms of the previously discussed parameters. These parameters were varied to find out the dominating and/or limiting physical processes, which are illustrated in figure 6.15. The setup was used as described in section 4.1. Additionally, a parameter space was found, where the internal gate was completely cleared with one clear pulse.

6.4.1 Dependence on the gate- and clear pulse width

The clear performance was investigated in dependence of the width of the gate- and clear pulses. During the clear time the gate is pulsed only once. Figure 6.21 shows the measured clear performance for different gate pulse widths at a constant clear time of 2100 ns. The gate pulse is applied 210 ns after the beginning of the clear sequence (figure 6.2). The reset is not improved significantly due to the increased pulse width.
The clear pulse is also increased at a constant gate pulse width of 42 ns as shown in figure 6.22. Also, in this case, the clear performance is not improved. The limited bandwidth of the FPGA of 24 Mhz allows pulse widths of a minimum of 42 ns.
As shown in figure 6.3 the relevant time for the effective reset begins immediately after the pulse is applied. The pulse width is compared with the average time for the processes for emission, recombination and drift/diffusion t_{dyn}:

$$t_{dyn} = \langle\tau_e\rangle(V_G = 16\ \text{V}) + \tau_r + t_{drift} \tag{6.50}$$

where $\langle\tau_e\rangle(V_{G,p} = 16\ \text{V})$ is the average emission time at $V_{G,p} = +16$ V in the potential minimum 1. The electric fields were calculated with TESCA to find out the corresponding

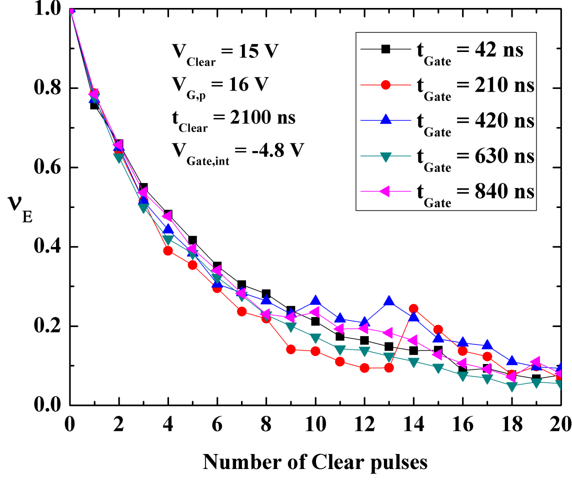

Figure 6.21: Measured fraction of remaining electrons ν_E in dependence of the number of clear pulses for different gate pulse widths.

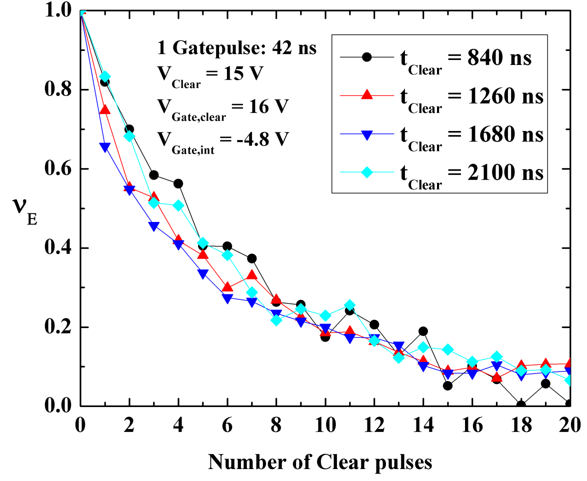

Figure 6.22: Measured fraction of remaining electrons ν_E in dependence of the number of clear pulses for different clear pulse widths.

emission time. For $V_{G,p} = +16$ V, an average electric field for all collected electrons of about 42 $\frac{\text{kV}}{\text{cm}}$ is obtained. From equation 6.13 the average emission time is calculated to $\langle\tau_e\rangle(V_G = 16\text{ V}) \approx 1$ ps. $\tau_r(\left|\vec{E}\right| = 0)$ is the recombination time in the potential minimum 2. For $\left|\vec{E}\right| = 0$, the recombination time can be calculated by:

$$\tau_r(\left|\vec{E}\right| = 0) = \frac{1}{\sigma v_{th} N_D^+} = 10\text{ ps} \tag{6.51}$$

$v_{th} = \sqrt{\frac{k_b T}{m^*}} = 1.8 \cdot 10^6 \frac{\text{cm}}{\text{s}}$ is the thermal velocity at $T = 6$ K and $N_D^+ = 10^{16}\ \frac{1}{\text{cm}^3}$ is the density of ionized donors in the internal gate. The capture cross section at 6 K is $\sigma = 2 \cdot 10^{-11}\ \text{cm}^2$ [47].

t_{drift} is the drift time, which is needed to drift from potential minimum 1 to 2:

$$t_{drift} = \frac{x_{12}}{v_{drift}} = \frac{1.47\ \mu m}{2 \cdot 10^7\ \frac{\text{cm}}{\text{s}}} = 7.4\text{ ps} \tag{6.52}$$

The average time for t_{dyn} is estimated to be 18.4 ps. The times for the pulse widths t_G are greater than the time, which is needed for the transport and trapping processes of the electrons:

$$t_G >> t_{dyn} \tag{6.53}$$

After recombination, the electrons stay in the shallow donors of the potential minimum and no electron transport occurs in the internal gate. Independent from the duration of the gate pulse, they stay in the potential minimum until the next pulse is applied.
Immediately after emission, the electrons are in the conduction band and can drift/diffuse to the clear contacts. The clear process can only be improved by increasing the dwell time of the electrons in the conduction band. Then, the electrons have more time to diffuse and reach the high field region of the clear contacts.
The results can also be understood by consulting the simulation program described in section 6.3. The electron dynamics was simulated for the aforementioned conditions. Figure 6.23 shows the simulation of the number of the trapped electrons in the potential minimum 2 in dependence of time. Immediately after the gate is pulsed nearly all electrons are emitted and are in the conduction band. At 12.5 ps the electrons reach the second potential minimum and recombine with the shallow donors. The plot shows the time from the beginning of the simulation and it can be seen, that the density of the trapped electrons is constant at $t > 25$ ps.

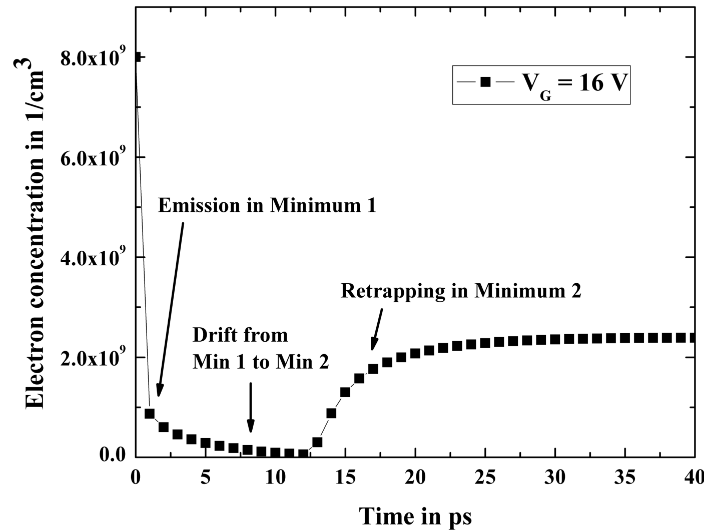

Figure 6.23: Simulation of the entire trapped electron concentration in the internal gate in potential minima 1 and 2 in dependence of the time. The results were obtained with the simulation program described in section 6.3. $t = 0$ s defines the time before electric field enhanced emission occurs and after the gate is pulsed.

After that time the concentration of the trapped electrons in the potential minimum 1 and 2 does not change. The clear/gate pulse time can last several microseconds and the electrons stay trapped. Consequently the clear performance is independent of the clear and gate time.

6.4.2 Gate pulse

The proposed model was verified by varying the number of gate pulses during the clear time. The experimental parameter ν_E was determined for different gate voltages as shown in figure 6.24 and 6.25. At $V_{G,p} = +18$ V the clear performance is improved, when more pulses are applied. When 10 gate pulses per clear are applied, the internal gate is empty after one clear pulse. By applying multiple pulses the electrons are emitted continously, which leads to an increase of the dwell time of the electrons in the conduction band. Consequently, the electrons have more time to diffuse/drift to the clear contacts. The emission time and the drift time are much shorter than the gate pulse width. In this case, the electron transport limits the clear performance.
In contrast, at $V_{G,p} = +6$ V, more than 20 clear pulses are needed. The clear performance does not change when one or 20 gate pulses are applied. It is not possible to remove the electrons by one clear pulse.

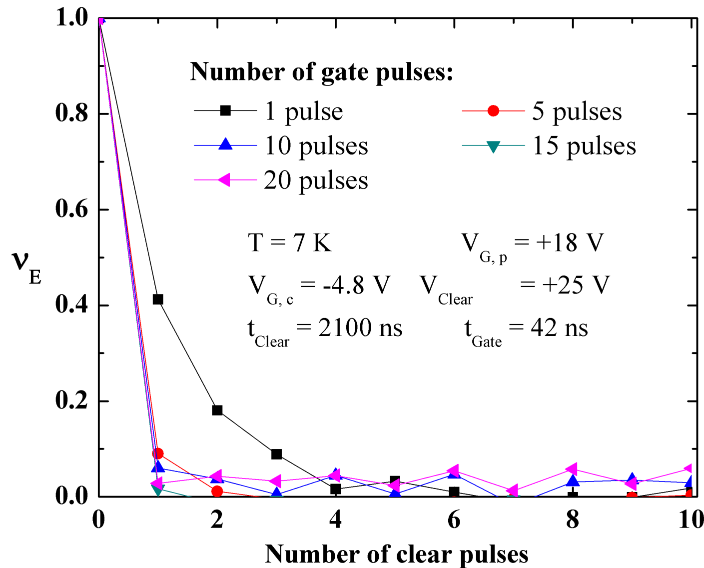

Figure 6.24: Measured fraction of remaining electrons ν_E in dependence of the number of clear pulses for $V_{G,p} = 18$ V.

Relative to $V_{G,p} = +18$ V, this can be explained by the lower electric fields in potential minimum 1 and the short drift path x_{12}. The average electric fields are in the range of 16 $\frac{\text{kV}}{\text{cm}}$, which corresponds to a theoretical value of the mean emission time according to equation 6.13:

$$\langle \tau_e \rangle_{theo}(V_{G,p} = 6 \text{ V}) = 20\ \mu\text{s} \tag{6.54}$$

The drift time and the recombination time are in the range of picoseconds and can be neglected relative to $\langle \tau_e \rangle_{theo}(V_{G,p} = 6V) = 20\ \mu$s. Thus, the emission time is greater than the gate pulse width of 42 ns and following relation is obtained:

$$42\ ns = t_G << t_{dyn} \approx \langle \tau_e \rangle_{theo}(V_{G,p} = 6V) = 20\ \mu s \tag{6.55}$$

In this case the clear performance is limited by the emission from the shallow donor state. The experimental value of the mean emission time is obtained, when ν_E is decreased by $1/e$. The curve in figure 6.25 is fitted with an exponential function; the number of clear pulses, which is needed to decrease ν_E by $1/e$, is 3.8 ± 0.2 [5].

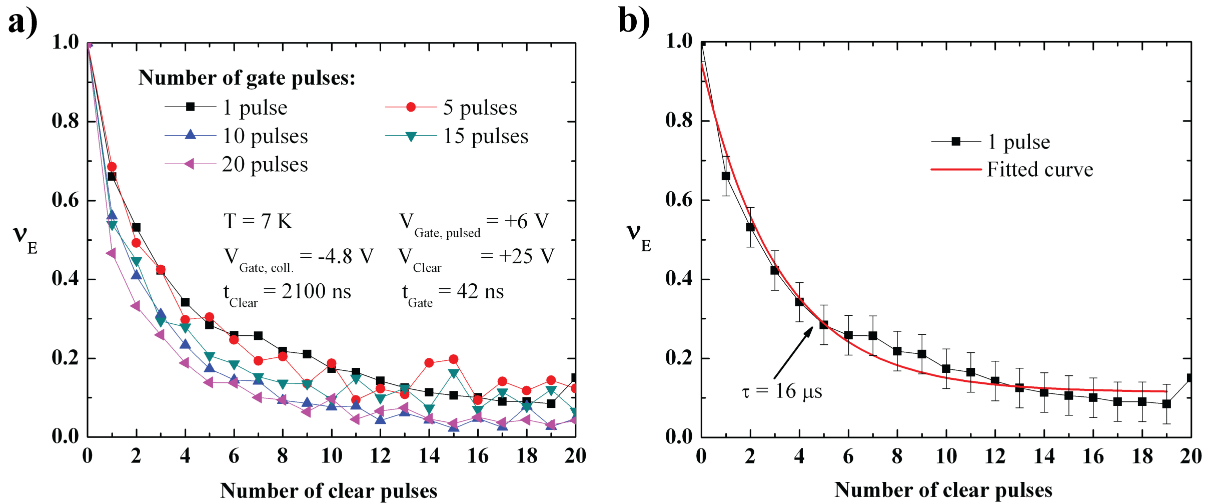

Figure 6.25: a) Measured fraction of remaining electrons ν_E in dependence of the number of clear pulses for $V_{G,p} = 6$ V. b) The curve (one gate pulse) is fitted with an exponential function.

[5] The number of clear pulses is an integer number. The value for ν_E is between 3 and 4.

The time of one clear pulse is $t_{clear} = 4.2\ \mu$s and the experimental value of the mean emission time is calculated to:

$$\langle \tau_e \rangle_{exp}(V_{G,p} = 6V) = (3.8 \pm 0.2) \cdot 4.2\ \mu\text{s} = (16 \pm 0.8)\ \mu\text{s} \tag{6.56}$$

The theoretical and experimental values do not correspond, but are in the same order of magnitude. The reason is that the actual electric fields in the device in the experiments are higher due to three-dimensional effects. The previously mentioned average electric fields of 16 $\frac{\text{kV}}{\text{cm}}$ at $V_{G,p} = 6$ V were determined with the simulation program TESCA, which calculates in two dimensions.
Multiple pulsing does not improve the clear performance as the transport from potential minimum 1 to 2 is not the limiting process. The main part of the collected electrons remains in the first potential minimum. Only a few electrons are emitted and diffuse to the high field region, where they drift to the clear contacts.

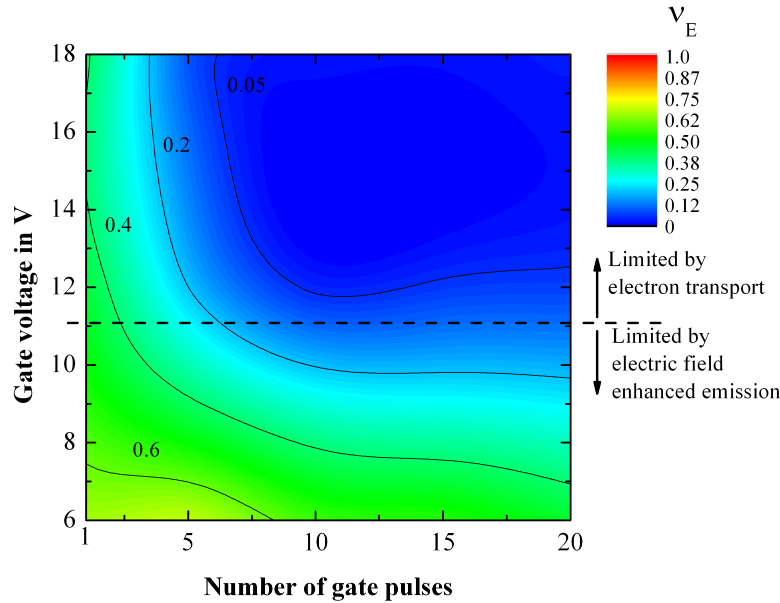

Figure 6.26: Measured fraction of remaining electrons ν_E after one clear pulse in dependence of the gate voltage and the number of gate pulses at $V_C = +25$ V. The duration of the clear pulse and the gate pulse are $t_{clear} = 2100$ ns and $t_{gate} = 42$ ns respectively. [6]

[6] The two-dimensional plot is a continous distribution of the parameter ν. Only, the data at the number of gate pulses 1,5,10,15 and 20 are experimentally determined. The rest of the points are approximated linearly.

Figure 6.26 illustrates the operating conditions, where the clear performance is limited by the electron transport due to the drift from potential minimum 1 to 2 or by electric field enhanced emission. It shows a two-dimensional plot, where the color denotes the fraction of remaining electrons after the first clear pulse. The clear voltage is set to $V_C = +25$ V. At gate voltages higher than +11 V, ν_E varies strongly with increasing number of gate pulses. In this regime the clear performance is limited by the electron transport from potential minimum 1 to 2. It is possible to improve the reset by applying several gate pulses. Below $V_{G,p} = +11$ V, ν_E does not vary with respect of the number of gate pulses. The clear performance is limited by the electric field enhanced emission and it is not possible to remove the electrons from the internal gate with one clear pulse. This picture changes, when the clear voltage is set to $V_C = +15$ V as shown in figure 6.27. It is evident, that the clear performance is reduced. The electric field coefficient a is reduced, which results in a slower expansion of the electron cloud in z-direction. At higher gate voltages there is a region where ν_E does not change significantly with the number of gate pulses. To analyze this phenomenon, the peak potential in the internal gate with TESCA was simulated.

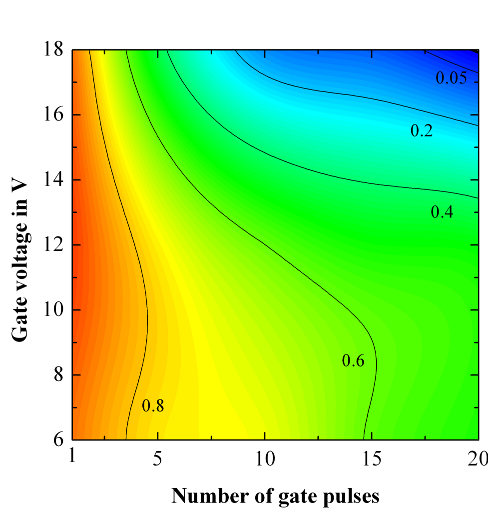

Figure 6.27: Measured fraction of remaining electrons ν_E after one clear pulse in dependence of the gate voltage and the number of gate pulses $V_C = 15$ V. The duration of the clear pulse and the gate pulse are $t_{clear} = 2100$ ns and $t_{gate} = 42$ ns respectively. [7]

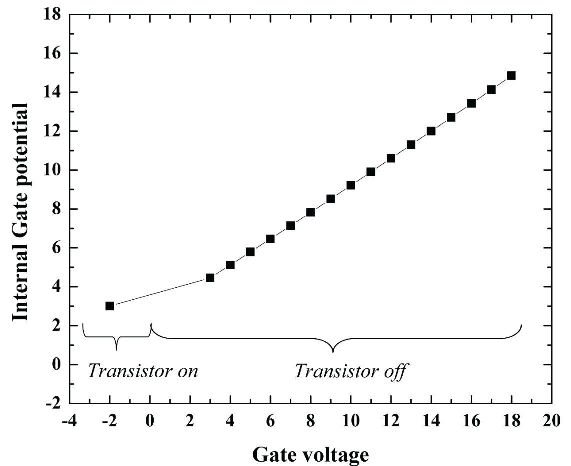

Figure 6.28: TESCA simulation of the internal gate peak potential in dependence of the gate voltage.

[7] See footnote 6.

For the calculation the cut 'source - gate - drain' was used, which is identical with the structure shown in the blue cut of figure 6.12. The internal gate potential is plotted in dependence of the gate voltage, when the transistor is off and on as shown in figure 6.28. With increasing gate voltage the internal gate potential approaches the clear voltage of $V_C = +15$ V. By consulting equation 6.44 the electric field coefficient depends on the clear voltage and the internal gate potential. This reduces the electric field coefficient a and thus, the electric field in direction of the clear contact $E(z)$. Even at $V_{G,p} = +18$ V the internal gate potential is equal to the clear voltage, which results in $a = 0$. For simulation the structure was used, which is shown in the upper plot of figure 6.29 a). The electrons diffuse/drift more slowly and recombine in the low field regime in the middle of the internal gate. As the coefficient a is not high enough, the use of multiple pulses does not influence the clear performance.
At low gate voltages, $V_{G,p} < 12$ V, ν_E decreases with increasing number of gate pulses. In this case, the internal gate potential is negative relative to the clear voltage. The electric field coefficient is high enough to remove a bigger part of the electrons. Consequently, more gate pulses enhance the clear performance. At $V_{G,p} = 6$ V the electric field at the position of the collected charge is not high enough to emit all electrons during one gate pulse. The emission time ranges from 2 ns to 1 s as indicated in figure 6.11. That means that only a small fraction of electrons has an emission time, which is lower than the duration of one gate pulse (42 ns). The other fraction stays frozen in the shallow donors. That is why, at best, 40 % remain in the internal gate, when 20 pulses are applied.
The figures 6.29 b), c) and d) show the theoretical ν_T and experimental ν_E in dependence of the clear pulses for $V_{G,p} = 6$ V, 12 V and 18 V respectively. In this case the gate is pulsed once. Comparing the blue and black curves, the experimental results show a good agreement with the theoretical predictions. The deviation can be explained by the lack of three dimensional effects of the theoretical model. The presented simulation algorithm takes into account one time dimension and one to two spatial dimensions. When 3D effects are incorporated, the absolute value of the electric field is a little bit higher[8].

For the calculation of ν_T barrier effects, which are caused from the clear gate contact, were implemented in the simulation program. In our experiments a clear gate voltage of $V_{CG} = 0$ V was applied, which is more negative than the clear and the pulsed gate voltages. In figure 6.29 a) a cut of the potential of the internal gate at a depth of 0.6 μm is shown. The potential was simulated with TESCA at $V_C = 25$ V, $V_{CG} = 0$ V and at the gate voltage in the collection state, $V_{G,c} = -2$ V, and the pulsed states, $V_{G,p} = 6$ V, 12 V and 18 V. In the pulsed states a barrier exists, which is located below the clear gate contact. The clear gate barrier between the clear and internal gate is higher the higher

[8] The absolute value of the electrical field in three dimensions is: $|\overrightarrow{E_{3d}}|^2 = E_x^2 + E_y^2 + E_z^2$. Instead, the two dimensional electrical field is given by: $|\overrightarrow{E_{2d}}|^2 = E_x^2 + E_y^2 < |\overrightarrow{E_{3d}}|^2$

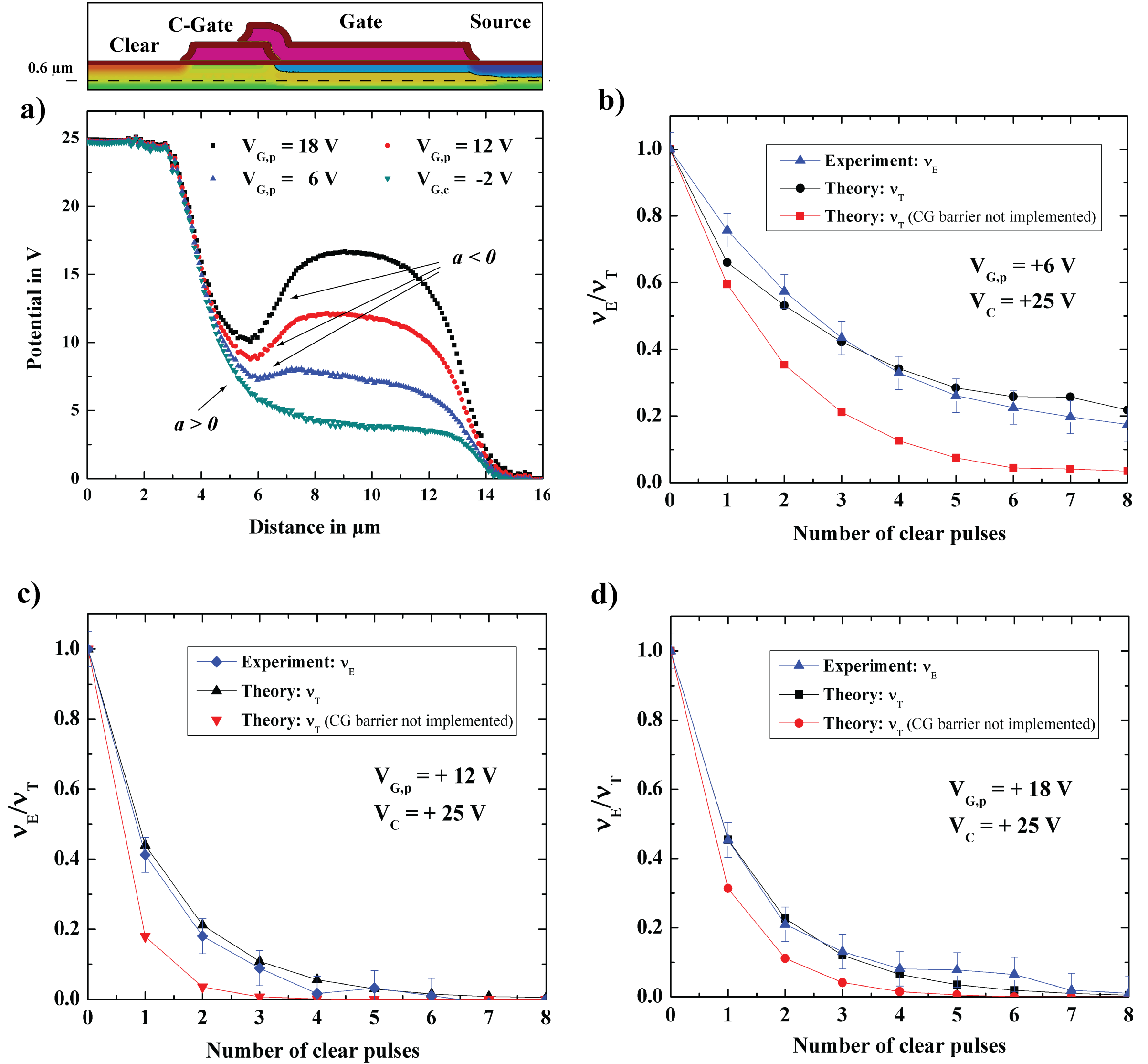

Figure 6.29: a) Cut of the potential of the internal gate at a depth of 0.6 μm for different gate voltages. The dashed line shows the potential at $V_G = 18$ V, when the clear gate does not influence the potential from internal gate to the clear contact. b), c) and d) ν in dependence of the number of clear pulses at $V_G = 6$ V, $V_G = 12$ V and $V_G = 18$ V respectively and $V_C = 25$ V. One gate pulse is applied. The red curves demonstrate the simulated data points, when the clear gate is not taken into account in the model. When the clear gate voltage is set to 0 V as was applied in the experiments (blue curves), a barrier is built up between the internal gate and the clear contact. The black curves show the simulated data points, when $V_{CG} = 0$ V.

the gate voltage in the pulsed state is. Therefore, the electrons in the internal gate are exposed to an electric field, which forces them to stay in the internal gate. In this case the electric field coefficient a is zero or negative. The electrons are emitted at the potential minimum 1 and drift to potential minimum 2 as indicated in figure 6.12, but the clear gate barrier avoids these electrons to reach the clear contacts.
In figure 6.30 the schematic of one gate pulse is shown. It illustrates that the effective reset arises from the pulsing from the pulsed to the collection state. Only, when the gate voltage is pulsed to the collection state, $V_{G,c} = -2$ V, the electric field coefficient a is positive. The electrons are emitted at the potential minimum 2 and drift to potential minimum 1. One part of the electrons recombines with the shallow donors and the other part diffuses/drifts to the clear contacts. When the clear gate barrier is not implemented in the model the theoretical ν_T (red curve in figures 6.29 b), c) and d)) is lowered relative to the experimental ν_E. In this case the barrier does not exist and the electrons can reach the clear contacts in the collection state as well as in the pulsed state. This leads to a reduced ν_T.

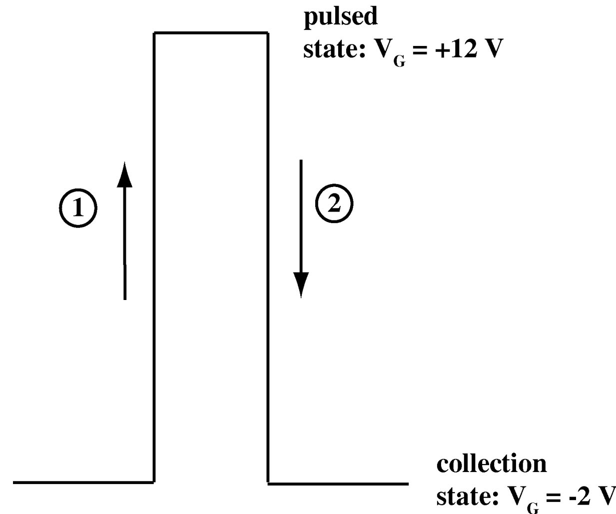

Figure 6.30: Schematic of one gate pulse. 1. The electrons are emitted into the conduction band, but they cannot reach the clear contact. The clear gate voltage of 0 V in the pulsed state leads to a barrier, which forces the emitted electrons to stay in the internal gate. 2. The emitted electrons drift/diffuse to the clear contact due to a positive electric field coefficient in the collection state.

6.4.3 Temperature dependence

The temperature dependence is another important issue, which has to be investigated. Instead of pulsing the gate, the source is pulsed to generate the electric fields at the position of the collected signal electrons. As typical operating temperatures of BIB detectors are 6 K to 10 K [51], this temperature regime is the field of interest in this subsection. Figure 6.31 shows the parameter ν_E at temperatures of 6 K and 11 K and at clear times of 2 μs and 16 μs. It can be seen that ν_E does not change with variable temperatures and clear times, when the source of the DEPFET is pulsed once. Only a ten fold pulsing reduces ν_E significantly. As there is no temperature dependence it is concluded that the emission is dominated by tunneling effects. The pure tunneling effect depends on the barrier height, which is given by $E_d - E_{PF}$, and the tunneling width. It is defined as the spatial distance between the ground state of the shallow donor and the conduction band at the same energy level. When the tunneling width is in the range of nanometers, the wave function of the trapped electron in the shallow donor overlaps with the conduction band. This results in tunneling. At the position of the collected charge a high electric field is generated, where the electrons are emitted into the conduction band. The electric field, which results from the simulation, is determined by the slope of the potential and is higher than 25 $\frac{\text{kV}}{\text{cm}}$ as can be seen in figure 6.33.

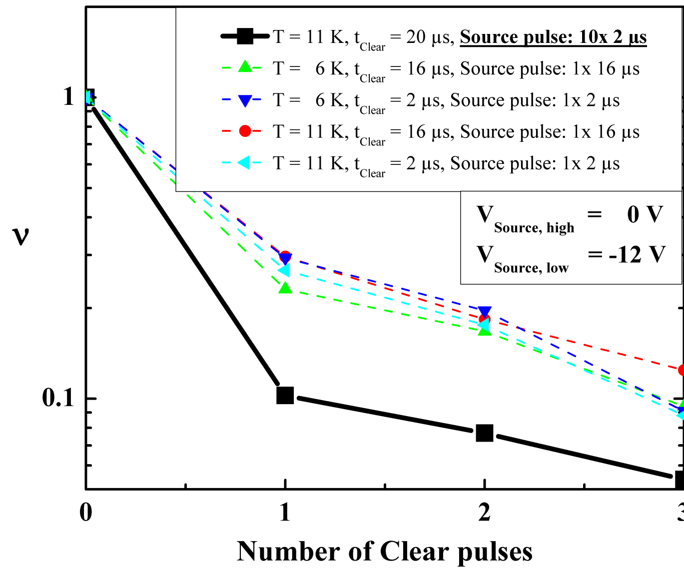

Figure 6.31: Measured fraction of remaining electrons ν_E for different temperatures (6 K and 11 K) and clear times (2 μs and 16 μs).

From the model of electric field enhanced emission an electric field higher than 17 $\frac{\text{kV}}{\text{cm}}$ is required to induce tunneling of trapped charge at temperatures lower than 20 K. In the case of weak fields, the emission time is strongly dependent on temperature. Therein, the tunneling width is high enough, so that tunneling does not occur. Thermal emission and thermal assisted tunneling dominate the emission time. However, in the case of electric fields lower than 10 $\frac{\text{kV}}{\text{cm}}$, the values of the emission time are in the range of seconds and higher (equation 6.13) and therefore not interesting for the studies.

6.5 Review of the experimental and theoretical methods

The predictions of the developed model and the experimental results were very good. The theoretical methods, which are described in this chapter, have consequences for the operation of the sensor system. The physical understanding of the reset method makes it possible to manipulate the electrons in the internal gate of the DEPFET. One example was already experimentally verified and is explained in section 6.4. By pulsing the gate contact several times the clear performance is enhanced. In this case, the electrons are permanently reemitted and remain longer in the conduction band. This makes it possible to remove all electrons by one clear pulse.
The simulations are required to understand and optimize the reset. The pulse form and the design of the DEPFET can be modified to further enhance the clear performance. In the next section, some examples are presented.
The model of the reset method is the fundament for the infrared sensor combination DEPFET - BIB detector. On the one hand, freeze-out of electrons is required in the active layer of the BIB structure as discussed in section 2.1. On the other hand, freeze-out decreases the clear performance of the DEPFET. The presented simulation program and the analysis of the model are required to understand the interdependency of these devices.

6.6 Future prospects

The operation of DEPFETs at low temperatures with a complete reset is a breakthrough in the field of cryogenic amplification [4]. Complete clear was achieved with room temperature devices within 420 ns. This is possible when high gate voltages of 12 V to 18 V are applied. This can be a problem, when the DEPFET - BIB device (figure 2.5) is operated. The difference of the internal gate potential and the back side voltage of the BIB structure represent the effective bias voltage. If the difference is too high, the BIB structure comes into the breakdown regime, where a high leakage current flows.
Therefore, two further types of DEPFETs were designed to investigate the parameter

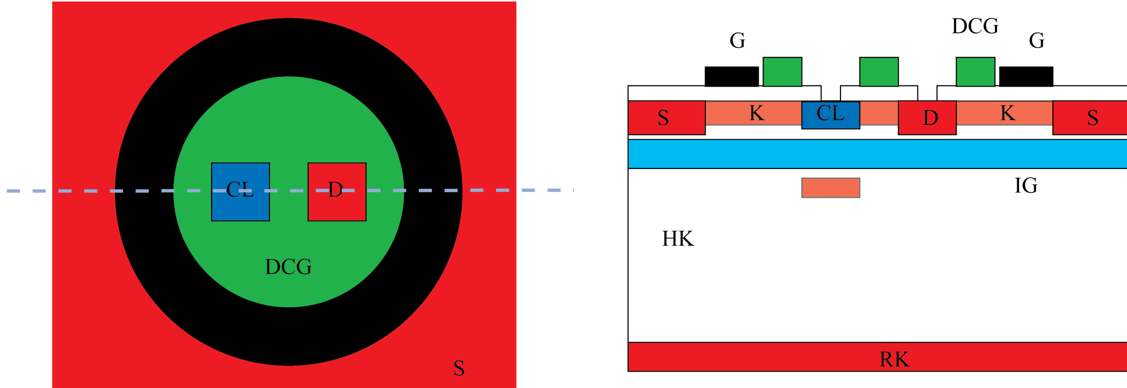

Figure 6.32: *Left:* Top view of the DCG-structure. *Right:* Cross section of a circular DCG-structure. S=source, D=drain, CL=clear, G=gate, K=iransistor channel, IG=internal gate, RK=back side, HK=bulk.

space and find out the most attractive structure for the DEPFET - BIB device. In addition, the shape of the pulse form is changed to enhance the clear performance.

6.6.1 Proposal for a new design

For the next DEPFET production, it is planned to produce new minimatrices for cryogenic applications. These structures are optimized for the reset at cryogenic temperatures. Two structures are described in the following subsections.

DCG-structure

The idea of the drain-clear-gate (DCG) structures goes back to the invention of G. Lutz [52]. It foresees a MOS region, which replaces the drain and the clear gate contact. Figure 6.32 shows the top view and the cross-section of a circular DCG-structure. The MOS contact comprises the clear and the drain contact and functions in the clear and collection state as follows:

1. In the collection status, the MOS contact is negatively biased in order to form a hole inversion layer underneath the oxide. The negative voltage of the drain is transferred to the high conductive inversion layer and the device is a transistor. A hole current flows from the source to the MOS-drain. The presence of the signal charge in the internal gate steers the transistor current.

2. During the clear process the MOS is set to a positive potential and functions as the clear gate. The electrons are removed to the positvely biased clear contact.

One advantage of this structure is, that no potential minimum does exist in the internal gate during the clear process. Thus, retrapping mechanisms do not occur. The only issue, which has to be considered for a complete clear is a sufficiently high electric field at the position of the collected charge. In this case only the emission time limits the clear time for the device.

Modified linear structures

Another concept is to modify the existing linear structures and steer the right and left clear contact of each pixel independently. As shown in figure 2.3 the pixel has two clear contacts on each side of the transistor. The idea is to seperate the steering of the clear contact on the left and the right side. For example, the left clear is pulsed to a high level and the right clear to a low level and vice versa. In this way, it is possible to shift the potential minimum in the internal gate transversal to transistor current and parallel to the surface (figure 6.12).

6.6.2 Source pulsing

It is shown that gate pulsing is an effective technique to clear the internal gate at cryogenic conditions. Another approach to generate electric fields is to pulse the source to negative voltages as already described in section 6.4.3. Figure 6.33 shows a one-dimensional plot of the potential of the internal gate in the pulsed and the collection state. Additionally, the electric field in the pulsed state is shown.

The shallow p-implanted source contact and n-doped Internal gate region can be seen as a backward biased pn-diode. In the collection state the potential minimum is located near the source contact as it is more positive ($V_S = 0$ V) than the drain ($V_D = -5$ V). When the source is pulsed to $V_S = -12$ V the potential minimum is shifted to the more positive drain. Simultaneously, electric fields of higher than 25 $\frac{\text{kV}}{\text{cm}}$ are created at the position of the collected signal charge. From equation 6.13 the emission time of 2 ns is low enough to emit the electrons within the clear time.

The advantage of source-pulsing is the lower absolute value of the potential of the internal gate in the pulsed state. Thus, for the combination DEPFET - BIB the potential difference between the internal gate and the back side is reduced. The internal gate potential is a linear function of the gate voltage as shown in figure 6.28. When gate pulsing is used the potential difference between the internal gate and the back side of the DEPFET - BIB is relatively high. This could lead to breakdown of the sensor.

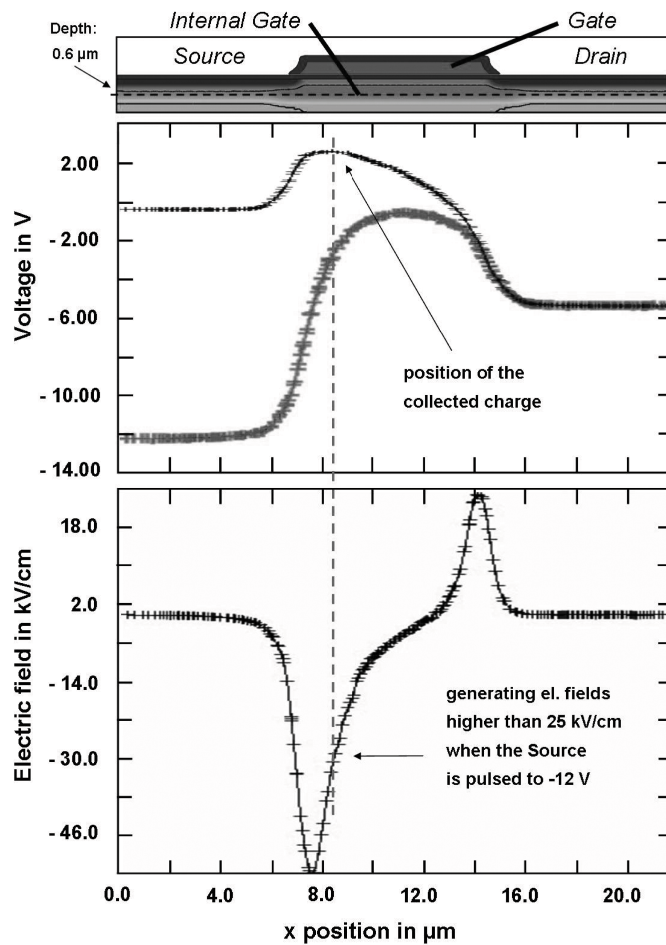

Figure 6.33: Plot of the transistor with its potential at a depth of 0.6 μm. Below, the electric field in x-direction is shown in the pulsed state. The potential and the electric field were simulated with TESCA.

6.6.3 Burst mode

A further improvement of the clear performance can be obtained by changing the shape of the gate pulse. Extremely short pulses are used, which have a triangular shape as shown in 6.34. Instead of the MUX Board, a pulser from Agilent H8114A, which can generate theses pulses with a pulse width of down to 10 ns, was used.
The effect of the burst mode is that the potential minimum is in a non-static state. As the pulsed state has no flat top, the potential minimum is always moving from position 1 to 2 (figure 6.12). The electrons do not undergo a static potential minimum, where the electric field is zero. In figure 6.35 ν_E is plotted against the amount of clear pulses in the standard and burst mode. The plot shows, that the clear performance can be enhanced significantly, when the burst mode is applied. A clear time of 420 ns at a temperature of 7.5 K was accomplished and for it, 6 burst pulses are used to remove the charge from the internal gate completely.

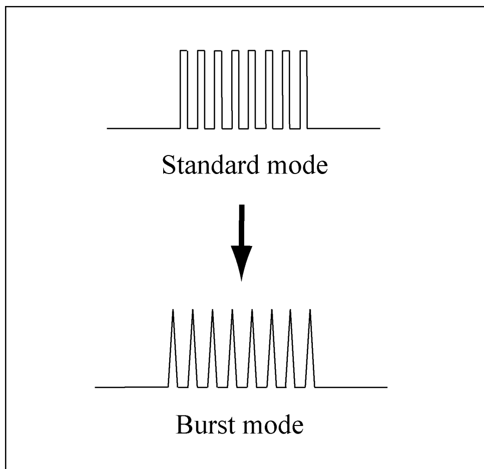

Figure 6.34: Shape of the gate pulse in the standard mode and the burst mode.

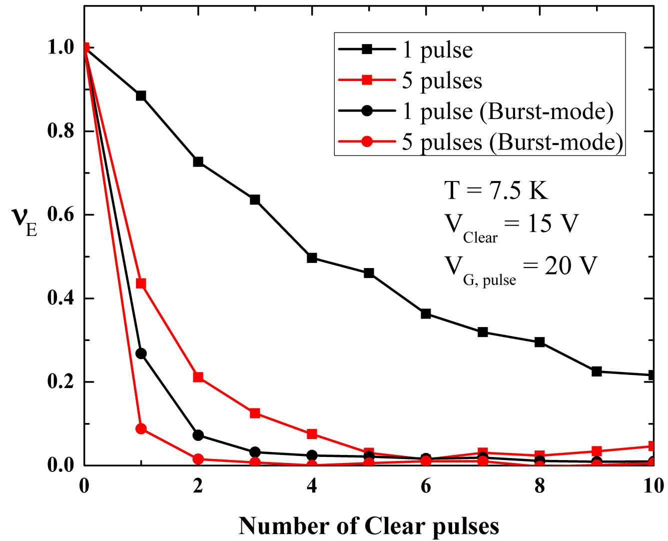

Figure 6.35: Measured fraction of remaining electrons ν_E in dependence of the number of clear pulses in the standard mode and the burst mode. The clear voltage is $V_C = 15$ V.

6.7 Summary of chapter 6

The reset of the DEPFET at cryogenic temperatures is the main topic of the thesis. The subject was worked out from the idea to a complete model of the physical mechanisms.
In section 6.1 the fundamental problem of the reset at cryogenic temperatures down to 6 K was explained. The low clear performance at cryogenic temperatures is caused by the freeze-out of the signal electrons into the ionized shallow donor states of the internal gate. By applying sufficiently high electric fields the trapped electrons are forced to be emitted into the conduction band, which leads to an enhanced clear performance. This is realized by pulsing the gate contact during the clear time.
Electric field enhanced emission from shallow donors, electric field dependent recombination into shallow donors and the drift and diffusion of the electrons in the internal gate describe the behaviour of the electrons during the clear process at cryogenic conditions. TESCA simulation were performed, where the potential and the electric field distribution of the internal gate during the clear process were calculated. The physical mechanisms and the TESCA simulations were discussed in section 6.2.
Section 6.3 describes how the previously mentioned physical mechanisms and simulations are implemented in a model. Combining the continuity equation for electrons with the equation for drift and diffusion one obtains a differential equation for the free electron concentration. The finite difference method was used to solve the differential equation dynamically. It was possible to determine theoretically the parameter ν_T, which is the fraction of recombined electrons after a certain clear pulse N_{rec} to the entire number of signal electrons N_{sig}. This parameter represents the clear performance of the DEPFET at cryogenic temperature.
Experimental results are discussed in section 6.4. Applying more gate pulses during the clear process and increasing the gate voltage in the pulsed state leads to enhanced clear performance. Furthermore, the parameter ν was compared with experiment for different gate voltages in the pulsed state. The experimental results agree very well with the theory. Deviations are explained by the limits of the model, which solves the differential equation in one spatial dimension.
The model has impact on the operation and the understanding of the DEPFET at cryogenic temperatures. Additionally, the simulations are needed to develop and understand the infrared sensor system DEPFET - BIB. In section 6.5, a short review of the model is presented.
Finally, in section 6.6, future prospects and ideas are presented, which further perform the clear performance of the DEPFET at cryogenic temperatures.

Chapter 7

Conclusion

The aim of the work is to get first insight into the device physics of the DEPFET and the BIB structure at cryogenic temperatures. Therefore, a measurement setup was established to investigate the static and dynamic behaviour. The thermal control of the setup was optimized for measurements in a temperature range from 5 K up to room temperature. The physical principle of the interaction of electrons with shallow donor states is the basis for the analysis of the device physics at cryogenic temperatures. The following results have been obtained:

- The activation energy of the shallow donors in the BIB structures was experimentally determined. The slope of the Arrhenius plot corresponds to an activation energy of 27 meV. This value is obtained at the optimum bias voltage of $V_B = 0.2$ V. The binding energy of the single donor state of antimony is 42.7 meV. The reduced activation energy is explained by the broadening of the impurity band. Furthermore, the hopping conduction in the impurity band is blocked effectively and the leackage current is suppressed to a minimum at low temperatures. Only by shielding the thermal background radiation in the experiment this property could be observed.

- The activation energy is further reduced by increasing the bias voltage. Intrinsic electric fields exist, which are responsible for the lower activation energy. They originate from the ionized donor state at the interface between the active and blocking layer. The out-diffusing of antimony from the active layer during the growth process of the blocking layer is responsible for the high concentration of ionized donors at the interface. Potential improvement can be obtained by MBE[1] facilities. The epitaxy process of the blocking layer must be optimized to suppress the dark current at high bias voltages of $V_B = 1$ V. Only at higher bias voltages the BIB structure can be successfully operated.

[1] Molecular Beam Epitaxy

- The low intrinsic amplification of the DEPFET at cryogenic temperatures is caused by trapped electrons. These electrons stay permanently in the internal gate and act repulsively on incoming signal electrons. Therefore, the signal electrons are collected, where the steering impact on the transistor is low. This explains the reduced amplification at 6 K by a factor of two compared to room temperature.
- The clear performance of the DEPFET suffers from the freeze-out of signal electrons. It was not possible to remove all signal electrons by one clear pulse leading to ineffective operation of the DEPFET. In this work a new reset method was developed and worked out from the initial idea to a complete physical model, which was experimentally verified with good precision.

This work shows for the first time that the DEPFET works at cryogenic temperatures down to 5 K. The new developed reset method makes it possible that the DEPFET can be operated under this condition. The idea of the reset method bases on the emission of the trapped electrons into the conduction band by applying electric fields. It is realized by pulsing the gate contact during the clear process. For an effective reset it is not sufficient to pulse the gate contact once as the electrons are located in a complex potential distribution in the internal gate. However, recombination processes occur, which cause that not all electrons can be removed from the internal gate. Therefore, a physical model for the reset method was developed, which describes the interdependency between emission, recombination and drift/diffusion of electrons. The model leads to a better understanding of the physics of the device at cryogenic temperatures.
The understanding of the physical processes is relevant to optimize the reset. By using multiple pulses, clear times as short as 420 ns at a temperature of 7.5 K can be achieved with this method. This value is comparable to clear times at room temperature, which are in the range of nano- to microseconds.
Furthermore, the possibility is given to develop any cryogenic semiconductor detector with the DEPFET as the integrated amplifier. The presented reset method can be applied on such a device. One example is the infrared sensor combination DEPFET - BIB detector, which is presented in this work.
Finally, I developed the experimental and theoretical methods for the DEPFET and the BIB structure, which are presented in this work, to examine their physical device properties. I come to the conclusion that it exists sufficient understanding to produce the device DEPFET - BIB detector. The next step is the investigation of this device and the development of a physical model for its properties, which is based on this thesis. It promises to be a very low-noise mid-infrared photodetector, which enables to observe faint astrophysical objects.

Bibliography

[1] M.D. Petroff and M.G. Stapelbroek. Blocked impurity band detectors. US Patent No. 4,568,960, 1986.

[2] J. Kemmer and G. Lutz. New detector concepts. *Nucl. Instr. and Meth. A*, 253:356, 1987.

[3] V. Fedl et al. A new concept for a cryogenic amplifier stage. *Nucl. Instr. and Meth. A*, 624:476 – 481, 2010.

[4] L. Strüder, G. Lutz and V. Fedl. Halbleiterstruktur, insbesondere bib-detektor mit einem depfet als ausleseelement, sowie entsprechendes betriebsverfahren. Patent: DE102009023807A1, 2010.

[5] A. Rogalski. *Infrared Detectors*. Gordon and Breach Science Publishers, 2007.

[6] Caroline A. Kilbourne et al. Uniform high spectral resolution demonstrated in arrays of tes x-ray microcalorimeters. *Proc. SPIE*, 6686:1 – 10, 2007.

[7] D. A. Wollman et al. High-energy resolution microcalorimeter spectrometer for x-ray microanalysis. *J. Microsc.*, 188:196 – 223, 1997.

[8] W.D. Lawson et al. Preparation and properties of hgte and mixed crystals of hgte-cdte. *J. Phys. Chem.*, 9:325 – 329, 1959.

[9] James W. Beletic et al. Teledyne imaging sensors: Infrared imaging technologies for astronomy & civil space. *Proceedings of the SPIE Conference on Astronomical Instrumentation*, pages 1 –14, 2008.

[10] A. G. U. Perera et al. Gaas/algaas quantum well photodetectors with a cutoff wavelength at 28 μm. *Appl. Phys. Let.*, 72:1596, 1998.

[11] Mermin Ashcroft. *Solid state physics*. Harcourt College Publishers, 1976.

[12] G. H. Rieke. Infrared detector arrays for astronomy. *Annu. Rev. Astron. Astrophys.*, 45:77 – 115, 2007.

[13] N. F. Mott and W. D. Twose. The theory of impurity conduction. *Advances in Physics*, 10:107 – 163, 1961.

[14] F. Stern and R. M. Talley. Impurity band in semiconductors with small effective mass. *Phys. Rev.*, 100:1638 – 1643, 1955.

[15] F. Szmulowicz and F. L. Madarsz. Blocked impurity band detectors - an analytical model: Figures of merit. *J. Appl. Phys.*, 62:2533 – 2540, 1987.

[16] R. Hartmann, K.-H. Stephan, L. Strüder. The quantum efficiency of pn-detectors from the near infrared to the soft x-ray region. *Nucl. Instr. and Meth. A*, 439:216 – 220, 2000.

[17] S. Wölfel. *Neuartige DEPFET-RNDR-Detektoren im experimentellen Betrieb.* PhD thesis, Universität Siegen, 2007.

[18] E. Gatti and P. Rehak. Semiconductor drift chamber - an application of a novel charge transport scheme. *Nucl. Instr. and Meth. A*, 225:608 – 614, 1984.

[19] Michael E. Ressler et al. Performance of the jwst/miri si:as detectors. *Proc. SPIE*, 7021:1 – 12, 2008.

[20] P. J. Love et al. 1024 x 1024 si:as ibc detector arrays for mid-ir astronomy. *Proc. SPIE*, 6276:1 – 8, 2006.

[21] J. Frenkel. On pre-breakdown phenomena in insulators and electronic semiconductors. *Phys. Rev.*, 54:647, 1938.

[22] M. Cardona P.Y. Yu. *Fundamentals of Semiconductors.* Springer Verlag, 1996.

[23] B. C. Dodrill et al. Performance characteristics of silicon diode cryogenic temperature sensors. *Applications of Cryogenic Technology*, 10:85 – 106, 1991.

[24] Yu. M. Shwarts et al. Silicon diode temperature sensor without a kink of the response curve in cryogenic temperature region. *Sensors and Actuators*, 76:107 – 111, 1999.

[25] S. M. Sze. *Physics of Semiconductor Devices.* John Wiley & Sons Inc., 1981.

[26] H. Santos and J. L. Gray. Field-dependent electron mobility in silicon between 8 and 77 k - a semi-empirical model. *IEEE Trans. on Electron Devices*, 35:1972 – 1976, 1988.

[27] Robert M. Glidden et al. Optimization of cryogenic cmos processes for sub-10k applications. *Proc. SPIE*, 1684:2 – 39, 1992.

[28] F. J. Morin and J. P. Maita. Electrical properties of silicon containing arsenic and boron. *Phys. Rev.*, 96:28 – 35, 1954.

[29] S.K. Tewksbury. Transient response of n-channel metal-oxide-semiconductor field effect transistors during turnon at 10 - 25 k. *J. Appl. Phys.*, 53:3865 – 3872, 1982.

[30] V. Fedl, L. Barl, G. Lutz and L. Strüder. Investigation of single pixel depmosfets under cryogenic conditions. *Conference record of IEEE Nuclear Science Symposium and Medical Imaging*, 1:1378 – 1381, 2008.

[31] C. Sandow et al. Clear-performance of linear depfet devices. *Nucl. Instr. and Meth. A*, 568:176 – 180, 2006.

[32] P. Klein. *Entwicklung, Bau und Test eines Halbleiter-Bildzellendetektors für den Einsatz in der Teilchenphysik.* PhD thesis, Ludwig-Maximilians-Universität, 1996.

[33] M. Porro et al. Spectroscopic performances of depmos detector/amplifier device with respect to different filtering techniques and operating conditions. *IEEE Trans. on Electron Devices*, pages 1 –, 2004.

[34] E. M. Conwell. Impurity band conduction in germanium and silicon. *Phys. Rev.*, 103:51 – 61, 1956.

[35] W. Baltensperger. On conduction in impurity bands. *Phil. Mag.*, 44:1355, 1953.

[36] K.-F. Berggren and B. E. Sernelius. Band-gap narrowing in heavily doped many-valley semiconductors. *Phys. Rev. B*, 24, 1981.

[37] James E. Huffman et al. Si:sb blocked impurity band detectors for infrared astronomy. *J. Appl. Phys.*, 72:273 – 275, 1992.

[38] R. K. Ray and H. Y. Fan. Impurity conduction in silicon. *Phys. Rev.*, 121:768 – 779, 1961.

[39] J. Repp. Modeling and experimental investigations of the spectral response of extrinsic photon detectors. Master's thesis, Ludwig-Maximilians-Universität, 2010.

[40] G. Lutz. *Semiconductor Radiation Detectors.* Springer Verlag, 1999.

[41] G. Abstreiter. Skript halbleiterphysik. private communications.

[42] H. Gajewski et al. *TESCA - Two Dimensional Semiconductor Analysis Package*. WIAS, Berlin, 1997.

[43] E. Rosencher, V. Mosser and G. Vincent. Transient-current study of field-assisted emission from shallow levels in silicon. *Phys. Rev. B*, 29:1135 – 1147, 1984.

[44] M. Lax. Cascade capture of electrons in solids. *Phys. Rev.*, 119:1502, 1960.

[45] E. Simoen B. Dierickx and G. Declerck. Transient response of silicon devices at 4.2 k: 1. theory. *Semicond. Sci. Technol.*, 6:896 – 904, 1991.

[46] C. Jacoboni, F. Nava, C. Canali and G. Ottaviani. Electron drift velocity and diffusivity in germanium. *Phys. Rev. B*, 24:1014 – 1026, 1981.

[47] P. Norton, T. Braggins and H. Levinstein. Recombination of electrons at ionized donors in silicon at low temperatures. *Phys. Rev. Let.*, 30:488 – 489, 1973.

[48] N. Kimmel. *Analysis of the charge collection process in solid state x-ray detectors*. PhD thesis, Universität Siegen, 2008.

[49] A. Einstein. Über die von der molekularkinetischen theorie der wärme geforderte bewegung von in ruhenden flüssigkeiten suspendierten teilchen. *Annalen der Physik*, 17:549 – 560, 1905.

[50] W. H. Press et al. *Numerical Recipes*. Cambridge University Press, 2007.

[51] Raytheon. Astronomical infrared sensor chip assemblies. Technical report, Raytheon Vision Systems, 2004.

[52] G. Lutz, L. Strüder and R. Richter. Semiconductor structure, particularly in a semiconductor detector, and associated operating method. Patent: US2008001180, 2008.

Declaration

of the graduand, Valentin Philipp Fedl.

With the handing over of the PhD thesis, I assure, that I composed the thesis autonomously and did not use any other sources or additives.

....	....
Location, date	*Signature*

Acknowledgement

I owe the success of the project and the PhD thesis to the experience and the support of the employees in the semiconductor laboratory and in the MPE. Therefore, I want to thank the people, who supported me in this project:

- Especially, I thank Prof. Lothar Strüder for the PhD project in the semiconductor laboratory. The investigation of the DEPFET and BIB detectors at cryogenic temperatures was a very new project and I could enforce my competences in many fields of semiconductor physics, such as technology, design, device measurements, theory and simulations. Additionally, the helpful discussions lead to a very good progress of the work and I learned to supervise a novel project. Furthermore, I experienced to keep on solving hard problems and never give up the believe that it can and will work.

- A lot of thanks goes to Dr. Gerhard Lutz for the simulations with the DEPFET. From the very creative and useful discussions I got a new point of view and I could develop new approaches to solve the problems.

- Many thanks goes to Prof. Ullrich Pietsch for the work as the second supervisor and the invitations to the presentations in his institute.

- I thank Lothar Barl from the infrared group of the MPE for the experience and support in cryogenic measurement setups.

- My Diploma student Jens Repp worked on the Fourier Transform Spectroscopy. I thank him for getting further insights to our BIB detector devices.

- Great thanks goes to Dr. Rainer Richter, who supported me with his experiences in linearly structured DEPFETs, simulations and technology.

- I thank Dr. Peter Lechner, who supported me with the design program Cadence. This program enabled me to make the first design of the BIB detectors and cryogenic DEPFETs.

- Many thanks go to Dr. Johannes Treis, who introduced me to the SPIX-Board and gave me insight to the complexity of the frontend electronics.

- I want to thank Dr. Laci Andricek, Gerhard Liemann and Bianca Schweinfest, who prepared the first wafers of the BIB detector chips.

- A lot of thanks goes to Norbert Meidinger for the very helpful discussion about thermal emission of electrons in impurity states in semiconductors and for the support with the instruments of his group.
- Dr. Heike Soltau and Dr. Florian Schopper gave me useful technological advice and therefore, a lot of thanks goes to them.
- Thanks goes to Rouven Eckhardt, who handled the samples for the SIMS measurements.
- Danilo Mießner bonded the chips on the ceramics quickly. A special thank goes to him.
- Also, I thank the whole PhD students group, especially Stefanie Ebermayer, Asya Mikova, Dieter Schlosser, Stefan Rummel and Ivan Ordavo. A special and great thanks goes to Gregor Rossmanith and Jasper Werhahn, with whom I can discuss general mathematical and physical topics.
- As well, thanks goes to the persons, who are not named but contributed to the success of the work.
- Finally, many thanks goes to my parents, Jürgen and Linda, and my sister, Dian, who support me in everything I do.